

Fabrication and Measurement of Nanomechanical Resonators

Richard Cousins, BSc(Hons), MRes

Thesis submitted to the University of Nottingham

for the degree of Doctor of Philosophy.

June 2016

Abstract

Over the past years there has been great progression in the field of micro- and nanomechanics with devices with higher and higher Q factors being created. This has been made possible thanks to a combination of advances in fabrication techniques and an increase in understanding as to what causes dissipation in nanometre scale structures. This understanding of dissipation mechanisms is still incomplete however. While lots of work has been done investigating mechanisms such as thermoelastic dissipation and dissipation due to two level systems (TLS) within the standard tunnelling model (STM) a full understanding has not been forthcoming. The increase in the quality of nanomechanical systems has allowed them to be coupled to optical or microwave cavities allowing the position of the mechanical system to be measured with near quantum limited accuracy. This thesis looks at both these streams of research within nanomechanics. It looks at the fabrication of silicon nitride torsional resonators that can have either their flexural or torsional modes preferentially actuated via a piezoelectric drive. It was found for a single paddle resonator that the room temperature Q

factor of the flexural mode was 2870 ± 70 and for the torsional mode was 5050 ± 220 . It was shown that while thermoelastic damping was reduced in the torsional mode it was still present meaning that we could not use the model for a simple beam to describe thermoelastic damping for a paddle resonator. The properties of an nanomechanical beam fabricated from a single crystal of aluminium were also investigated. It was found that at 1.5 K it had an unloaded Q factor of 36900 which is at least 2 times larger then any other group has reported. We also used our knowledge of high stress silicon nitride membranes to design a system that could couple an aluminium on silicon nitride membrane to a LCR circuit. Calculations show that this would have a coupling constant, g , of over 1000 putting it well within the regime where ground state cooling and quantum limited measurements are possible.

Acknowledgements

As is always the case with a completing a PhD there is a huge list of people that need thanking. Thanks to my supervisor Chris Mellor for giving me a chance to do this and helping me along the way. I also need to thank John Owers-Bradley for giving me the use of his fridge and providing endless help and advice for using it. I am indebted to the staff in the workshop for helping me numerous times even if I only had a badly drawn request on a scrap of paper, an special thanks to Pete Smith for always helping me quickly. In the cleanroom I need to thank Jas Chauhan for keeping everything running and Dave Taylor for dropping everything to help whenever I need it. Thanks to Elisa Antolin for growing me the single crystal aluminium used in this work (and also lindy hopping with me). Thanks to Chris Pallender and Dave Holt for supplying me with liquid helium even at short notice and always being helpful. There have been many colleagues over the time who have helped me and I would like to say a special thanks to Mark Patton for helping in the early days and to James Thorpe for always being ready to help with a helium transfer or a hair brained plot to

send a webcam into the dewar, James also earns a thanks for putting up with my descent into madness while writing this thesis.

Over my time here I have been lucky enough to make a number of amazing friends in particular (in no particular order) James, Duncan, Vicky, Ryan (and Sam), Sarah, Caroline, Robin, Lucy, Stuart, the cricket team and not forgetting that special someone (you know who you are!). A big thanks to Sacha, Che and Isabella de le Fuente for giving me things to do on the weekend, the staff at the JA for helping me to recover after a week of work and Anna in the tearoom for keeping me fed and watered. I'm sure I will have forgotten someone so feel free to add your name here _____.

Finally None of this would have been possible without the love and never-ending support of my family, I have no idea what I would have done without them standing behind me.

Thank you,

Richard

To my Grandfather whom I miss everyday.

Contents

1	Introduction	1
1.1	Quantum Limited measurements of a mechanical mode	2
1.2	Dissipation	7
1.3	Coupled Circuits	8
1.4	Outline	9
2	Linear Dynamics of Nanomechanical resonators	12
2.1	Flexural Modes of Beams	13
2.2	Torsional Modes of Paddle Resonators	20
2.3	Flexural Modes of Square and Circular Membranes	23
2.3.1	Conclusion	28
3	Damping Within Nanomechanical Resonators	29
3.1	Extrinsic Dissipation	30

CONTENTS

3.2	Intrinsic Dissipation	35
3.3	Other Works on Dissipation in Micro- and Nanomechanical resonators	44
3.4	Conclusion	51
4	Microwave Coupling and Quantum Limited Measurements	52
4.1	Quantum Limited Measurements	53
4.2	Microwave Coupling	54
4.3	Other Work on Microwave Coupling	59
4.4	Conclusion	64
5	Fabrication of Nanomechanical Devices	65
5.1	Wafers	66
5.2	Metallization	67
5.3	Etching	69
5.4	Lithography	70
5.4.1	Proximity Effect Correction	75
5.5	Fabrication of Gold Bow Tie Nano Antennas	77
5.6	Fabrication of Silicon Nitride Torsional Resonators	81
5.7	Fabrication of Single Crystal Aluminium Beams	86

CONTENTS

5.8	Air Bridges	88
5.9	Fabrication of on-chip LCR circuit	91
5.10	Conclusion	97
6	Silicon Nitride Torsional Resonators	98
6.1	Measurement Techniques	99
6.2	Results	110
6.2.1	Analysis	120
6.3	Conclusion	130
7	Single Crystal Aluminium NEMS	133
7.1	Experimental Method	134
7.1.1	Magnetomotive detection	134
7.1.2	Experimental Set Up	137
7.2	Results	141
7.3	Analysis	148
7.4	Conclusion	156
8	Design of an on chip LCR circuit	159
8.1	LCR circuit Design	159
8.2	Conclusion	170

CONTENTS

9 Summary and Future Work	171
9.1 Future Work	173
9.2 Conclusion	176
A Fabrication Details	178
A.1 Silicon Nitride Torsional Resonators	178
A.2 Single Crystal Aluminium Resonators	181
A.3 Aluminium and silicon nitride on chip LCR circuits . . .	183
References	188

List of Symbols

Symbol	Quantity	Units
κ	Spring constant	Nm^{-1}
γ	Damping	Hz
ω_0	Natural Frequency	Hz
f_0	Resonant frequency	Hz
E	Young's Modulus	Pa
I	Inertia	Kgm^2
T_0	Tension	N
ρ	Density	Kgm^3
m,n	Mode number	-
ν_p	Poisson's raito	-
η	Magnetic damping Constant	T^{-2}
α	Coefficient of thermal expansion	K^{-1}
κ_0	Zero point motion	m
C_p	Volumetric Specific Heat Capacity	$\text{Jm}^{-3}\text{K}^{-1}$
l_T	thermal diffusion length	m
I_r	Irradence	Wm^{-2}
\bar{n}	Thermal occupation	-
p_n	Occupation Probability	-
C	Cooperativity	HzM^{-1}
g	Coupling Strength	Hz

CHAPTER 1

Introduction

Over the past decade there has been an explosion in the use of micromechanical resonators (MEMS) in consumer electronics, they feature in smart phones, the Nintendo Wii WiimoteTM and ensure the stability of the increasingly popular drones. As with many aspects of physics there has been a drive to miniaturize these devices. This has led to nanoelectromechanical systems. This has been made possible thanks to rapid progress in nanofabrication techniques. Some work has looked at developing these devices to be highly sensitive sensors for properties such as mass [1], force [2], and spin [3]. Another interesting stream of research is to use these devices to explore the sometimes blurred boundary between classical and quantum descriptions of the world.

The aim of this work is to create a device that is capable of measuring its movement with quantum limited precision, that is being able to measure a mode of a resonator when it is in its quantum ground

state. To reach this aim we need to understand a number of different things. We need to firstly understand what we mean by the phrase quantum limited measurement and understand how we will know that we are measuring a mode of a resonator with quantum limited accuracy. Secondly as to perform quantum limited measurements we need high quality resonators we need to understand what makes a high quality resonator therefore we need to investigate what causes dissipation in nanomechanical resonators. Finally we need to consider how to combine our knowledge of quantum limited measurements with high quality factor resonators.

1.1 Quantum Limited measurements of a mechanical mode

One of the long standing aims of nanomechanics has been to be able to bridge the length scales of quantum mechanics with those of classical mechanics. In particular it is interesting to see what size of object it is possible to describe with quantum mechanics. It was hoped that thanks to their small size and high quality factors it would simply be a case of creating a resonator and then cooling it down until the equation,

$$\frac{\hbar\omega}{k_{\text{B}}T} \gg 1, \quad (1.1.1)$$

is satisfied, where, ω is the resonant frequency of the NEMS and T is

its temperature. When this condition is satisfied it can be said that the resonator is in the quantum regime. When the resonator is in the quantum regime its movement can be described by quantum mechanics and therefore the movement can be described by wavefunctions. The aspect of quantum mechanics we are looking at is putting a resonator in its quantum groundstate. When the resonator is in its quantum groundstate it is moving with just a single quanta of energy. The inclusion of the resonant frequency factor shows that rather than putting the whole resonator in its quantum ground state we are only putting one particular mode of the resonator in its quantum groundstate with higher order modes still being at higher energies. When this mode is in its quantum ground state it is possible given a suitable measurement system to measure it with quantum limited precision. O'Connell et al. managed to create such a device by driving the fundamental mode of a dilational resonator which had a resonance of 6 GHz [4]. They were able to measure the response of the resonator by coupling it to a quantum qubit that showed at 25 mK it had a resonant frequency of 6 GHz and therefore ensured that the Equation 1.1.1 was satisfied. However due to the large frequencies and short mechanical lifetimes they were unable to measure its motion with quantum limited accuracy or to couple the resonance with an electrical circuit and therefore manipulate it.

This shows that the main problem of working with high mechanical frequencies is that it produces resonators with very small zero point

motion, κ_0 ,

$$\kappa_0 = \sqrt{\frac{\hbar}{2M_{eff}f_0}} \quad (1.1.2)$$

where M_{eff} is the resonator's effective mass and f_0 is its resonant frequency. For example, the resonator used in [4] would have a zero point motion less than 1 fm. In addition to this, devices with mechanical frequencies in the GHz range are very stiff making them particularly fragile and difficult to fabricate.

This means that we are in the situation where, rather than use resonators with higher and higher frequencies we need to find a better way of cooling the resonator down. If we want to work with resonances in the low MHz range then looking at Equation 1.1.1 we need to be in the sub mK temperature range, something that is impossible using commercial cooling techniques such as dilution refrigeration. Whilst it is possible to use cooling techniques such as nuclear demagnetization to cool the resonator to a few mK this option was not available to us. It could also be possible to use optical cooling to cool the resonator as Chan et al. did [5], however this is not applicable to the range of materials we would like to cool or the vibrational modes we are interested in.

As it is not possible to use conventional refrigeration to cool the environment our resonator is in, a number of groups are looking at ways to reduce the effective temperature of the resonator. One way of doing this is by coupling the resonator to an microwave circuit. In doing this

it is possible to transfer energy between the electrical circuit and the mechanical resonator. By creating an energy flow from the resonator to the electrical circuit it is possible to effectively cool a vibrational mode of the resonator. This cooling system is known as (microwave) sideband cooling and will be discussed in greater detail in later chapters, but for it to be as effective as possible it requires that the mechanical resonance has as narrow a linewidth as possible i.e. the resonance has a Q factor as high as possible.

The Q factor of a resonator, $Q = f_0/\Delta f$ with f_0 being the resonant frequency and Δf is the full width at half maximum, FWHM, of the resonant peak, is a measure of how little energy it loses over a given time, with higher Q factors allowing for faster and stronger interactions between the mechanical and electrical elements. This results in better cooling of the mechanical element. This means that it is important to create devices with high Q factors. Figure 1.1 is a well known plot that suggests that Q factors tend to scale inversely with size and therefore zero point motion (which needs to be as large as possible to facilitate accurate measurement of its quantum ground state). However more recent work has shown that increasing the inbuilt stress of a resonator increases its resonant frequency without negatively effecting its damping. This in turn increases the Q factor of the resonator.

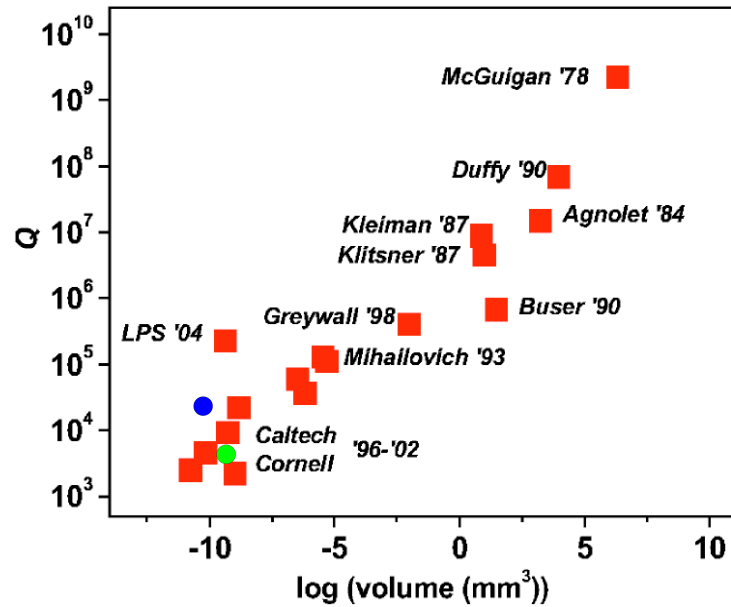


Figure 1.1: Figure showing how Q factor is inversely proportional to resonator size. Reproduced from [6]. Added to the original image is two of our results. The aluminium resonator discussed in Chapter 6 (blue circle) had a resonant frequency of 12.5 MHz and was measured at 1 K , and the silicon nitride torsional resonator in Chapter 5 (green circle) had a resonant frequency of 9 MHz and was measured at 300 K. It is likely by cooling the resonators these points will rise up and therefore beat the linear trend shown.

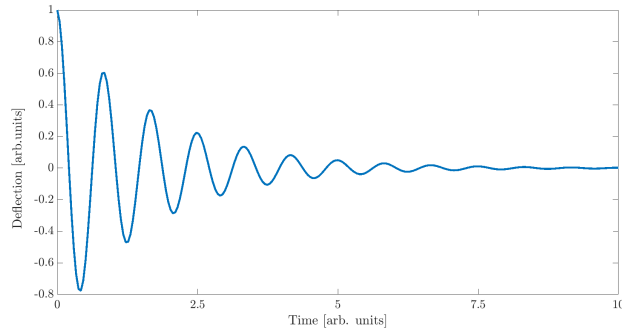


Figure 1.2: Figure showing how an undriven oscillators motion will decay over time. A higher Q factor will result in longer decay times.

1.2 Dissipation

Whether a NEMS is being used for a more classical physics purpose such as mass sensing, or being used to probe quantum mechanics it is a requirement for it to have as small a dissipation as possible. Dissipation is a measure of how quickly a undriven resonator will lose energy with a small dissipation meaning that a NEMS resonator does not lose energy as quickly as a resonator with a large dissipation (Figure 1.2) with the Q of the resonator being directly proportional to the ring-down time. Having a small FWHM is useful as it means that it is possible to detect very small shifts in frequency. These shifts in frequency allow NEMS to be used in many sensing applications. With the ongoing drive for miniaturization and because the Q factor is inverse to size a common value used to describe the quality of a resonator is the product of the resonant frequency and Q factor, fQ .

Whilst it has been known for a long time that it is important for a

resonator to have as little dissipation as possible we are still a long way from fully understanding what causes dissipation at low temperatures. While over the past years and decades the physics community has learned to make resonators with higher and higher values of fQ it is often without a concrete idea as to what is causing this dissipation. It is known that at higher temperature dissipation is caused by localized strain within the resonator causing heating and therefore an energy loss however little is known about what happens when the movement is torsional rather than flexural. At the lowest temperatures it is known that the dissipation arises from defects in the solid creating an energy flow, again however, the precise mechanism is not perfectly understood.

1.3 Coupled Circuits

To produce accurate measurements of the microwave circuit it is advantageous to have the electrical circuit as close as possible to the mechanical element. This results in a lot less noise from the environment as it is possible to isolate the signal we are interested in. A common way of getting the electrical system close to the mechanical element is to integrate the electrical circuit onto the same chip that the resonator is located. Modern fabrication techniques allows for the fabrication of a range of common electrical elements, such as inductors and capacitors onto the surface of a chip. An early example of this on-chip circuitry is

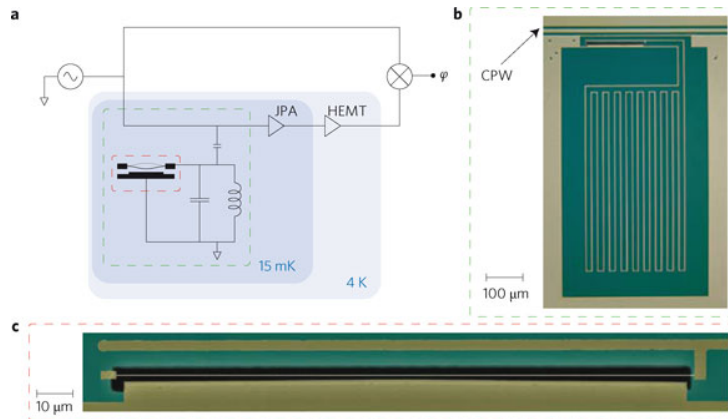


Figure 1.3: An example of an on chip LCR circuit that includes a nanofabricated variable capacitor and meander inductor. a) shows the electrical circuit while b) and c) show optical and scanning electric microscope images respectively of the circuit. Reproduced from [7].

the LCR circuit created by Teufel et al. [7] shown in Figure 1.3. They created a meander inductor and a capacitor that included a mechanical element. By integrating a mechanical resonator into one of the electrical elements it is possible to couple the mechanical resonator with the microwave circuit and therefore perform sideband cooling.

1.4 Outline

The aim of this thesis is to demonstrate that we will ultimately be able to make a device that can couple a high Q mechanical element into a microwave circuit and therefore perform sideband cooling. As well as possibly measure the movement of the resonator with quantum limited precision. As we first need a good understanding of the mechanics of the mechanical element Chapter 2 looks at deriving the

equations of motion behind a range of different nanomechanical resonators while they are in the linear regime. As mentioned earlier one of the most important aspects of nanomechanics is understanding dissipation especially at low temperatures. Chapter 3 looks at a number of different dissipation mechanisms with a particular focus on dissipation due to two level systems which is seen as highly important at the lowest temperatures. Chapter 3 also discuss work by other groups that have investigated dissipation in a range of different materials. Chapter 4 discuss the theory behind making quantum limited measurements of a mechanical resonator and introduces a number of key values. Chapter 4 also looks at a number of pieces of work by other groups. Once the theory behind the mechanics of nanomechanics has been investigated we move on to discussing how to create these devices. Chapter 5 looks at the equipment and methods I have used to create a wide range of devices with features in the nm range. Further fabrication details can also be found in the Appendix. Next the thesis moves onto experiments I have performed here in Nottingham. Chapter 6 studies experiments on silicon nitride torsional resonators. They were measured optically and Chapter 6 includes details of the measurement system before discussing what causes the dissipation in torsional resonators at room temperature. Next we moved onto consider resonators fabricated from a single crystal of aluminium. Chapter 7 looks at these resonators and starts by describing the measurement system used to investigate them. It

then goes on to discuss why they have considerably higher Q factors than similar beams made from polycrystalline aluminium. Chapter 8 explains the design of a resonator that could operate in the quantum regime. In particular it looks at a circuit that incorporates a mechanical resonator into a capacitor that was then coupled to an inductor thus making an LC circuit. Finally Chapter 9 summarises the work and looks at future directions for this research.

CHAPTER 2

Linear Dynamics of Nanomechanical resonators

The aim of this thesis is to create devices with high Q factors that can be used to perform experiments on microwave coupling and progress towards being able to make quantum limited measurements. To be able to do this we need to fully understand the mechanics of a nanomechanical resonator. This chapter looks at the dynamical properties of a range of nanomechanical resonators in the linear regime. We will define equations of motion for the flexural modes of beams, torsional modes of paddle resonators and flexural modes of both rectangular and circular membranes. This will also allow us to find estimates for the frequencies of a wide variety of nanomechanical resonators and so design devices with resonant frequencies in the frequency range of interest.

2.1 Flexural Modes of Beams

The flexural modes of a simple doubly-clamped beam resonator can be derived from the equations for simple harmonic motion (SHM) to which a driving force, F , and a damping term, γ , are added. The starting point for describing their motion is the equation of motion for an undamped simple harmonic oscillator,

$$m\ddot{u}(t) + ku(t) = 0, \quad (2.1.1)$$

where m and k are the beam's mass and spring constant respectively and u is its displacement. In the case of our beam we need to add a sinusoidal driving force $F e^{i\omega t}$, and a damping term $\gamma \dot{u}$. Using the relationship $\omega_0^2 = \frac{k}{m}$ we can include the frequency of the beam to give the response of a damped driven beam as,

$$\ddot{u}(t) + \gamma \dot{u}(t) + \omega_0^2 u(t) = \frac{F e^{i\omega t}}{m}. \quad (2.1.2)$$

If we use the solution that at $F = 0$, $u(t) = u_0 e^{i\omega t}$ then we get the quadratic equation,

$$-\omega^2 + i\gamma\omega + \omega_0^2 = 0 \quad (2.1.3)$$

which can be solved to give,

$$\omega = i\frac{\gamma}{2} \pm \omega_0 \sqrt{1 - \frac{\gamma^2}{4\omega_0^2}}. \quad (2.1.4)$$

For the case where the damping is small the relation $Q = \omega_0/\gamma$ can be

used to give the natural frequency of the beam as,

$$\omega'_0 = \omega_0 \sqrt{1 - \frac{1}{4Q^2}}, \quad (2.1.5)$$

where $Q = \frac{\omega_0}{\gamma}$ is the quality factor of the beam. Inserting this into Equation 2.1.2 defines the displacement with respect to the Q factor as,

$$u(t) = u_0 \exp\left(-\frac{\omega_0 t}{2Q}\right) \cos(\omega'_0 t). \quad (2.1.6)$$

This shows that for a case where $Q \gg 1$ than it can be treated as a simple harmonic oscillator with $\omega'_0 \approx \omega_0$.

The next step is to set the force F in Equation 2.1.2 to a driving force, F_d and use the solution $u(t) = Re^{i\omega_d t}$, to find the response, R , of the beam as,

$$R = \frac{F_d/m}{\omega_0^2 - \omega_d^2 + \frac{i\omega_0\omega_d}{Q}} \quad (2.1.7)$$

where ω_0 is the resonant frequency and ω_d is the drive frequency. This shows that when the beam is being driven at its resonant frequency ($\omega_d = \omega_0$) the beam will have a maximum response of $R_{max} = \frac{QF_d}{m\omega_0^2}$. The response of the beam is therefore directly proportional to the Q factor of the beam, meaning that it is easier to measure the displacement of a beam with a higher Q factor. In addition a higher Q factor means it is easier to precisely measure the resonant frequency. Figure 2.1 shows a graphical representation of Equation 2.1.7 for a range of Q factors.

Now that we understand the motion of the beam we can start to determine the natural frequency ω_0 . The situation for a device like ours

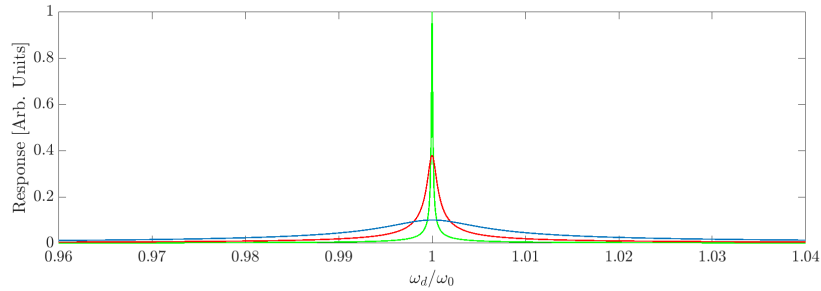


Figure 2.1: Figure showing the response of the resonator for 3 different Q factors, 100 (blue line), 1000 (red line) and 10000 (green line). It can be seen that higher Q factors result in a larger response and a better defined peak.

which has cross sections that are a lot smaller than its length is described by Bokaian [8] and is explained here. By orientating the beam so that its length is on the x-axis, its width is on the y-axis and the movement is in the z direction then it is possible to derive a simple equation of motion,

$$EI \frac{\partial^4 z}{\partial x^4} - T_0 \frac{\partial^2 z}{\partial x^2} + \rho A \frac{\partial^2 z}{\partial t^2} = 0, \quad (2.1.8)$$

with E being the Young's modulus, I is the moment of inertia, T_0 is the intrinsic tension in the beam, ρ is its density and A is the cross sectional area. However this equation is only true if: (a) there is no external drive, (b) no damping, (c) the beam is in the linear regime and (d) when any complicated mechanical effects are ignored. This is analogous to the Euler-Bernoulli equation but with a tension term added. As we are working with a doubly clamped beam we can impose

boundary conditions where the displacement at each end is zero i.e.,

$$\begin{aligned} z(0, t) = z(L, t) &= 0 \\ \frac{\partial z}{\partial x}(0, t) = \frac{\partial z}{\partial x}(L, t) &= 0 \end{aligned} \tag{2.1.9}$$

in which L is the length of the beam. The general solution for this equation takes the form of a sum over all the modes (represented by the subscript n) and looks like,

$$z_n(x, t) = \sum_n u_n(t) g_n(x) \tag{2.1.10}$$

where

$$u_n(t) = u_{0n} e^{i(\omega_{0n} t + \phi_n)}$$

and $g_n(x)$ is the spatial function of the n^{th} mode. Substituting Equation 2.1.10 into Equation 2.1.8 we get,

$$EI \frac{\delta^4 g}{\delta x^4} - T_0 \frac{\delta^2 g}{\delta x^2} - \rho A \omega_{0n}^2 g(x) = 0, \tag{2.1.11}$$

as the equation the spatial dependence must satisfy.

These equations must be solved for a number of different situations namely: the situation where the tension dominates over the bending rigidity i.e. $T_0/EI \gg 1$, known as the string limit; the opposite situation where the bending rigidity dominates over the tension i.e. $EI/T_0 \gg 1$, known as the bending limit. Finally the situation when neither tension or bending rigidity dominate and both need to be taken into account.

The case for the string limit is the simplest to solve as the 4th order term in Equation 2.1.8 can be ignored and we are left with a simpler 2nd order differential equation. The solution to this takes the form of $g(x) = \sin \frac{k_n x}{L}$. If we substitute this into Equation 2.1.11 we get,

$$\omega_{0n} = \frac{k_n}{L} \sqrt{\frac{T_0}{\rho A}} \quad (2.1.12)$$

and

$$g_n(x) = u_{0n} \sin \left(\sqrt{\frac{\rho A}{T_0}} \omega_{0n} x \right), \quad (2.1.13)$$

where $k_n = n\pi$. This is a fairly simple solution and is the same as that of plucking a guitar string.

The case for the bending limit is slightly more complicated as it involves a 4th order differential equation and it has 4 possible solutions namely $g(x) = \sin, \cos, \sinh$ or $\cosh(\frac{kx}{L})$, choosing any of these gives values for k_n of ,

$$k_n = \beta_n L \quad \text{where} \quad (2.1.14)$$

$$\beta_n = \left(\frac{\rho A}{EI} \right)^{\frac{1}{4}} \sqrt{\omega_{0n}}$$

and the general solution has the form,

$$g_n(x) = c_1 \sin(\beta_n x) + c_2 \cos(\beta_n x) + c_3 \sinh(\beta_n x) + c_4 \cosh(\beta_n x), \quad (2.1.15)$$

where c_1, c_2, c_3, c_4 are constant coefficients. The boundary conditions previously mentioned imply that the values of $\beta_n L$ need to satisfy the

equation,

$$\cos(\beta_n L) \cosh(\beta_n L) - 1 = 0. \quad (2.1.16)$$

This can be solved using standard trigonometric identities to obtain values of $\beta_n L = 4.73, 7.85, 10.99, 14.14, \text{ etc} = k_n$. Using these values along with Equation 2.1.14 we are able to calculate the fundamental angular frequency of the beam for the bending limit as,

$$\omega_0 = \left(\frac{4.73}{L}\right)^2 \sqrt{\left(\frac{EI}{\rho A}\right)}. \quad (2.1.17)$$

Next we consider the situation when bending rigidity and tension are of similar importance. In this case the solutions are more complicated. The solution to this problem is outlined by Bokaian [8] and a brief outline is given here.

We start by substituting the solutions we used for the bending limit into Equation 2.1.8 to get two sets of equations; firstly for the hyperbolic equations we get,

$$k_1 = \sqrt{U + \sqrt{U^2 + \Omega^2}} \quad (2.1.18)$$

and for the normal, real, equations we get,

$$k_1 = \sqrt{-U + \sqrt{U^2 + \Omega^2}}, \quad (2.1.19)$$

where $U = \frac{T_0 L^2}{2EI}$ and $\Omega = \omega_0 L^2 \sqrt{\frac{\rho A}{EI}}$; these are known as the tension and frequency parameters respectively. These give a general solution to

the mode function $g(X)$ as

$$g(X) = d_1 \sinh(k_1 X) + d_2 \cosh(k_1 X) + d_3 \sin(k_2 X) + d_4 \cos(k_2 X) \quad (2.1.20)$$

where k_1, k_2, k_3, k_4 are constant coefficients and X is the ratio $\frac{x}{L}$ and is therefore dimensionless. By applying the boundary conditions mentioned in Equation 2.1.9 we get the equation

$$\Omega + U \sin(k_2) \sinh(k_1) - \Omega_n \cos(k_2) \cosh(k_1) = 0. \quad (2.1.21)$$

This can be solved numerically for a given set of variables i.e.: tension, length, Young modulus, moment of inertia, density and cross-sectional area to obtain values for the eigenfrequencies of the beam.

An expression is derived in reference [8] which can be used to numerically estimate the frequencies f_n of the beam,

$$f_n = \frac{\pi}{8} (2n+1)^2 \frac{1}{L^2} \sqrt{\frac{EI}{\rho A}} \sqrt{1 + \frac{0.97 T_0 L^2}{(n+1)^2 \pi^2 EI}} \quad (2.1.22)$$

this provides the upper bound for the fundamental mode of the beam ($n=1$) the 0.97 comes from a coefficient defined in [8] which depends only on the type of end conditions e.g. where it is clamped at both ends as in our situation.

Other approximations for the fundamental frequency of a beam have also been derived, for example in [9] f_0 is estimated to be

$$f_0 = \frac{2\pi}{L^2} \sqrt{\frac{EI}{3\rho A} \left(1 + \frac{L^2 T_0}{4\pi^2 EI} \right)} \quad (2.1.23)$$

for the $n=1$ harmonic. Comparing these shows a difference of a few percent which considering the accuracy to which it is possible to estimate the properties of the beam, this level of agreement is sufficient. By using one or both of these equations it is possible to easily estimate the frequencies of the resonators using experimentally obtainable values. It can be seen that to maximise the fundamental frequency for a particular material we want to maximise the tension in the beam and keep its dimensions as small as possible.

2.2 Torsional Modes of Paddle Resonators

For the torsional modes of the resonator, Equation 2.1.22 is no longer accurate as we can no longer consider the beam moving as a simple harmonic oscillator. Instead we need to consider the resonator's moment of inertia. The frequency of the torsional mode of a beam is defined by,

$$f_0 = \frac{1}{2\pi} \sqrt{\frac{\kappa}{I}}, \quad (2.2.1)$$

where f_0 is the beams resonant frequency, κ is its spring constant and I is its moment of inertia.

To calculate the triple paddle torsional resonator's moment of inertia we need to split the resonator into different parts i.e. the beam, I_b , and the paddles, I_{bp} for the larger paddles and I_{sp} for the smaller paddle (Figure 2.2) . The total inertia of the resonator is given by the sum of the individual parts $I = I_b + 2I_{bp} + I_{sp}$.

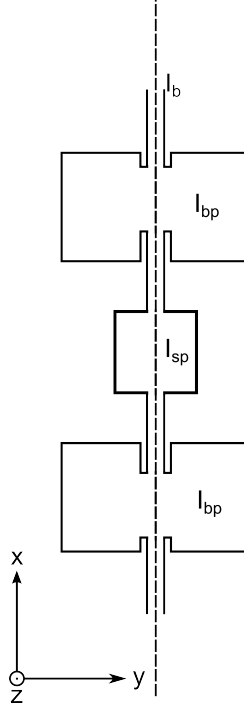


Figure 2.2: Figure defining the paddles and axis used in the equations of motion defined in this section. The equations are valid for the beam being rotated along the centre of the beam donated by the dashed line.

The moment of inertia of a solid object is defined by the integral,

$$I = \int \rho x^2 dv, \quad (2.2.2)$$

where ρ is density and x is the length of the axis the beam is being rotated along. Therefore a doubly clamped beam with width, w (in the y axis), and thickness, h (in the z axis), will have a moment of inertia along the central beam (Figure 2.2) equal to,

$$I = \int_{-\frac{w}{2}}^{\frac{w}{2}} \rho A y^2 dy + \int_{-\frac{h}{2}}^{\frac{h}{2}} \rho A z^2 dz \quad (2.2.3)$$

where A is the cross sectional area of the axis that is being twisted.

This can be solved to give,

$$I_b = \frac{\rho A_y w^3}{12} + \frac{\rho A_z h^3}{12}, \quad (2.2.4)$$

which can be simplified to,

$$I_b = \frac{m(w^2 + h^2)}{6}, \quad (2.2.5)$$

where m is the mass of the beam.

For the paddles the thickness of the resonator can be ignored as it is a lot smaller than the width, this results in the paddles moment of inertia being,

$$I = \int_{-\frac{w}{2}}^{\frac{w}{2}} \rho A y^2 dy \quad (2.2.6)$$

which can be solved to give,

$$I = \frac{mw^2}{12} \quad (2.2.7)$$

For a triple paddle design with paddles that are a lot wider than the beam, the beam's moment of inertia can be neglected giving the total moment of inertia as,

$$I = \frac{\rho h}{12} [2l_{bp}w_{bp} + l_{sp}w_{bp}]. \quad (2.2.8)$$

As our resonator only clamps to the substrate where it is a thin beam, the torsional spring constant is simply that of a rectangular beam i.e.,

$$\kappa = \frac{2KG}{w_b}, \quad (2.2.9)$$

where K is the torsional moment of the beam and $G = \frac{E}{2(\nu_p+1)}$ is the shear modulus of the beam with ν_p being Poisson's ratio. For a beam with a rectangular cross section, K is defined by [10]

$$K = w_b h_b^3 \left[\frac{1}{3} - 0.21 \frac{h_b}{w_b} \left(1 - \frac{w_b^4}{12h_b^4} \right) \right]. \quad (2.2.10)$$

Combining values for κ and I gives,

$$f = \frac{1}{2\pi} \sqrt{\frac{24KG}{l_b \rho t [2l_{bp} w_{bp} + l_{sp} w_{bp}]}}. \quad (2.2.11)$$

For a single paddle resonator this simplifies to,

$$f = \frac{1}{2\pi} \sqrt{\frac{24KG}{l_b \rho t l_p w_p}}, \quad (2.2.12)$$

where the subscript p refers to the single paddle. This shows that unlike for the flexural modes all the dimensions of the beam are important meaning that these have to be carefully considered when designing the resonator. It also shows that the tension of the beam does not affect the frequency of the beam whereas the shear modulus does.

2.3 Flexural Modes of Square and Circular Membranes

Finally we look at the equations of motion for a membrane. These membranes can be used to form moveable plates of parallel plate capacitors. Here we consider a membrane as a thin sheet clamped to the

substrate at all edges, this gives us the boundary conditions that at the edges of the membrane the displacement in the z axis is equal to zero. There are two different shapes of membranes that we are interested in, either rectangular or circular membranes. A solution by DasGupta and Hagedorn [11] sets the starting point as needing to solve the wave equation,

$$\frac{\partial^2 z}{\partial t^2} - c^2 \nabla^2 z = 0, \quad (2.3.1)$$

where $c = \sqrt{T/\mu}$, where $T = \sigma h$ is tension, and $\mu = \rho h$ is the membranes mass per unit length for a membrane with inbuilt strain σ , density, ρ , and thickness, h . To solve this equation we need to use different coordinate systems depending on the membrane shape. For rectangular membranes we can use Cartesian co-ordinates i.e. $z(x, y, t)$ but for the circular membranes we need to use polar co-ordinates i.e. $z(r, \phi, t)$. In both cases the final solution depends on the mode numbers m or n . Because of their geometry membranes can have resonances in two dimensions, for circular membranes the n modes refers to the nodes being radial whilst the m modes refer to the nodes being along the radius. For rectangular membranes the n modes and m modes refer to the nodes being along different axes (i.e. width or length), these definitions are shown in Figure 2.3.

For the case of a rectangular membrane with sides of length a and b

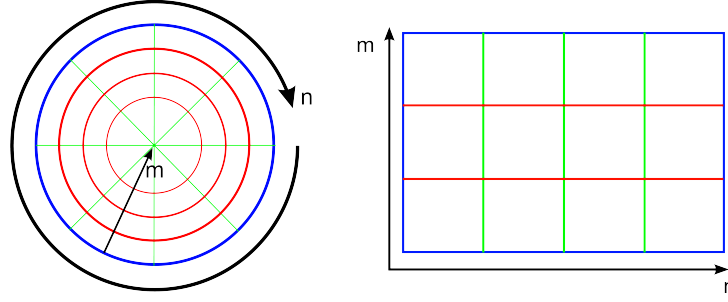


Figure 2.3: Figure defining the mode numbers m and n for circular and rectangular membranes.

then Equation 2.3.1 can be written in Cartesian coordinates as,

$$\frac{\partial^2 z}{\partial t^2} - c^2 \left(\frac{\partial^2 z}{\partial x^2} + \frac{\partial^2 z}{\partial y^2} \right) = 0. \quad (2.3.2)$$

As the membrane is clamped around the edges we get boundary conditions,

$$z(0, y, t) = z(a, y, t) = z(x, 0, t) = z(x, b, t) = 0 \quad (2.3.3)$$

we can solve this by setting $z(x, y, t) = Z(x, y)e^{i\omega t}$ to obtain the equation,

$$\frac{\partial^2 Z}{\partial y^2} + \frac{\partial^2 Z}{\partial x^2} - \frac{\omega^2}{c^2} Z = 0, \quad (2.3.4)$$

which has the general solution,

$$\begin{aligned} Z(x, y) = & A \cos(\alpha x) \cos(\beta y) + B \sin(\alpha x) \cos(\beta y) + \\ & C \cos(\alpha x) \sin(\beta y) + D \cos(\alpha x) \cos(\beta y), \end{aligned} \quad (2.3.5)$$

which if combined with the boundary conditions in Equation 2.3.3 gives a solution to the $(n, m)^{th}$ mode of the membrane as,

$$Z(x, y) = D \cos(\alpha x) \cos(\beta y), \quad (2.3.6)$$

where $\alpha = \frac{m\pi}{a}$ and $\beta = \frac{n\pi}{b}$.

Combining Equations 2.3.4 and 2.3.6, gives the frequency for a rectangular membrane as [11],

$$\omega_{n,m} = \pi c \sqrt{\frac{m^2}{a^2} + \frac{n^2}{b^2}}. \quad (2.3.7)$$

or for a square membrane where $a = b$,

$$\omega_{n,m} = \pi c \sqrt{\frac{m^2 + n^2}{a^2}}. \quad (2.3.8)$$

Next we need to look at the equations for a circular membrane. The wave equation for a circular membrane with a radius of a is [11],

$$\frac{\partial^2 z}{\partial t^2} - c^2 \left(\frac{\partial^2 z}{\partial y^2} + \frac{\partial z}{r \partial r} + \frac{\partial^2 z}{r^2 \partial \phi^2} \right) = 0. \quad (2.3.9)$$

For a circular membrane it is harder to find a solution to Equation 2.3.9 as as we only have a single boundary condition setting the displacement at the edges of the membrane (where $r = a$) as 0, i.e.,

$$z(a, \phi, t) = 0. \quad (2.3.10)$$

To get around this problem we can use the condition that at all points the displacement of the amplitude must be finite.

The solution $z(r, \phi, t) = W(r, \phi)e^{i\omega t}$ can be used to change Equation 2.3.9 to a solvable equation,

$$W + \frac{c^2}{\omega} \left(\frac{\partial^2 W}{\partial r^2} + \frac{\partial W}{r \partial r} + \frac{\partial^2 W}{r^2 \partial \phi^2} \right) = 0. \quad (2.3.11)$$

The solution for W needs to have both radial (i.e. $\Phi(\phi)$) and azimuthal ($R(r)$) components meaning it will take the form $W(r, \phi) = R(r)\Phi(\phi)$.

Substituting this into Equation 2.3.11 gives,

$$\frac{\omega^2}{c^2} + \left(\frac{\partial^2 R}{\partial r^2} + \frac{1}{rR} \frac{\partial R}{\partial r} + \frac{1}{\Phi r^2} \frac{\partial^2 \Phi}{\partial \phi^2} \right) = 0. \quad (2.3.12)$$

It can be seen that for this to be solvable $\frac{\partial^2 \Phi}{\partial \phi^2}$ must be a constant giving us a value of $\Phi(\phi) = e^{im\phi}$. Inserting this into Equation 2.3.12 and simplifying with $v = \omega/c$ gives,

$$\frac{\partial^2 R}{\partial r^2} + \frac{\partial R}{r \partial r} + R \left(v^2 - \frac{m^2}{r^2} \right) = 0, \quad (2.3.13)$$

this is Bessel's equation, its solution can be written as,

$$R(r) = F J_n(vr) + G Y_n(vr), \quad (2.3.14)$$

where F and G are constants of integration and J_n and Y_n are the Bessel functions. As the Bessel functions are symmetrical, $J_n = J_{-n}$ and $Y_n = Y_{-n}$, we only need to consider positive values of n (plus $n=0$). While the value of J_m is always finite Y_m has a logarithmic singularity at $z = 0$ meaning that to ensure the boundary condition that the displacement of the membrane at all points is finite G must be zero meaning that,

$$R(r) = F_{n,m} J_n(vr). \quad (2.3.15)$$

Equation 2.3.15 can be combined with the boundary functions in Equation 2.3.10 to obtain an equation for the frequencies of a circular mem-

brane as [11],

$$\omega_{m,n} = (2m + 4n - 1) \frac{\pi c}{4a}. \quad (2.3.16)$$

2.3.1 Conclusion

The aim of this chapter was to provide an understanding of the dynamical properties of nanomechanical resonators when they are in the linear regime. To do this we looked at the equations of motion for a number of different resonator designs and were able to give equations to calculate the resonant frequencies of the flexural motion of beams (Equation 2.1.22), the torsional motion of paddle resonators (Equations 2.2.11 and 2.2.12) and both square and circular membranes (Equations 2.3.16 and 2.3.7 respectively). In addition to using these equations it is also possible to use finite element software such as comsol to model the resonators and therefore extract their resonant frequencies. It does this by splitting the resonator into a number of elements then finding the eigenfrequencies for the whole system. This was used for resonators in Chapters 6-8. It should be noted that the equations in this chapter are only accurate whilst the resonator is in the linear regime and would no longer be correct if the resonator is in the non-linear regime. Now that the equations of motion have been described the next Chapter looks at damping, γ , which plays an important role in the equations of motion for a nanomechanical resonator.

Damping Within Nanomechanical Resonators

Damping is one of the most important values when it comes to designing nanomechanical resonators. The most common parameter given when discussing damping of a resonator is its quality or Q factor. A resonator with an infinitely large Q factor would continue to resonate indefinitely without any reduction in amplitude as its movement would be undamped. Q factors of a few thousand are easily obtainable at room temperatures and atmospheric pressure. In fact a guitar string has a Q factor of around 3000 [12], and Q factors in the billions have been observed in the acoustic vibrational modes of a 5 kg single crystal silicon beam [13]. This chapter looks at a number of sources of damping, these either occur internally to the resonator, known as intrinsic dissipation, or externally, known as extrinsic dissipation.

3.1 Extrinsic Dissipation

Extrinsic damping involves how the resonator reacts with its surroundings whether this be with where it connects to the substrate or how it interacts with the detection mechanism. As these damping mechanisms occur in resonators of all sizes and at all temperatures, they have been studied extensively, so only a brief discussion is given below.

Fluid Friction

As with any object moving within a fluid, a resonator will lose energy due to friction between the resonator and the fluid. The method used to calculate the damping due to fluid friction depends on the size of the resonator and the density of the fluid it is moving in [14]. For objects mm and above in size and at atmospheric pressures, Navier-Stokes equations can be used, as the system can be treated as being in the continuum flow regime. However at pressures below 1 mbar the system can be considered to be in the free molecular flow regime. In the free molecular flow regime the interactions of individual gas molecules defines the damping. This means that the dissipation due to fluid friction is proportional to pressure, the thermal velocity of the gas atoms and the beam's properties, such that,

$$Q_{fluid}^{-1} = \frac{pA}{m_{eff}\omega_0 v}, \quad (3.1.1)$$

where, p is the pressure of the gas, A is the area of the object moving

through the fluid, m_{eff} , is the resonators effective mass, ω_0 is its resonant frequency and v is the thermal velocity of the gas particles [14]. It should be noted that the area used in this equation refers to the area of the resonator that is moving. This means that a torsional mode may have a lower value for dissipation due to fluid friction if the mode is such that not all of the resonator is moving i.e. only one of the paddles may be moving. Therefore care should be taken when comparing values of dissipation due to fluid friction. However at low temperatures it is likely that we will be working with a cryogenic vacuum and therefore it can be neglected. For room temperatures and pressures below around 1 mbar, dissipation due to fluid friction would still need to be considered as a possible source of dissipation.

Clamping Losses

Any resonator that is moving will generate acoustic waves, these can propagate through the clamping points into the substrate causing a dissipation of energy. One of the biggest problems with dissipation due to clamping losses is that it is effectively independent of temperature meaning that it limits the Q factor especially at low temperatures. For devices where the acoustic wave is of a similar length to the length of the beam the waves are mostly reflected back at the clamping points [15]. Therefore the dissipation is related to the aspect ratio, $\frac{t}{L}$ of the

thickness, t and length L such that [16],

$$Q_{cl}^{-1} \propto \frac{t^4}{L^5}. \quad (3.1.2)$$

What this means is that as we try to make devices with higher resonant frequencies (and therefore higher aspect ratios) the dissipation due to clamping losses will become greater and greater.

For torsional modes in a paddle resonator it is possible to reduce the dissipation by including 2 paddles either side of a central paddle that is moving (Figure 3.1) . These paddles act as counterweights and again stop the acoustic waves reaching the clamping points [17]. In addition to this it is possible to reduce clamping losses by careful fabrication of the clamping points [18].

Losses via Measurement System

The act of actuating and detecting the motion of a resonator can, in itself, cause dissipation. The magnetomotive method (which is discussed in Chapter 6) is a commonly used method for both actuating and detecting metallic NEMS, however this method causes dissipation. The dissipation arises from eddy currents, created by the magnetic field used to actuate the resonator, opposing the resonator's motion. The dissipation due to the magnetomotive method is given by the equation [19],

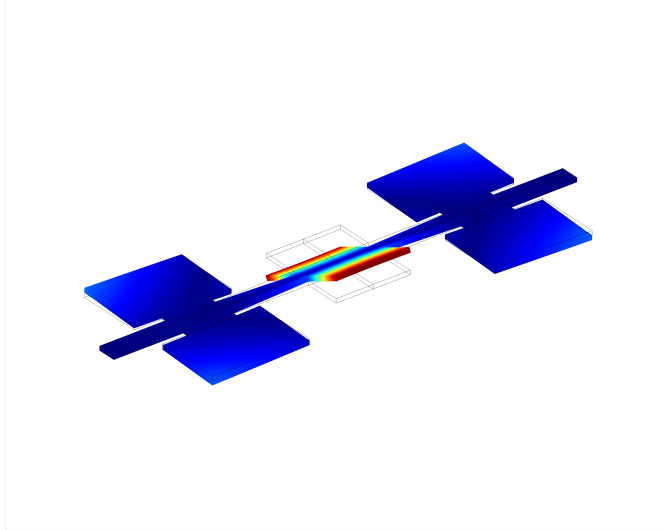


Figure 3.1: Comsol simulation of a triple paddle torsional resonator where only the middle panel is moving. The two larger paddles act as counterweights and therefore reduce clamping losses. The colours give an indication of displacement with blue being zero displacement and red being the maximum displacement

$$Q_{mag}^{-1} = \eta B^2, \quad (3.1.3)$$

where η is a constant that depends on the measurement set up and resonator properties, and B is the magnetic field in Tesla. This shows that we can increase the Q factor of the resonator by working at smaller magnetic fields. As this dissipation is temperature independent it is possible to experimentally calculate the value of η and therefore calculate the magnetomotive dissipation, $\frac{1}{Q_{mag}}$ for any results. This value can then be subtracted from the so called loaded quality factor Q_l to give an unloaded quality factor, Q where, $\frac{1}{Q} = \frac{1}{Q_l} - \frac{1}{Q_{mag}}$. The unloaded quality

factor is the quality factor of the resonator if we were able to measure it in zero magnetic field. Whilst it is possible to remove magnetomotive dissipation it is still advisable to use as small as magnetic fields as possible. In doing this the magnetomotive dissipation will be reduced but this will come at the cost of smaller signals meaning it could be hard to measure the displacement especially if small drive powers are also used.

Optical detection as described in Chapter 5 also causes dissipation through either heating of the resonator or due to the optical force of the laser light. Resonator heating is caused by the laser heating up an area of the resonator. This creates localized hot spots that cause the resonator to expand in these areas. To return the resonator to thermal equilibrium there will be a heat flow across the resonator. This heat flow causes a change in the localized strain of the resonator as it contracts and expands. This change takes mechanical energy from the system causing dissipation. The optical power of the laser hitting the resonator will also cause dissipation due to it applying a constant radiation force to the resonator. In order to reduce these sources of dissipation the ideal conditions will be to use as small as possible laser powers and use materials with low coefficients of expansion. Doing this will reduce dissipation however in reality we are normally limited by the minimum laser power to ensure lasing occurs and by the fact we have a limited choice in materials. This being said it has been previously

shown by this group to not be important for the types of resonators used in this work [20].

3.2 Intrinsic Dissipation

Intrinsic dissipation mechanisms originate from the material of the resonator. These include dissipation where an increase in the surface area (therefore an increase in the surface to volume ratio) of the resonator due to effects such as oxide layers or dangling bonds causes an increase in dissipation. This arises because the defects on the surface alter the strain on the resonator. The resonator then tries to return this strain field to its equilibrium position losing energy in the process. These effects can be reduced via careful fabrication however they are very hard, if not impossible, to eliminate completely.

Thermoelastic Dissipation

When a resonator has one of its modes actuated it undergoes expansion and contraction creating a strain field. This movement causes a local temperature field. The coupling of the strain field and the temperature field causes an irreversible energy loss as the resonator tries to return to its equilibrium position. This damping has been shown to be dependent on the resonator size and mechanical properties [21]. As the mechanical properties are temperature dependent the dissipation

is also temperature dependent but always non-zero. It is thought that for the torsional modes of a resonator thermoelastic dissipation is negligible [22]. This is because for a purely torsional mode the resonator undergoes very little compression or expansion, and in the case where there is a central paddle what little expansion or compression occurs can therefore be thought to be negligible [6]. Where dissipation could arise is: (a) where the response of the resonator is not purely torsional rather a combination of a flexural and torsional mode and (b) where the paddles are flexing and therefore creating a strain field. This means that whilst it is likely to contribute less to the damping in a torsional mode it can not be completely ignored.

Two Level Systems

One of the most interesting and important intrinsic damping mechanisms at low temperatures is known as dissipation due to two level systems (TLS). This is because it is expected that it will affect resonators of any size and material. This dissipation is temperature dependent at low temperatures with this dependence strongly varying between different materials. Dissipation due to TLS was first investigated simultaneously by Anderson et al. [23] and Philips et al. [24]. They proposed a system that is commonly referred to as the standard tunnelling model (STM). This model predicts that any material will contain a number of atomic defects within in it. These defects result in a range of potential wells

with different energy levels. After being strained the system tries to restore the material to its original energy state by correcting these defects. It does this by moving atoms or molecules between defect states. At the lowest temperatures only the two lowest energy levels (E_1 and E_2) need to be considered meaning that the defects can be represented by a double well potential, hence the name dissipation due to two level systems.

These two energy levels (shown in Figure 3.2) have a energy difference, Δ , and are separated by a tunnelling energy, Δ_0 , which is defined by,

$$\Delta_0 = \hbar\Omega e^{-\lambda}, \quad (3.2.1)$$

where $\hbar\Omega$ is the average energy of the wells and λ is a tunnelling parameter that depends on the mass, m , of the tunnelling particle, the distance, d , between the wells and the height, V , of the potential barrier such that $\lambda = \sqrt{d(mV/\hbar^2)}$. As the properties of these potential wells varies depending on the type of defects there are a number of different double wells that can exist. This results in a range of values of Δ and Δ_0 , however as all levels of Δ are equally likely the energy difference of the whole system averages to zero. As the energy difference across the system averages to zero the systems tries to relax to its equilibrium position. In does this by atoms tunneling accross the potential barriers. This results in the atoms moving in 3N-dimensional space [23] and therefore gaining or losing energy while only moving distances far less then the lattice constant of the material. To allow for this tunneling

the system needs to absorb energy from the environment. As we are at low temperatures and $E = k_B T$ the energy of these absorptions is likely to be in the order of a meV [24]. This energy is absorbed via the interactions of photons, phonons or electrons.

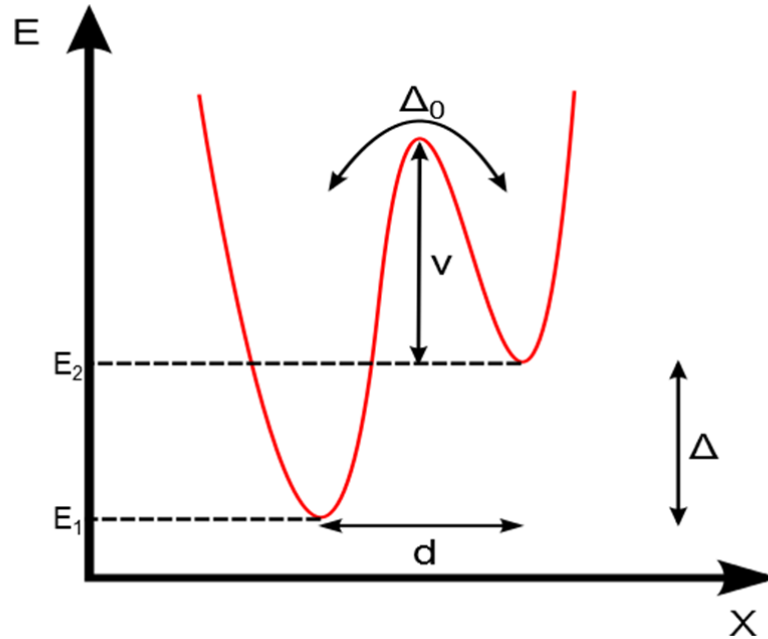


Figure 3.2: Diagram showing a representation of a TLS which has two potential wells with energy levels E_1 and E_2 with an energy difference of Δ . They are separated by a barrier of height V resulting in a tunnelling energy of Δ_0

There are two ways that these interactions can happen namely resonant interactions or relaxation interactions. In a resonant interaction the motion of the resonator is directly coupled to the TLS. This means that the TLS can directly absorb a phonon or electron from the movement of the resonator. This causes a particle or atom in the lower well to move

up to the upper well. In order for the average energy to remain at zero a particle must lose energy which it does via the emission of a phonon or photon [23, 24]. This results in damping of the resonator's motion. For this interaction to take place the resonator must have a frequency that ensures its energy is greater than the energy difference Δ_0 . This means that the strength of this interaction depends on the ratio $\hbar\omega_0/T$ where ω_0 is the frequency of a particular mode of the resonator and T is its temperature. When this ratio is bigger than 1 it is possible for these interactions to occur. For a resonator with a mechanical frequency of around 10 MHz this would happen at temperatures below around 0.5 mK, which is around 100 times less than the temperature which is easily achievable with dilution refrigeration techniques. This means that very few resonant absorptions will take place for the sort of systems we will be looking at. However it is possible that they will play a role in systems where the mechanical frequencies are in the GHz range.

This does not mean that dissipation due to TLS can be neglected however as it is still possible for interactions to take place in the regime where $\hbar\omega_0/k_B T \leq 1$. This is because the motion of the resonator creates a strain field across the resonator [24]. This strain field causes a shift in the thermal equilibrium of the resonator. To compensate for this the energy levels of the TLS (E_1 and E_2) will shift causing the emission of energy via a phonon or photon, again causing the system to lose energy.

The strength of this relaxation interaction depends on how long this relaxation takes. This time, τ , depends on the the energy level difference Δ_0 [24]. As previously mentioned there is a large range of values of Δ_0 resulting in a large spread of values of τ . The amount of energy loss via this process is greatest when the mechanical frequency of the resonator is the same as this relaxation time. In addition to τ being dependent on Δ_0 the minimum possible relaxation time, τ_{min} , is also dependent on the temperature of the TLS. This means that this is a temperature dependent process with dissipation decreasing below the temperature where $\tau_{min} \gg \omega$. At higher temperatures τ_{min} reaches a constant value resulting in a temperature plateau in the dissipation. This crossover happens at the temperature, T^* , when $\tau = \omega$ [26].

As mentioned earlier, for dissipation due to TLS to occur it requires mediating phonons or electrons and it is the properties of these that go some way to defining the temperature dependence of the dissipation. For the case of phonons the dissipation can be related to the heat capacity and thermal conductivity of the solid as this defines the properties of the mediating phonons [24]. What this means is that for the case of insulating amorphous solids there will be a cubic temperature dependence. For an electron mediated process the temperature dependence is related to the decay time of thermally excited electrons and therefore it is expected that there will be a linear temperature dependence [24].

In addition to causing dissipation, TLS also cause a shift in the me-

chanical frequency of the resonator. This is because the TLS alters the sound velocity of the resonator material which in turn effects the stiffness and density. Regardless as to whether or not the resonator is made from an insulator or a metal the frequency shift will be logarithmic with it decreasing either side of a maximum at T^* .

These T^3 and T temperature dependences are only valid for polycrystalline materials. For the case of single crystal structures it is expected that the temperature dependence would be markedly different. For the single crystal case it is assumed there is only a single source of defects, this means that there is only one value of Δ_0 [27]. These defects relax via a acoustic phonon emission with an energy of $\hbar\omega$, this means that the temperature dependence of dissipation due to these relaxation mechanisms depends on the number of thermal phonons in the system i.e. it is analogous to the Bose-Einstein distribution. This results in a prediction that the temperature dependence for a single crystal resonator will be [27],

$$\frac{c}{k_B T} e^{-\frac{2\Delta}{k_B T}} \quad (3.2.2)$$

where c is a constant that relates to the properties of the resonators material, and effectively defines how strong the coupling is between the phonon bath and the defect state. All the above dependencies are only valid for temperatures below the crossover temperature T^* . As mentioned earlier for amorphous and metallic resonators the dissipation due to TLS plateau's due to the relaxation time τ reaching a maximum.

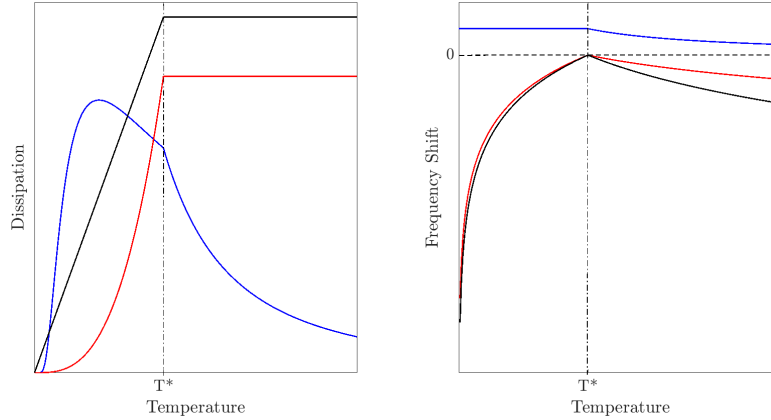


Figure 3.3: Figures giving an indication to the temperature dependences of the dissipation and frequency shifts due to TLS for. Black lines show the linear dissipation dependence found in metallic solids, red lines show the cubic dependence found in amorphous solids and red lines show the dependence for single crystals as given by Equation 3.2.2. Lines give an indication to the dependences only and both scales are arbitrary and the cross over temperature T^* is for indication purposes only.

However for single crystal resonators the dissipation does not plateau. This is because at high temperatures relaxation absorption dominates as $T \gg \frac{E}{k_B}$. This means that at high temperatures the dissipation follows a T^{-2} dependence [27]. Figure 3.3 shows how the temperature dependence varies for the 3 different forms of material.

There are problems with all these models when the dimensions of the resonator are scaled down. In the case of amorphous solids reducing the dimensions of the resonator can restrict the mediating phonons, with the phonon wavelength being around a few 100 nm. This means that in a nanomechanical resonator the phonons will be one or two di-

mensional which could result in a reduction in temperature dependence to approximately a linear or quadratic dependence. Another key issue is the surface to volume ratio of the resonator. As the resonator dimensions are reduced the surface to volume ratio becomes greater and greater. This means that the role of surface defects becomes more relevant. As an example we can consider the case of comparing an MBE grown single crystal aluminium resonator with an e-beam evaporated polycrystalline one. Whilst the MBE grown aluminium should result in a resonator with no internal defects the surface will have a number of defects due to the fabrication procedure introducing oxidization. Scanning electron microscopy (SEM) of the surface of the monocrystalline aluminium shows that this creates an aluminium oxide layer with a grain size of around 50 nm. This grain size is similar to what is expected from electron beam evaporated aluminium [28]. If we consider a beam 10 μm long by 300 nm wide by 30 nm thick then around 80% of the grain boundaries in an oxidized polycrystalline material will be on the surface therefore also exist on an oxidized monocrystalline surface. Whilst the basic theory behind TLS seems to be well understood there is a lot of uncertainty behind the finer points of the model. In particular the temperature dependence is not well understood and while work has qualitatively supported the model there has been a lack of quantitative work supporting it. In particular there has been a number of problems achieving the predicted cubic and linear temperature dependences as

well as the exponential dependence expected for single crystals. The next section considers research which has disagreed, at least in part, with the standard tunnelling model (STM).

3.3 Other Works on Dissipation in Micro- and Nanomechanical resonators

This section looks at earlier research on damping of nanomechanical resonators for a range of different materials. This will allow us to be able to see if the theoretical predictions made earlier are accurate as well as allowing us to compare the results presented later with other work and therefore give us an idea as to the quality of our devices.

There have been a number of works looking at damping within a range of materials some of these are summarised in Table 3.1, however very little work has been done on single crystal structures. Work on single crystal structures would be particularly interesting as it would help us better understand the standard tunnelling model. One paper on single crystal structures is by Tao et al. [32] who looked at diamond resonators. They looked at both single crystal and polycrystalline cantilevers with a range of dimensions but with lengths, widths, and thickness in the 100 μm , 10 μm and 100 nm range respectively.

Figure 3.4 shows how the Q factor of a number of different cantilevers

Resonator	f_0 [MHz]	Q	κ_0 [fm]
Gold nanobeam at 40 mK [29]	7.38	25000	45
Silicon nitride nanobeam at 40 mK [30]	7.3	1000000	57
Aluminium beam at 4.2 K [31]	7.1	5000	43
Aluminium drum at 40 mK [4]	10.7	36000	4.1
Silicon nitride torsional resonator at 300 K	8	800	63
Diamond cantilever at 93 mK [32]	6	5900000	1.1
Silicon nitride membrane at 1.2 K [20]	2.2	50000	1.2

Table 3.1: Table showing fundamental frequencies (f_0), Q factors and zero point motion (κ_0) of a range of resonators, zero point motion is either taken from the reference or calculated using $\kappa_0 = \sqrt{\hbar/(2m_{eff}f_0)}$ where m_{eff} is the effective mass of the resonator. The silicon nitride torsional resonator is the one measured in this work and discussed in Chapter 6.

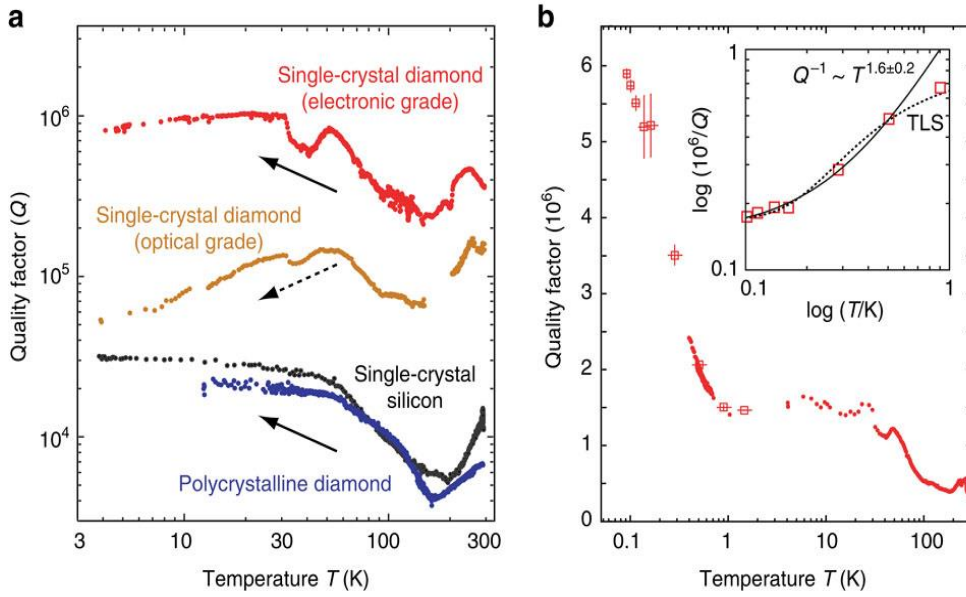


Figure 3.4: Figures showing how the Q factor of a number of different diamond or silicon cantilevers varies against temperature. a) Shows Q factors above 3 K while b) shows Q factors down to 100 mK for the electronic grade single-crystal diamond cantilever. Reproduced from [32].

varies with temperature. It can be seen that at room temperature the single crystal cantilevers have Q factors over 10 times that of polycrystalline diamond or even single crystal silicon.

As the results shown in Figure 3.4a are for temperatures above 4 K it is not expected that there will be any temperature dependant dissipation due to TLS. This is because it is expected that at high temperatures dissipation due to TLS is thought to be negligible. It is quite difficult to compare the Q values of the different resonators as there are marked differences in the dimensions of the cantilevers. As was seen earlier dissipation due to mechanisms such as fluid friction and clamping losses are strongly dependent on the device dimensions. That being said the

difference in Q factor between the single crystal and polycrystalline diamond is larger than would be expected from just a change in device dimensions. The authors suggest that at high temperatures the dissipation is due to surface friction, with the polycrystalline diamond having more defects on the surface therefore having a higher surface to volume ratio.

The low temperature response for the single crystal diamond can be seen in Figure 3.4b and shows a $Q^{-1} \propto T^{1.6}$ relationship. This is markedly different to what is expected from the STM. What is equally surprising is that for a number of resonators they found that the Q factor actually dropped below 4K. Whilst the authors say that fabrication differences could account for this it is hard to explain considering the wealth of evidence that suggests at low temperatures it is normal for the Q factor to increase.

Whilst the work by Tao et al. may not help our understanding of the STM it does show that single crystal structures (at least in the case of diamond) do significantly increase the Q factor of a resonator. However in diamond the dissipation is thought to be due to relaxation via phonon emission whereas in aluminium it would be via electrons. Therefore it is not guaranteed that the same dependencies would be seen.

Whilst there has been no work looking at single crystal metals, there has been a number of works that have studied polycrystalline metallic resonators. Recently there have been many studies looking at alu-

minium resonators as thanks to its superconducting properties it is thought that aluminium could be useful in microwave coupling experiments [4, 31, 33, 34]. What is interesting about superconductors is that it is expected, that due to the electrons at the Fermi surface being in a superconducting state they are no longer responsible for the relaxation of the TLS. This means it is expected that relaxation will still be via phonons and therefore have a T^3 dependence.

Sulkko et al., looked at aluminium beams with lengths, widths and thickness in the 10 μm , 100 nm and 100 nm range respectively [34]. They found that contrary to expectations there was a linear relationship between dissipation and temperature below around 1 K before plateauing below around 100 mK. One reason for the departure could be due to the fact the beam's small dimensions result in the mediating phonons being one dimensional. The plateau was probably caused by some form of temperature independent mechanism such as clamping losses. As this experiment used capacitive drive and detection they were always using low currents so that the aluminium was always in the superconducting regime.

In contrast to the work by Sulkko et al., Lulla et al. looked at aluminium on silicon resonators when the aluminium was in both its normal and superconducting state [31]. They used the magnetomotive technique on a "goal post" design of resonator with posts 3 μm long and the crossbar was 7 μm long, the beams are 250 nm wide and 150 nm thick of which

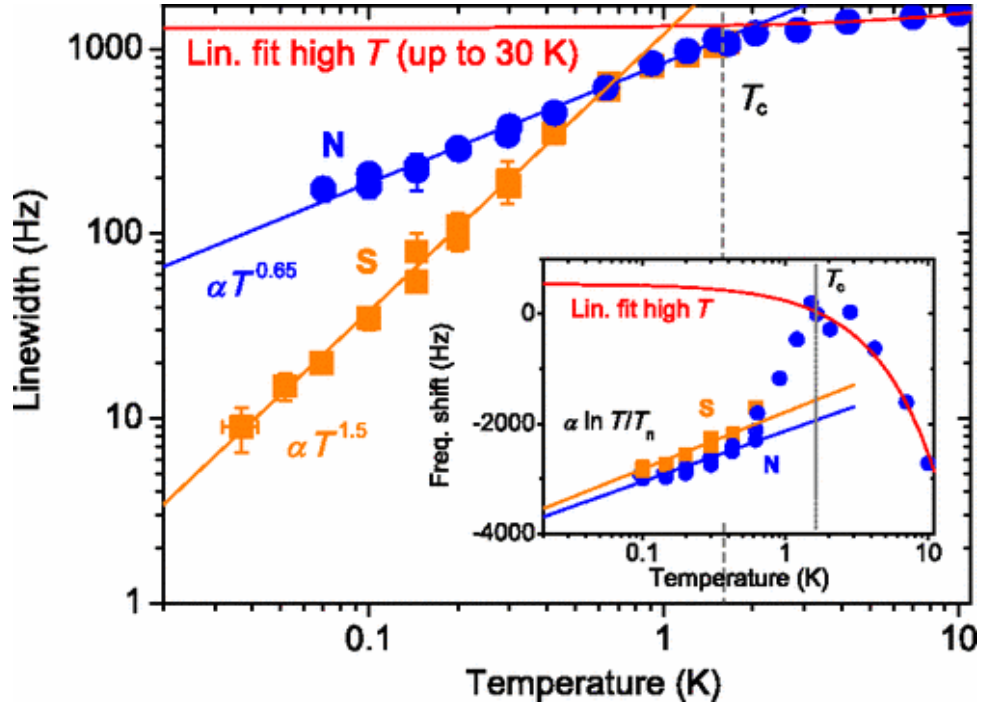


Figure 3.5: Temperature dependence of a aluminium goal post resonator in both the normal (blue lines, circle points) and superconducting (orange lines, square points) states. The term linewidth is analogous to dissipation with $Q=f_0/\text{linewidth}$ where $f_0 = 7.07$ MHz. Reproduced from [31].

30 nm is aluminium. By varying the drive current and magnetic field they could keep the aluminium in the normal or superconducting state.

Figure 3.5 shows that there is a marked difference between the temperature dependence of the dissipation between the normal and superconducting states. Below around 700 mK the dissipation has a $T^{\frac{3}{2}}$ relationship for the superconducting state but a $T^{\frac{2}{3}}$ relationship for the normal state. As with the work by Sulkkio et. al it is expected that due to the size of the structures any phonons will be 1D meaning that a linear temperature dependance would be expected and it is hard to explain the deviation from this. An important difference between Lulla's

work and Sulko's and our work is that in Lulla's work the resonator included a silicon layer. This silicon layer could have a significant effect on the Q factor of the resonator especially with regard to its temperature dependence. This can be seen by comparing similarly sized gold resonators both with [35] and without [29] a silicon nitride layer. A marked difference in the temperature dependence is observed between these layers with a $T^{1.5}$ dependence with the silicon nitride and a $T^{0.5}$ without. This suggests that when the aluminium is in the superconducting state the dissipation due to TLS is dominated by the silicon nitride layer suggesting that the aluminium layer has very little dissipation due to TLS when it is superconducting.

Haust et al. also looked at the difference between superconducting and normal state aluminium with particular reference to the role of electrons in TLS, however this was in bulk aluminium [36]. They limited their investigations to looking at the change in sound velocity as the temperature was changed and found a marked difference between when the aluminium was in its superconducting or normal state. They found that the sound velocity is considerably larger in superconducting aluminium. What this appears to show is that electrons do play a role in the dissipation due to TLS, this is because in a superconductor the electrons would form Cooper pairs and therefore would not be able to contribute to the relaxation of the TLS.

Material	$Q^{-1} (T < T^*)$	$Q^{-1} (T > T^*)$	$\frac{F_0}{F} (T < T^*)$	$\frac{F_0}{F} (T > T^*)$
Amorphous Solid	$\propto AT^3$	const.	$\propto \frac{3k}{2} \ln \frac{T}{T_0}$	$\propto \frac{-k}{2} \ln \frac{T}{T_0}$
Metallic Solid	$\propto BT$	const.	$\propto \frac{3k}{2} \ln \frac{T}{T_0}$	$\propto \frac{-k}{2} \ln \frac{T}{T_0}$
Single Crystal	$\propto Ce^{1/T}$	$\propto CT^{-2}$	const.	$\propto \frac{C}{T}$

Table 3.2: Table showing the temperature dependence of the dissipation, Q^{-1} and frequency shift, $\frac{F_0}{F}$, due to TLS of nanomechanical resonators for a range of materials. A, B, C and k refer to constants that depend on the material properties.

3.4 Conclusion

This Chapter looked at damping within nanomechanical resonators. At low temperatures dissipation due to two level systems is likely to dominate and the strength of this dissipation was strongly dependent on the material the resonator is made of, with a range of temperature dependences predicted (Table 3.2). We looked at a number of other works on dissipation and found however that these dependences while qualitatively supported were not quantitatively proven. We also showed that it appears that the superconductivity of a sample also affects the temperature dependence of the Q factor. Chapter 5 looks at how we can use this knowledge of dissipation to design and fabricate nanomechanical resonators with high Q factors. The next chapter looks at how we are able to measure the motion of a resonator with quantum limited precision.

Microwave Coupling and Quantum Limited Measurements

The idea behind this thesis is to create a situation where we are able to measure a nanomechanical resonator with quantum limited accuracy. Because of the cooling limits imposed on us by our experimental apparatus we need to find a way of further cooling a particular mode of a resonator. The method we use to do this is to couple the resonator to a microwave circuit and perform sideband cooling to effectively reduce the temperature of the resonator. This chapter deals with the theory behind microwave coupling and making quantum limited measurements as well as looking at work by other groups.

4.1 Quantum Limited Measurements

One of the main reasons that groups are still working with nanomechanical resonators despite the fact that Q factor scales inversely with size is that they have relatively large zero point motions, $\kappa_0 = \sqrt{\hbar/(2M_{eff}f_0)}$. The zero point motion of a resonator is the amplitude of the resonators motion when it is in quantum ground state. With nanomechanical resonators having zero points motions in the order of 10's of fm it is possible to accurately measure its zero point motion. However measuring such small deflections is not at all simple. This is because there are a number of different sources of noise that can effect the sensitivity of any measurement made.

One of these noise sources comes from quantum mechanics and the fact that the very act of measuring a system will effect its motion. Whatever measurement system is used to measure the motion of a resonator will apply a force on the resonator, this force is known as a back-action force. As this force causes the resonator to move it effectively adds noise to the measurement signal. The size of this noise, \bar{s}_f , depends on the precise type of measurement system for example in magnetomotive measurements it arises from the back emf generated by the resonators motion.

Even when we are not measuring the resonator it is still experiencing a number of forces for example as the interaction of gas atoms with the

resonator will cause it to move while interactions within the resonator can cause charge fluctuations altering an electrical signal. These forces add a noise, \bar{s}_{th} , can be defined by the force noise power spectral density (PSD). The PSD is related to the properties of the resonator and the temperature of the system such that,

$$\bar{s}_{th}(\omega) = 4k_B T m \omega / Q, \quad (4.1.1)$$

where m is the mass of the resonator [37]. However at low temperatures when $k_B T \approx \hbar \omega$ this value is no longer accurate and needs to be replaced with a semi-classical approach such that [38],

$$\bar{s}_{th} = \frac{2m\omega}{Q} \hbar \omega \coth \left(\frac{\hbar \omega}{2k_B T} \right). \quad (4.1.2)$$

This noise combined with the force noise, \bar{s}_f and any other electrical measurement noise, \bar{s}_m (e.g. from amplifiers) sets the limit on the precision of measurement we are able to make. As long as this total is less than the zero point motion we will be able to measure the resonator with quantum limited precision.

4.2 Microwave Coupling

In order to reach the situation where we can make quantum limited measurements we first need to cool a mode of the resonator so that Equation 1.1.1 is satisfied. To do this we need to couple the resonator to a microwave circuit and perform a cooling method known as sideband

cooling. This will allow us to cool a mode of a resonator so it has an effective temperature of zero. It will also allow us to alter the Q factor of the resonator

To start with it would be useful to discuss some of the important values and terms used in microwave coupling. We have already introduced the concept of the resonator's Q factor and zero point motion, κ_0 . As we want to be able to reach the resonator's ground state the next important values to be considered are the average thermal occupation, \bar{n} , and occupation probability, p_n . These give the average number of particles across all the energy levels and the probability of finding the resonator in a particular energy level respectively and are defined as [39],

$$\bar{n} = (k_B T_r / \hbar \omega) - 1/2, \quad (4.2.1)$$

and,

$$p_n = \left[\exp \left(-\frac{\hbar \omega}{2k_B T_r} \right) \right]^n \left[1 - \exp \left(-\frac{\hbar \omega}{2k_B T} \right) \right]. \quad (4.2.2)$$

where k_B is Boltzmann's constant, T_r is the resonator's temperature and ω is its resonant frequency.

As can be seen both the thermal occupation and the occupation probability are strongly dependent on the temperature of the system. Even when we set the temperature, $T_r = \frac{3\hbar\omega}{2k_B}$ so that the thermal occupation $\bar{n} = 1$ the probability of finding the resonator in its ground state is still only 20%. This shows that at any non-zero temperature there is a finite probability that the resonator will be in an excited state. As when we

talk about cooling the resonator to its ground state we require $\bar{n} < 1$ for the majority of the time we need to be able to cool the resonator until one of its modes effective temperature is zero.

As we are coupling the resonator to a microwave circuit an important value is the coupling strength, g . This is useful when looking at microwave coupling as it describes how well the electrical and mechanical resonators are coupled. Its exact value depends on the particular type of system but it can be defined as how much the resonant frequency of the microwave circuit shifts per unit motion of the resonator, $g = \partial\omega/\partial u$. This coupling strength can be boosted from its base value of g by increasing the energy pumped into the circuit. This increases the number of phonons in the circuit and as phonons are the mediating particle between the mechanical element and microwave circuit increases the coupling. The limit of how many phonons that can be put into the circuit depends on the room temperature electronics and the fact that it needs to be ensured that any metallic layer remains superconducting with too many phonons causing the superconductivity to break down.

As well as the coupling strength g another important value is the cooperativity of the system as this defines the rate at which the circuit can take energy from the resonator this is defined as [40],

$$C = \frac{4g_0^2}{\Gamma_m \kappa_0} \quad (4.2.3)$$

where Γ_m is the mechanical damping rate. If this value is too small it

will not be possible to cool effectively as the thermal decoherence rate, $\Gamma_{th} \approx n\Gamma_m$ i.e. the rate at which the resonators motion will cause it to heat will be higher than the rate at which the circuit can remove the energy. What this shows is that we need to keep the mechanical damping rate as low as possible, or to put it another way to have as high a Q as possible.

In order to create a strong interaction between a mechanical mode and microwave circuit we need to ensure that our system is in the good cavity limit. Whilst there is no precise definition as to what this is in principle the system needs to be arranged such that,

$$\Gamma_m \ll \Gamma_c \ll g < \Omega_m \quad (4.2.4)$$

where, Γ_c is the electrical damping. What this expression represents is the fact that the mechanical damping must be less than the electrical damping which must be less than the coupling rate thus allowing it to remove energy at a quick enough rate. The coupling rate must also be less than the mechanical frequency to allow for the coherent transfer of quanta between states within the resonator's ringdown time.

If a resonator is in the good cavity limit then it is possible to use the microwave circuit to alter the behaviour of the resonator. This is done by using the microwave circuit to pump the resonator. The microwave circuit has a frequency, ω_c , it then has sidebands a distance equal to the mechanical frequency, ω_m , either side of ω_c . These sidebands are known

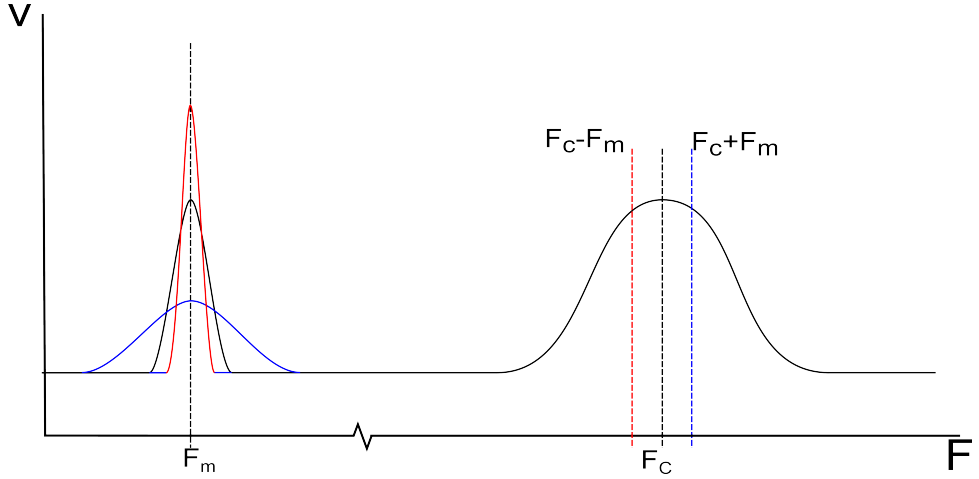


Figure 4.1: Figure showing the effect of driving the electrical circuit on one of its sidebands. As can be seen the mechanical resonance is altered from its normal state (black lines) by either driving it blue detuned (blue line) or red detuned (red line).

as resolved sidebands if, $\Gamma_m \ll \Gamma_c$. By applying a pump tone at $\omega_c \pm \omega_m$, then so called sideband effects can be observed. In the situation where the drive frequency is on the lower sideband it is known as red detuned then energy is removed from the resonator thus reducing its Q however more importantly also reducing its effective temperature. The strength of this cooling rate can be defined by its cooperativity, C , as shown in Equation 4.2.3. In the opposite case i.e. if the frequency is on the upper sideband it is known as blue detuned and energy is added to the resonator resulting in an effective negative damping source therefore increasing its Q and temperature [40]. These effects are represented in Figure 4.1.

It is possible to use sideband cooling to cool a particular mode of the resonator until its effective temperature is equal to zero. A number of

groups have looked at doing this as well as the opposite case and a brief description of some of this work follows.

4.3 Other Work on Microwave Coupling

One of the main groups that has looked at this area is Teufel et al. [41]. The key innovation of their work was to create a lumped element circuit. By doing this they were able to use a parallel plate capacitor which greatly increased their coupling strength. Their work involved using an aluminium membrane to form one part of parallel plate capacitor. This capacitor was then combined with an on chip inductor to form part of an LCR circuit. The membrane had a zero point motion of 4.1 fm and resonant frequency of 10.69 MHz. They were able to get to the point where $\bar{n} < 1$, such that the phonon occupation was just 0.34 however they were not able to perform quantum limited measurements. Their mechanical membrane was just a simple polycrystalline aluminium membrane with a Q factor of 300000 at 15 mK. As we have the ability to create membranes out of high stress silicon nitride we should be able to obtain a better Q factor. It is also possible that by using a single crystal aluminium device we could also improve the Q factor. To improve the quality of the measurements they were able to make they exploited an impressive electrical system that included a custom-made Josephson parametric amplifier [42], which can amplify

the microwave signal while adding minimal noise. It is likely that if we wanted to approach the quantum limit we would have to include a quantum limited amplifier and a low temperature, high electron mobility transistor (HEMT) amplifier to the set up discussed in Chapter 6.

Work has also been done by Faust et al. [43], who have managed to couple a resonator with a microwave cavity but interestingly they did this at room temperature. Whereas other work has looked at using the resonator to form one plate of a capacitor they placed a high stress silicon nitride beam within a parallel plate capacitor (Figure 4.2). This meant that in moving the resonator the average permittivity of the gap between the plates varied. The motion of the resonator was measured by recording the electrical noise on the sidebands of the microwave circuit. As this noise will increase when the beam is resonating it is an effective way of measuring the mechanical response. Due to their high starting temperature they were not able to get anywhere near the quantum limit, they were however able to effectively cool the resonator from 300 K to 150 K. They successfully showed that when the drive signal was detuned by ω_m they were able to either increase or decrease the amplitude of the resonator. When the frequency was reduced the cavity created an electrical force (back-action force) which opposed the motion of the resonator thus decreasing its amplitude, and conversely when the drive frequency was increased, the amplitude was also increased as the back-

action force opposes the mechanical damping of the resonator. As the back-action is effectively a form of damping, the Q of the resonator is also affected by the detuning with it decreasing with negative detuning and increasing with positive detuning. When they were driving the circuit with positive detuning and a large power they are effectively adding a negative damping to the motion of the resonator. This meant that they were able to increase the Q factor by a factor of 5 to 1.3 million which is astonishingly high for these conditions. Whilst it is useful to know that it is possible to couple a mechanical and electrical circuit at room temperatures, their work also has great promise for improvement as they were only working in the weak coupling regime with a coupling factor, g_c , nearly a million times smaller than Teufel et al. [41]. This shows that while the ultimate aim is to reach the quantum limit the blue detuned regime in which the Q is increased is also interesting and worth investigating further. If the coupling factor for this work could be improved or even if the environment temperature was reduced the achievable Q by would be greatly improved. This could result in highly precise sensors of mass, force or temperature.

A method to couple a torsional resonator in a cavity has been demonstrated by Kim et al. [44]. They optically coupled a torsional resonator with a whispering gallery mode resonator. They did this by fabricating a two paddle torsional resonator next to a microdisk whispering mode resonator (Figure 4.3). The silicon resonator changed the index of re-

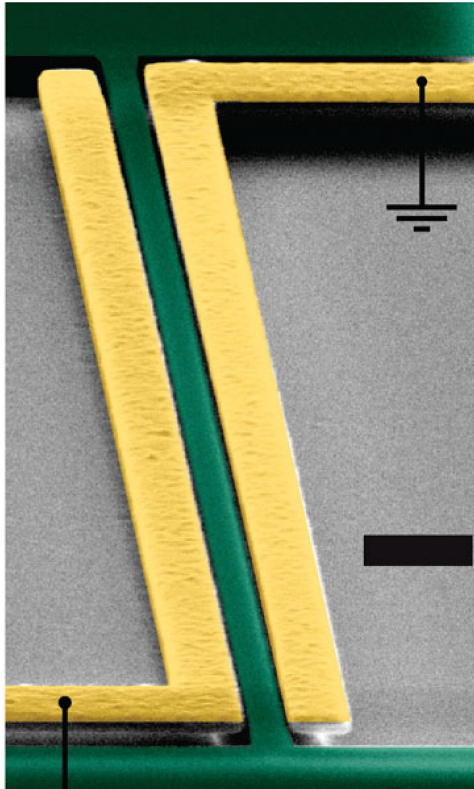


Figure 4.2: Resonator used in experiments by Faust et. al. The green areas represent the silicon nitride beam that alters the permittivity of the gap between the gold capacitor plates. Reproduced from [43]

fraction of the optical cavity, meaning that as the resonator moved the optical resonance of the microdisk was also altered. However as they were using a piezo to drive the resonator, they had better coupling for the flexural mode compared to the torsional mode. It could be possible to use our method of driving the torsional mode with a piezo to improve the coupling of the torsional mode and therefore take advantage of its apparent greater Q factor.

In addition to driving the system either red or blue detuned, it could also be interesting to simultaneously drive on both sides of the resonant

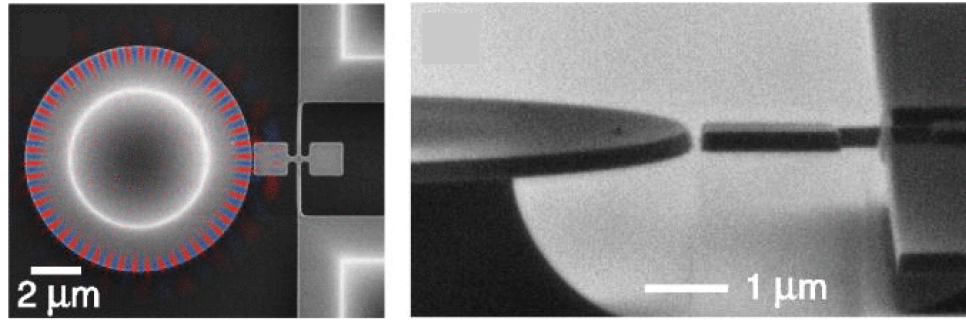


Figure 4.3: Image of the resonator used by Kin et al. where a torsional resonator was coupled with a whispering gallery mode resonator. Reproduced from [44].

frequency (known as sideband squeezing or two sideband pumping). It has been theoretically shown [45–47] that by doing this it could be possible to measure the position of the resonator without the effects of the back-action force generated by the coupling, this effectively overcomes the Heisenberg limit. This is done by only measuring one quadrature of the resonator’s movement, with the back-action force only affecting the other quadrature. The ability to squeeze the state so that it is possible to measure below the quantum limit was demonstrated by Wollman et al [48]. They coupled an aluminium micron scale mechanical resonator into a LCR circuit and drove on both sidebands. In doing this they were able to reduce the motion of the resonator on one quadrature to $0.8 \kappa_0$, whilst on the other quadrature the motion was around $10 \kappa_0$.

4.4 Conclusion

This chapter looked at the theory behind making quantum limited measurements of a resonators motion and set out the requirements to be able to do this. It then moved on to the theory of microwave coupling and sideband cooling that will allow us to cool a resonator down to a temperature where this was possible. Finally it looked at a number of pieces of work that have looked and making quantum limited measurements and performing microwave coupling. In Chapter 8 we set out how we designed a system that would be capable of performing quantum limited measurements of a nanomechanical resonator. The next chapter looks at various fabrication methods we used to be able to maker such a mechanical resonator.

Fabrication of Nanomechanical Devices

As can be seen in Chapter 3 the Q factor of a resonator is strongly dependent on its physical and material properties. This means that focus needs to be paid to: a) its surface as this will cause damping via TLS b) to the structural quality of the resonator as this will effect its resonant frequency and c) the points at where it is clamped (as energy can be lost through these clamping points). To create devices that have high Q factors we have used a number of novel fabrication techniques to make devices ranging from free standing beams, to membranes and micron scale torsional resonators. This chapter starts by looking at some of the equipment and more novel methods we have used and have developed for this work. It then goes on to describe the fabrication procedure for creating silicon nitride torsional resonators, single crystal aluminium beam resonators and on chip LCR circuits which incorporate

a silicon nitride membrane into a parallel plate resonator. We have also worked with the school of Electronic Engineering at the University of Nottingham to make high quality nanometre scale bow tie antennas (BNA's) for optical trapping of nanoparticles and a description of the method behind the BNA's fabrication is also included. Full fabrication methods for the devices discussed can be found in the appendix.

5.1 Wafers

The starting point for all the devices in this thesis is a planar substrate, there are a number of forms a substrate can take but mostly they take the form of a single crystal. Examples of common single crystal substrates are silicon, sapphire (Al_2O_3) and gallium arsenide (GaAs). It is useful for the wafer to be semi-insulating as this prevents the build up of static charge during fabrication which could either damage the NEMS or cause problems with fabrication techniques such as electron beam lithography. Being semi-insulating means that once they have been cooled down to low temperatures they are fully insulating and will therefore not interfere with the measurements.

For the experiments on torsional resonators and LCR circuits a silicon substrate¹ was used. This enabled the deposition of a sacrificial layer of silicon dioxide and a high stress layer of silicon nitride. The silicon

¹Wafer supplied by Wafer World, Palm Beach, Florida, USA

dioxide and nitride layers were deposited via chemical vapour deposition by Cornell nanofabrication facility. The silicon nitride was deposited so that it had an inbuilt stress of 1050 GPa, meaning that we were able to make resonators with an increased stress resulting in an increase of the Q factor.

For the experiments on single crystal aluminium beams, a GaAs substrate was used. This allowed a 30 nm single crystal layer of aluminium to be grown at sub room temperatures via molecular beam epitaxy (MBE), this was done here in Nottingham by Dr Elisa Antolin. The aluminium was then capped with a 14 nm layer of amorphous GaAs to ensure that the aluminium did not oxidise prior to fabrication.

5.2 Metallization

There are a number of different ways to coat a sample with thin films, the choice of what to use depends on the particular application. The simplest way of coating a sample with a thin metallic film is via thermal evaporation. Thermal evaporation works by placing a metal in a crucible through which a current is passed. Joule heating in the crucible causes the metal to heat up. By placing the crucible and the sample in a bell jar which is evacuated to pressures in the 10^{-7} mbar range the metal evaporates and is driven towards the sample where it cools and forms a thin film. The advantages of this method is that that it

is quick and relatively inexpensive, however the disadvantages are that you are limited to what metals can be deposited as they have to have melting points below that of the crucible and would also need to be able to reach a temperature where the vapour pressures allowed it to be evaporated.

To increase the range of metals that can be deposited electron beam evaporation (EBE) can be used. In EBE a high energy (10 kV) beam of electrons is directed towards a evaporant which is placed in an crucible with a high melting point such as ceramic, or carbon. As with thermal evaporation this causes the metal to evaporate onto the sample. As well as having a wider range of metals that can be evaporated via this method, it also produces higher quality films. This is because firstly, thanks to the use of a load-lock to transfer samples, we are able to evaporate at a much lower pressure and in a much cleaner chamber. Secondly, we are able to evaporate at a slower rate resulting in a higher quality film. We are also able to rotate the sample in this chamber resulting in a more uniform film across the wafer.

In addition to thermal and electron beam evaporation there are a number of other methods such as sputtering and chemical vapour deposition that can be used to deposit thin films, however they have not been used in this work.

5.3 Etching

In order to fabricate the free standing structures discussed in this thesis we need to etch away parts of the wafer. There are two ways to etch a wafer, either via a wet etch where acids are used to remove unwanted material, or via a dry etch where reactive gasses are used. These methods have both advantages and disadvantages. Broadly speaking wet etches have better selectivity between materials e.g. between the target material and photoresist, meaning they are better to use if a lot of material needs to be removed. In addition to having better selectivity, using acids also allows isotropic etching or anisotropic etching that can be along a particular crystal axis. This means it is particularly useful for undercutting structures or creating membranes such as those used to create torsional resonators. The trouble however with wet etches is the range of materials that can be etched as well as the etch uniformity. This is why for a number of etches we use dry etching. To perform dry etching we use a plasma etcher². Dry etching works by applying a large RF voltage between two plates. The sample is placed on the bottom plate. In between the two plates a low pressure gas is pumped, the RF field then causes this gas to turn into a plasma. This plasma contains electrons and ions. As the bottom plate has a RF field applied to it it rapidly switches between being negatively charged and positively charged. Due to the fact that the electrons are a lot lighter

²Corial 200IL ICP Dry Etcher

then the ions they are accelerated towards the bottom plate a lot faster than the electrons. Over time the electrons hitting the sample cause it to be negatively charged. This causes the positive ions to be accelerated towards the sample. The sample is either chemically etched, where the plasma chemically reacts with the target material causing it to be removed or alternatively the wafer can be physically etched, where the wafer is bombarded with gas ions causing ablation of the wafer. The etch rate of the dry etch can be controlled by either altering the gas chemistry or the applied RF power. Etching can be monitored via a laser interferometer focussed on the sample which gives an indication of the etch rate, it is especially useful for detecting when a certain layer has been removed as the etch rate changes. The problem with this method is that the selectivity with photoresist is often very poor often as bad as 1:1 for PMMA. This means additional masks often have to be used such as lift-off resist (LOR 5A) or metallic masks (commonly germanium due to its resistance to oxygen etching).

5.4 Lithography

The majority of fabrication methods require you to be able to define a pattern on the wafer, this pattern is then used as a mask in later fabrication steps. Lithography is used to define this pattern. Lithography works by first applying a thin polymer (known as a resist) to the surface

of the sample. The resist, dissolved in solvents is normally applied via spin coating, in which the resist is deposited onto the sample before spinning it at a few thousand rpm for 30-45 s. The sample is then placed on a hot plate or a oven to remove the solvent, this is known as soft baking. The polymer in the resist is sensitive to incident radiation which can come from, photons, in the case of photolithography, or electrons in the case of electron beam lithography (EBL). One of two things happens to the resist when it is exposed to this radiation; in the case of positive resists such as PMMA the polymer chains are broken up. This results in them being more soluble in a developer, this means that it is possible to only remove the resist where it has been exposed. In the case of negative resist such as AR-N the opposite situation occurs and the radiation initiates a chemical reaction in which the polymer chains are cross-linked making them less soluble. This results in the area that has been exposed remaining after the sample has been developed.

As mentioned earlier there are two ways to define a structure, either via photolithography or EBL. In photolithography light is shone through a mask, which is transparent plate that has had chrome deposited on it in certain areas to block the light. The wavelength of the light used sets a limit for the resolution of this method. Whilst companies like Intel have managed to get below 14 nm using excimer lasers and phase shift masks, our contact mask aligner³ has a resolution limit of around 1-2

³Suss Microtech MJB-3

microns. The fact that the exposure time is only a few seconds for a whole sample means this method is well suited to exposing large areas such as contact pads and ground planes.

To create structures that have nm scale dimensions we need to use electron beam lithography (EBL). In EBL a beam of high energy electrons are focussed and directed onto the sample, a computer is then used to define the region of the sample exposed to the electron beam. A series of deflection coils and a nanopositioning stage are used to define the pattern on the wafer. The setup in Nottingham uses a modified Jeol 7000-F thermal field emission scanning electron microscope (SEM), to which a beam blanker has been added to allow the beam of electrons to be blocked while the sample and/or beam is moved around. A pattern generator⁴ controls the deflection coils and the nanopositioning stage. Whilst this method is very useful for drawing small patterns it is slow, with it taking over one hour to draw a 1 mm by 1 mm square, this means it is often combined with photolithography. To do this location marks defined by earlier photolithography or electron beam lithography steps are used, these can be scanned with the SEM, its dimensions are then compared to a mark recognition file. The EBL software can then alter the scale and position of the pattern it draws. Using this method allows for patterns to be positioned with sub-micron accuracy.

The resolution that can be obtained with this method is a bit more com-

⁴XPG-2 from XENOS semiconductors.

plicated to work out than it is for photolithography as it is not limited by the wavelength of the electrons (which would be in the sub nm scale) rather it is limited by how these electrons scatter when they hit the substrate. There are 3 different types of interactions that occur when the electrons travel through the sample [49] these are shown in Figure 5.1 . The main interaction is due to the creation of secondary electrons created when the incident beam travels through the resist and some way into the substrate and slows down. As these secondary electrons have low energies they only travel a small distance therefore do not significantly contribute to the overexposure of the resist. In addition to the creation of secondary electrons there are two types of scattering that need to be considered. The first type of scattering is forward scattering, in forward scattering the electrons are deflected by a small angle. The total amount of scattering builds as the beam travels through the resist and into the substrate, this means that it is preferable to use a thin resist. The second type of scattering is backscattering and occurs when the scattering angle is large. As the scattering angle is large it allows for the electrons to travel large distances away from the incident beam as they are not limited by the thickness of the resist. As we are working with high accelerating voltages (30 kV) considerable backscattering also occurs in the substrate. The amount of backscattering that occurs in the substrate depends on the substrate material [50]. This means that the amount of overexposure varies between different substrates. The

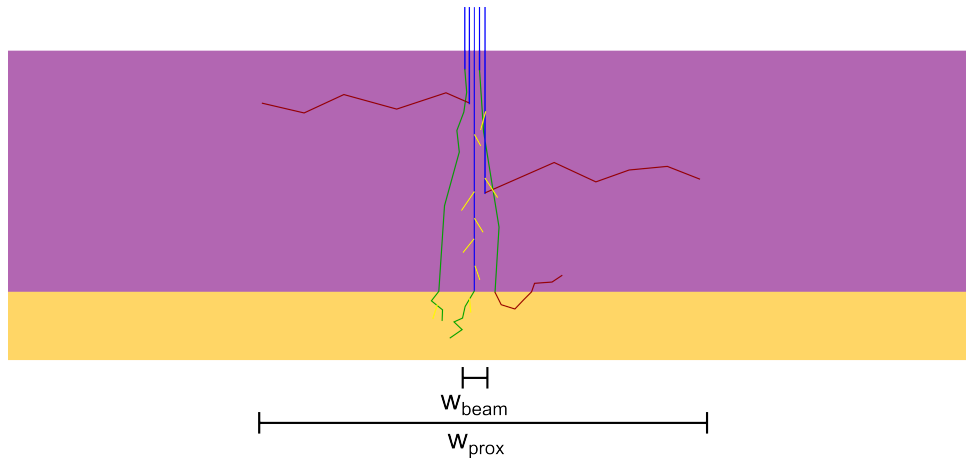


Figure 5.1: Figure showing effect of scattering on the exposure width of a electron beam. The incident beams (blue lines) width w_{beam} is increased to w_{prox} . As the beam travels through the resist (purple) and into the substrate (yellow) it is expanded due to secondary electrons (yellow lines), forward scattering (green lines) and back scattering (red lines)

combination of these scattering mechanisms results in an area around the drawn pattern also being exposed. This increase in exposure area is known as the proximity effect, and restricts the practical resolution of EBL to around 10 nm depending on the quality of the beam focusing. There are a number of ways that the proximity effect can be overcome or even exploited to improve the resolution of a pattern.

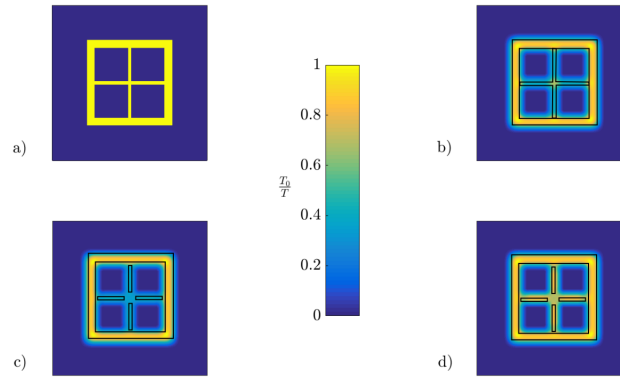


Figure 5.2: Figures showing computer simulations of the additional dose received due to the proximity effect as a ratio of the additional dose. a) shows the drawn pattern, b) shows the dose without any correction, c) shows the dose after shape correction and d) shows the dose after both shape and dose correction. Black outline shows the pattern drawn by the software.

5.4.1 Proximity Effect Correction

As mentioned in the previous section the proximity effect causes over-exposure in the drawn pattern, for many designs this can have a drastic effect on the way the sample behaves. To better understand what the proximity effect causes a Matlab program⁵ can be used to show how the dose varies over a given pattern. Figure 5.2 gives an example created by us of this program along with 2 different solutions to correcting for the proximity effect.

Figure 5.2a shows the pattern that is desired, while 5.2b shows the dose without any correction i.e. if the pattern was drawn with a constant

⁵Written by Dr. Mellor

dose. This shows that the dose due to backscattering varies significantly over the pattern. Most notable is that the central cross has a lower dose, this is due to the fact that the lines are smaller meaning that there is less exposure due to the proximity effect. What is also notable is that on the junction of two lines there is not a right angle connection instead there is a curved corner. This is also due to there being more electrons hitting this region causing an increase in the number undergoing backscattering. Figure 5.2c shows one solution to this problem known as shape correction. In this method the drawn shape is altered by removing the centre and edges of the cross from the exposure. As can be seen these areas are still exposed, this is again thanks to the proximity effect. This improves the area around the corners and the center of the cross. However with this method the smaller beams are still underexposed, to fix this problem it is possible to vary the dose for different parts of the pattern. Figure 5.2d shows a combination of shape and dose correction, in this method the smaller lines are given a larger dose while the areas around the center of the cross and the junctions are given smaller doses. As can be seen this comes very close to recreating the desired pattern with just a few small variations. This can be improved even further by more precise control of the drawn shape and dose. There are a number of commercial programs that will do this automatically, however these are expensive and are currently not available in our facilities.

It was thanks to the shape proximity effect correction that we were able to create a range of high quality devices including some for other groups. Figure 5.3 shows an resonator fabricated for Birmingham University from niobium that had been deposited onto a silicon wafer. It included a 100 nm wide and 15 μm long beam. A combination of dose and shape proximity effect corrections were used to ensure all the corners were near perfect right angles. Further to this in a collaboration with the Electronic Engineering Department at the University of Nottingham we were asked to use our fabrication skills to create an array of gold BNA's on a glass substrate. It was required that these BNA's had as sharp as possible points as well as as small as possible separation. The fabrication method for these BNA's is described below.

5.5 Fabrication of Gold Bow Tie

Nano Antennas

Bowtie nano antennas (BNA's) were first used to demonstrate optical trapping by Roxworthy et al. in 2011 [51]. They are able to trap sub-micrometer to micrometer sized particles with forces 20 times larger than the previously used optical tweezers. The work here at Nottingham is focussed on trapping biological samples. By doing this they hope to better understand structures such as cells, bacteria, enzymes, proteins and DNA. Computer simulations of the devices suggests that they will

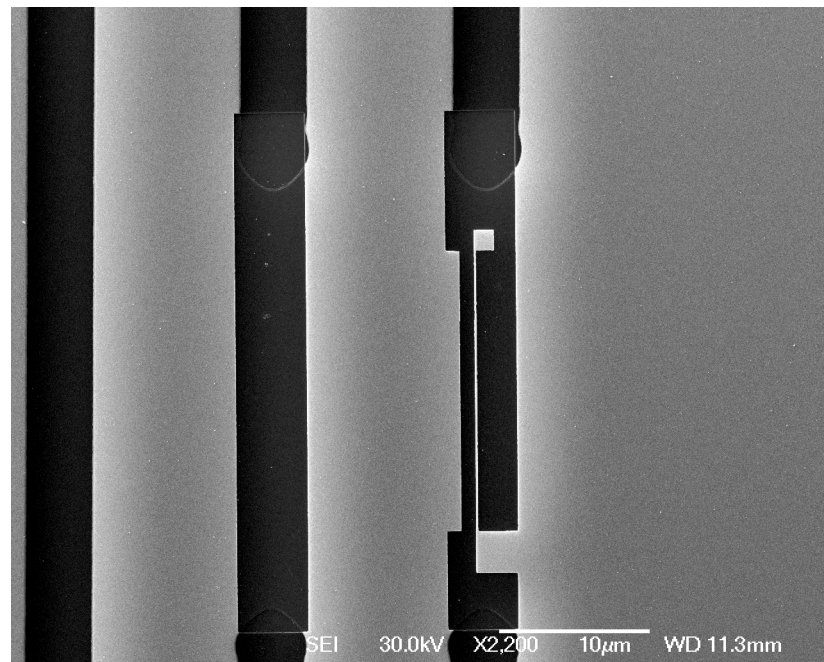


Figure 5.3: SEM image showing a capacitor created for Birmingham university. The resonator incorporates a 100 nm beam into an inductor and features near right angles corners that was made using a combination of shape and dose correction.

be able to use these devices to perform high quality optical trapping experiments [52].

The BNA's and crosses were fabricated on a 0.17 mm thick 1 inch by 1 inch glass cover slip. The cover slip is cleaned in ethyl lactate, acetone, methanol and IPA in an ultrasonic bath, before being dehydrated on a hot plate. A 170 nm layer of PMMA 495k A5 was spin coated before being soft baked. In order to be able to perform electron beam lithography we need a conducting substrate, this stops the charge building up on the surface. This charge build up causes over exposure and causes the beam to be deflected resulting in the drawn pattern differing from the desired pattern. In order to make the cover slip conductive we use a specialist coating⁶ which forms a conductive film on the surface of the cover slip, while not interfering with the exposure. A 50 nm layer of this coating is spin coated before being soft baked.

To define the BNA's we used electron beam lithography. The proximity effect will cause the points of the triangle to be over exposed, resulting in a rounded point. A number of different tests were performed to see how the sharp point can be maintained. Initially the point was just removed however this resulted in a flat tip. Next a number of simulations were performed using the Matlab program mentioned earlier. This appeared to show that by indenting the point and adjusting the dose in this area we should be able to create sharp points. However whilst this

⁶SX AR-PC 5000/90.2, supplied by ALLRESIST GmbH, Stausberg, Germany

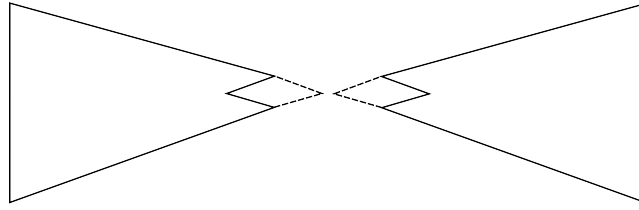


Figure 5.4: Figure showing the shape drawn to make a BNA. The solid line was drawn and the proximity effect ensured that the actual shape produced included the dashed line.

worked well on semi-insulating silicon wafers it was found that it did not work on the glass slides. This was because of the fact that the glass slides were insulating, this meant that the stitching of the pattern was not perfect (i.e. the areas with different doses did not match up). With this in mind it was decided that the best solution was to use purely shape correction (with the indented point). The proximity effect ensured that the indented portions of the point were exposed without the overexposure of the point (Figure 5.4). Measurements in a SEM showed that the radius of the point was less than 10 nm.

Once exposed the sample was placed in de-ionised water to remove the conductive film, before being developed. The sample was then placed in a thermal evaporator which was pumped to pressures in the 10^{-7} mbar range, before a 1-3 nm titanium adhesion layer followed by 50 nm of gold was evaporated onto the sample. The sample was then placed in acetone to remove the resist and lift off the excess gold. An SEM image of a BNA can be seen in Figure 5.5.

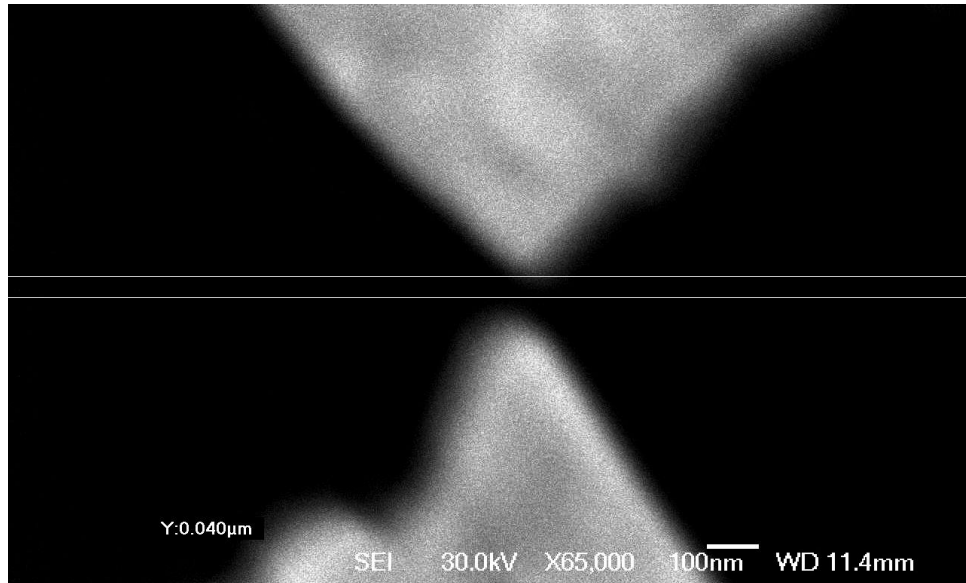


Figure 5.5: SEM image of a gold on glass BNA showing a gap less than 40 nm. The poor quality of the image is due to charge build up the insulating glass substrate.

5.6 Fabrication of Silicon Nitride Torsional Resonators

The silicon nitride torsional resonator was made using a wafer that consists of a silicon substrate onto which 575 nm of silicon dioxide and 170 nm of high stress silicon nitride had been deposited. The silicon dioxide acts as a sacrificial layer allowing the resonator to be released. The wafer was cut into 9.5 mm by 9.5 mm squares and cleaned. A 170 nm layer of PMMA A5 was then spun onto the wafer and soft baked. Next a pattern of alignment marks and location marks are exposed using EBL, the location marks are those described in Chapter 6 and facilitate the location of the resonators once it was placed in the measurement

apparatus. The sample was developed before being placed in a RIE where a short silicon nitride etch was performed, this roughens the surface of the wafer allowing for better adhesion of the metallic layer. The sample was then placed in a thermal evaporator where 5 nm of chrome and 50 nm of gold are deposited, the chrome acts as a adhesion layer and is chosen over the more commonly used titanium as it is not etched in the hydrofluoric acid used in a later step.

The next step is to make a silicon nitride membrane, these membranes can also be used to create vacuum gap capacitors that could be used for lumped element microwave circuit NEMS experiments. To make the membrane a 500 nm layer of PMMA A8 was spin coated before being baked in an convection oven. A series of dots, one micron in diameter, were then defined using EBL (Figure 5.6a). The sample was then developed before being placed in a dry etcher where a long silicon nitride etch is performed to leave the sample with a number of holes that extend into the silicon dioxide layer. The silicon dioxide is then removed via a 48% hydrofluoric wet etch. Before etching the sample is transferred between beakers of acetone, methanol, IPA and water without drying, this ensure that the HF can easily access the holes. The sample is then placed in the HF which has a selectivity of over 1000:1 for silicon dioxide compared to silicon nitride [53]. To remove the acid from the gap underneath the membrane the sample is transferred between beakers of water, then IPA, then methanol before being blow dried. An

alternative to blow drying especially for the larger membranes used in the LCR circuits is to use a critical point dryer, which replaces the IPA with liquid carbon dioxide, which is in turn converted to gaseous carbon dioxide without crossing the liquid gas phase boundary (Figure 5.6b).

Once the membrane has been made 170 nm of PMMA 495k A5 was spin coated before being soft baked. As the resist acts as an etch mask the inverse of the pattern was then exposed using EBL, with a varying dose to ensure a good definition at the cut outs between the beam and paddle . The resist pattern was then developed before being placing the sample in a RIE (Figure 5.6c). A silicon nitride etch is then carried out to release the resonator, it is then checked in an SEM (Figure 5.6d).

An additional step can be incorporated after the membrane has been made to deposit a metallic dot to allow for torque magnetometry experiments to be carried out. This is done by spin coating PMMA 495K A5 and defining a dot in an appropriate place on the resonator before developing and then placing the sample in a thermal evaporator, e-beam evaporator or sputter deposition device. The waste material can then be lifted off in acetone before continuing as normal. An SEM image of a torsional resonator with a metallic dot fabricated with this method can be seen in Figure 5.7.

Full details of the process for these devices can be found in the Appendix.

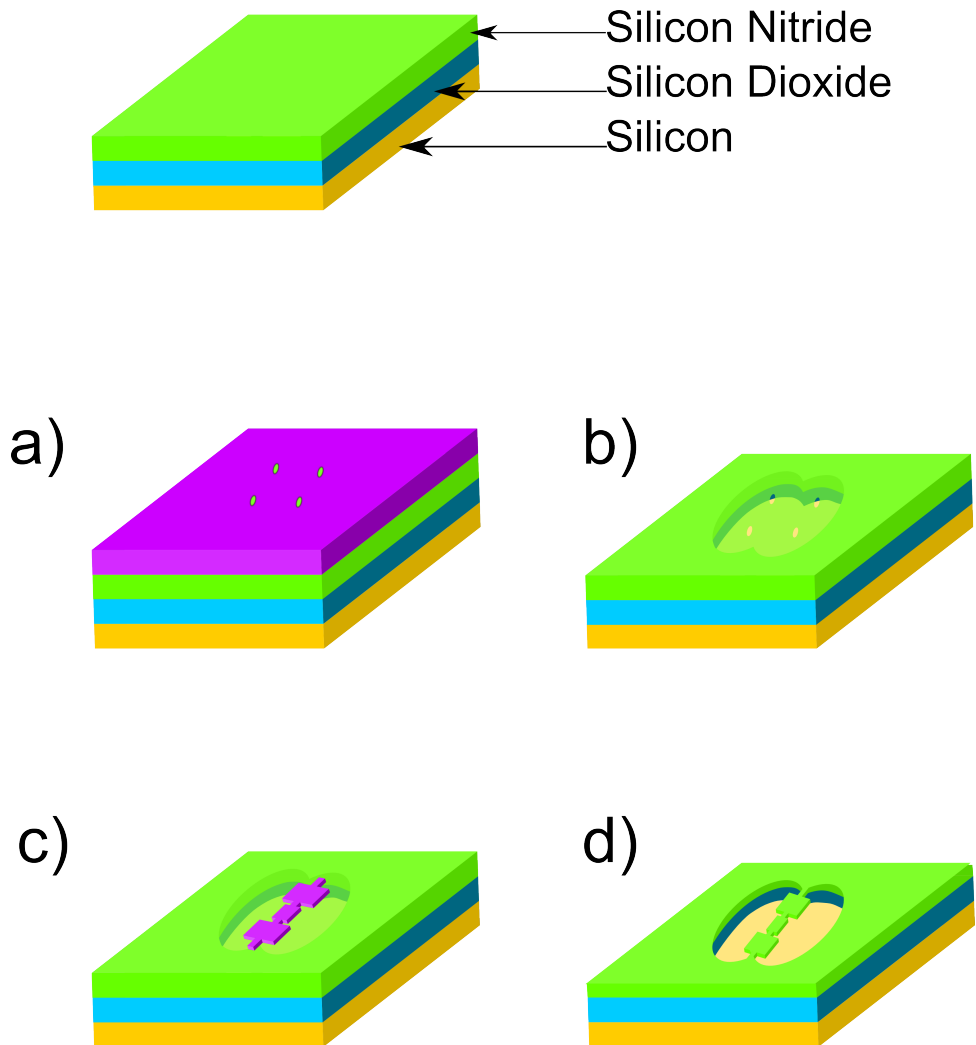


Figure 5.6: Diagram showing the fabrication procedure for making of silicon nitride torsional resonators. a) Etch holes are defined in a layer of PMMA and the silicon nitride via EBL then a CHF_3 dry etch, b) a membrane is created via a removal of the silicon dioxide by a HF wet etch, c) the resonator is defined in PMMA via EBL, d) the resonator is released by removing the silicon nitride with a CHF_3 dry etch.

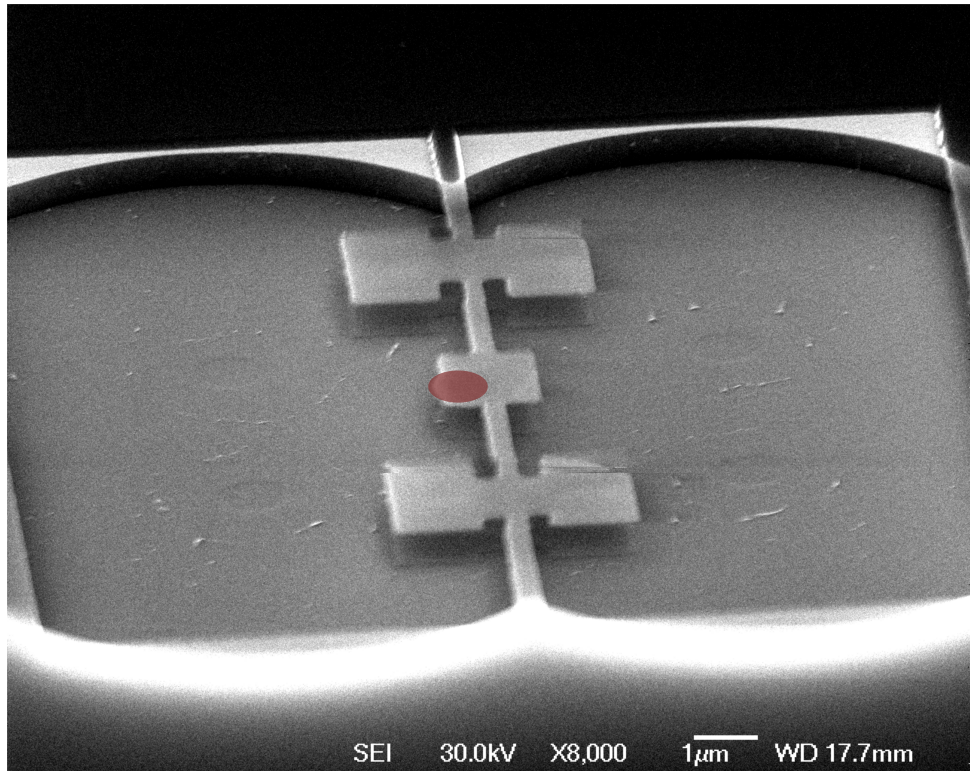


Figure 5.7: SEM image of a silicon nitride torsional resonator onto which a nickel dot has been deposited (highlighted in red). Image is taken at a 45° tilt.

5.7 Fabrication of Single Crystal Aluminium Beams

The single crystal aluminium beams are fabricated from a GaAs wafer onto which 30 nm of single crystal aluminium has been grown by MBE followed by a 14 nm layer of amorphous GaAs. The wafer was first scribed into 4.9 by 4.9 mm chips. The sample was then cleaned, before being dehydrated on a hot plate. A 170 nm layer of PMMA A5 was then spun onto the wafer and soft baked. Next a pattern of alignment marks and contact are exposed using EBL. The sample is then developed before being placed inside an thermal evaporator where 50 nm of polycrystalline aluminium was deposited. This layer of aluminium ensures that there is good contact between the contact pads and the bond wires. The excess aluminium was lifted off by placing the sample in Dimethyl sulfoxide (DMSO) at 70°C. The negative electron beam sensitive resist we use is AR-N 3500, as this is a very thin resist, and due to the fact that the etch used to remove the aluminium and aluminium oxide are very aggressive etches, a mask of lift off resist (LOR) and germanium was also used. A 170 nm layer of LOR5A was spun onto the wafer and soft baked, before being placed inside a thermal evaporator where 80 nm of germanium was deposited. A 100 nm layer of AR-N 7520 was then spun on and then soft baked. The sample was exposed using EBL before being developed (Figure 5.8a). The wafer

was then placed on a graphite shuttle in a RIE where the germanium and LOR was removed to leave a mask of LOR and a thin layer of germanium, this mask stands up well to the chlorine etch used to remove to aluminium. To etch the aluminium the sample is transferred onto a chrome shuttle where the GaAs cap layer is removed, then a precautionary aluminium oxide etch is performed before finally the aluminium is etched, this final etch is carefully monitored by watching the signal from a laser focussed on the aluminium, once the aluminium has been removed the signal drops significantly due to the drop in reflectivity. As soon as this dropped is observed the etch is stopped as soon as the aluminium is removed (Figure 5.8b). This ensures that the aluminium resonator is as thick as possible. Once the aluminium has been etched the sample is rinsed in water before being cleaned in DMSO overnight to remove any residual resist. To release the beams a wet etch needs to be used as the standard dry etch for GaAs is an isotropic etch so would not undercut the beam sufficiently to release it. To ensure that there is minimal undercutting at the clamping points where the beam meets the contact pads etch windows were used to release the resonator. This ensured that the resonator was clamped away from the contact pads. To define the etch windows a 170 nm layer of PMMA A5 was spun onto the wafer and soft baked. The etch windows were then exposed using EBL. The sample was then developed allowing the windows to be etched. A mixture of citric acid and hydrogen peroxide was used to

release the beam as this is highly selective for GaAs over aluminium. Once the etch was carried out the sample was transferred from water to IPA then to methanol before being blown dry with a nitrogen gun, this was to ensure that the surface tension did not break the beam as methanol has the lowest surface tension of commonly used solvents (Figure 5.8c). The beam was then inspected in a SEM to ensure it had been released, before checking its resistance. Finally the sample is attached to a 12 pin header with silver epoxy before being bonded with gold wires and silver epoxy. An SEM image of an aluminium beam can be seen in Figure 5.9.

Full details of the process for these devices can be found in the appendix.

5.8 Air Bridges

To make structures such as on chip inductors or capacitors we need to be able to create air bridges. An air bridge can be used to allow two wires to cross without them touching each other. It can also be used to suspend the top plate of a parallel plate capacitor over the bottom plate. To make these air bridges we use a resist called PMGI (Polymethylglutarimide)⁷, this resist has the property that it can be made to reflow via a softbake. A typical process would involve using a standard photolithographic process to define an area of a sample where

⁷supplied by Microchem. MA, USA

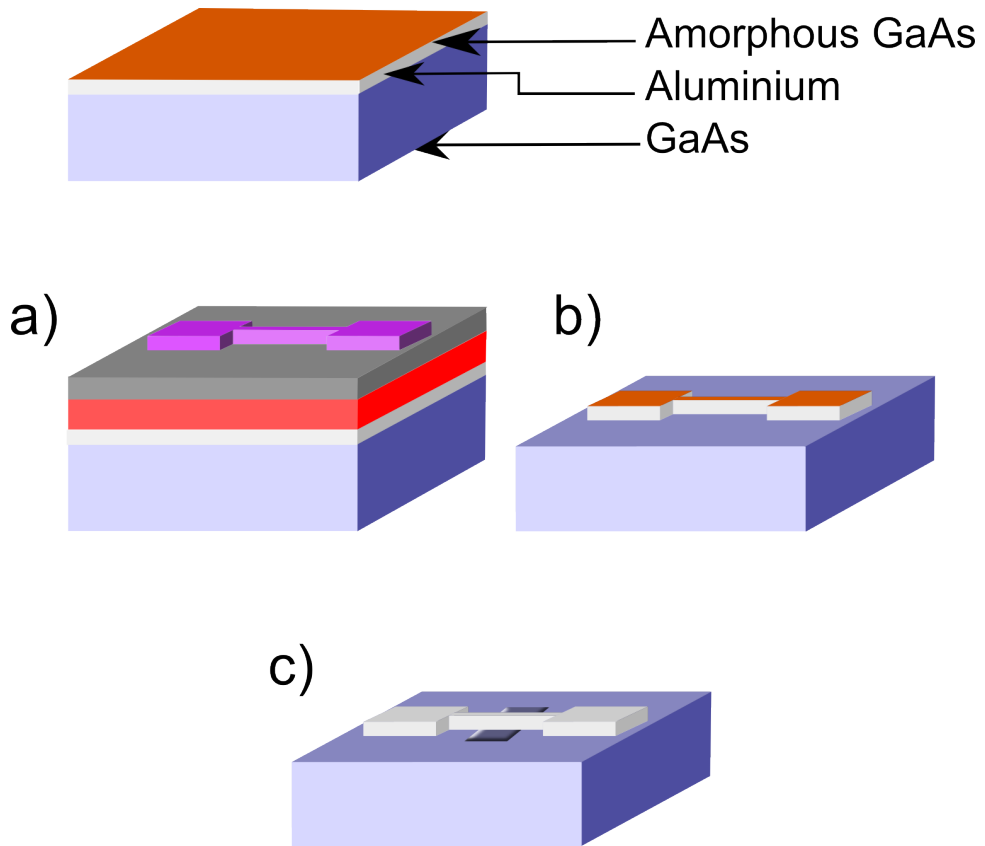


Figure 5.8: Diagram showing the fabrication process of single crystal aluminium resonators. a) The shape of the resonator is defined on AR-N7520 via EBL, b) the aluminium is etched via a chlorine dry etch, c) the aluminium beam is released via etching a window in the GaAs using a citric acid and hydrogen peroxide wet etch. N.B. images are not to scale.

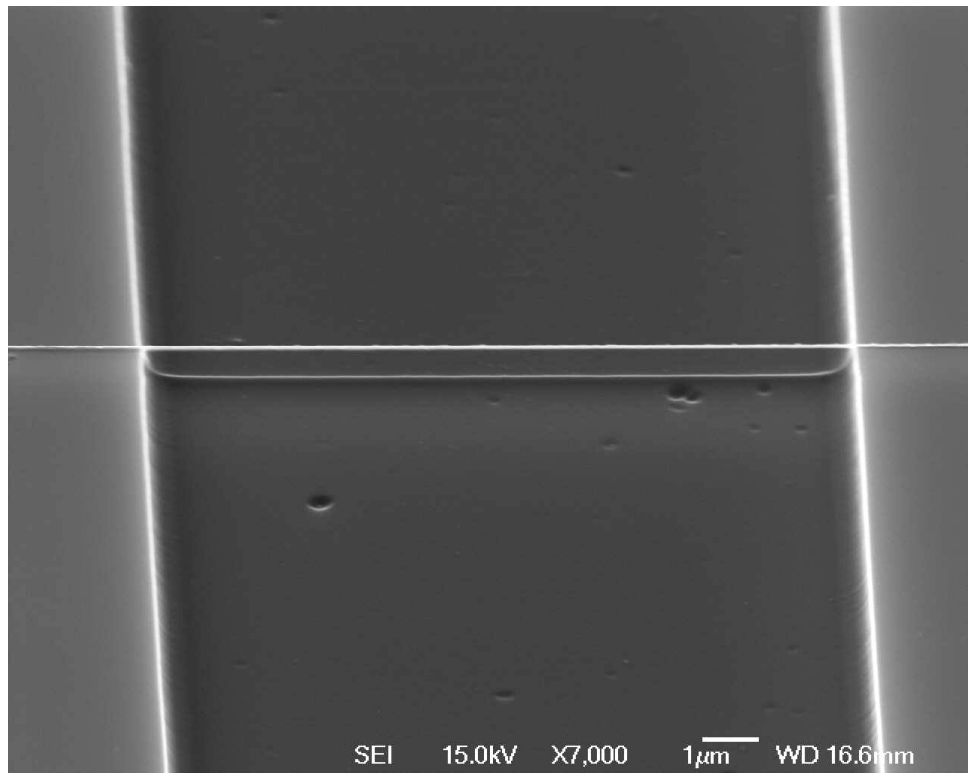


Figure 5.9: SEM image of an monocrystalline aluminium beam taken at an angle of 45 degrees.

the bridge is required. The PMGI is then exposed via deep UV, then developed before being baked on a hotplate. This baking results in the PMGI reflowing thus creating a smooth profile. This process is then combined with a standard lift off process to deposit metal thus making an air bridge. An SEM image of an airbridge can be seen in Figure 5.10. This method can also be used to make an "igloo", but care must be taken to ensure the solvent used to remove the PMGI can get inside the "igloo". For this reason it is a good idea to include a number of "windows" into the "igloo" design. An entrance to an "igloo" can be also be seen in Figure 5.10.

These structures are also used in the fabrication of on chip LCR circuits which are discussed in the next section.

5.9 Fabrication of on-chip LCR circuit

The LCR circuits (whose design is shown in Figure 5.12) are fabricated from the same wafer as the silicon nitride torsional resonators were and as before the wafer was scribed into 9.5 mm by 9.5 mm squares. After cleaning a 170 nm layer of PMMA A5 was spun onto the wafer and baked. Alignment marks for later steps and contact pads are then exposed using EBL or photolithography (albeit with a different resist) before being developed. As with the torsional resonators the silicon nitride was then roughened using the dry etcher before a layer of chrome

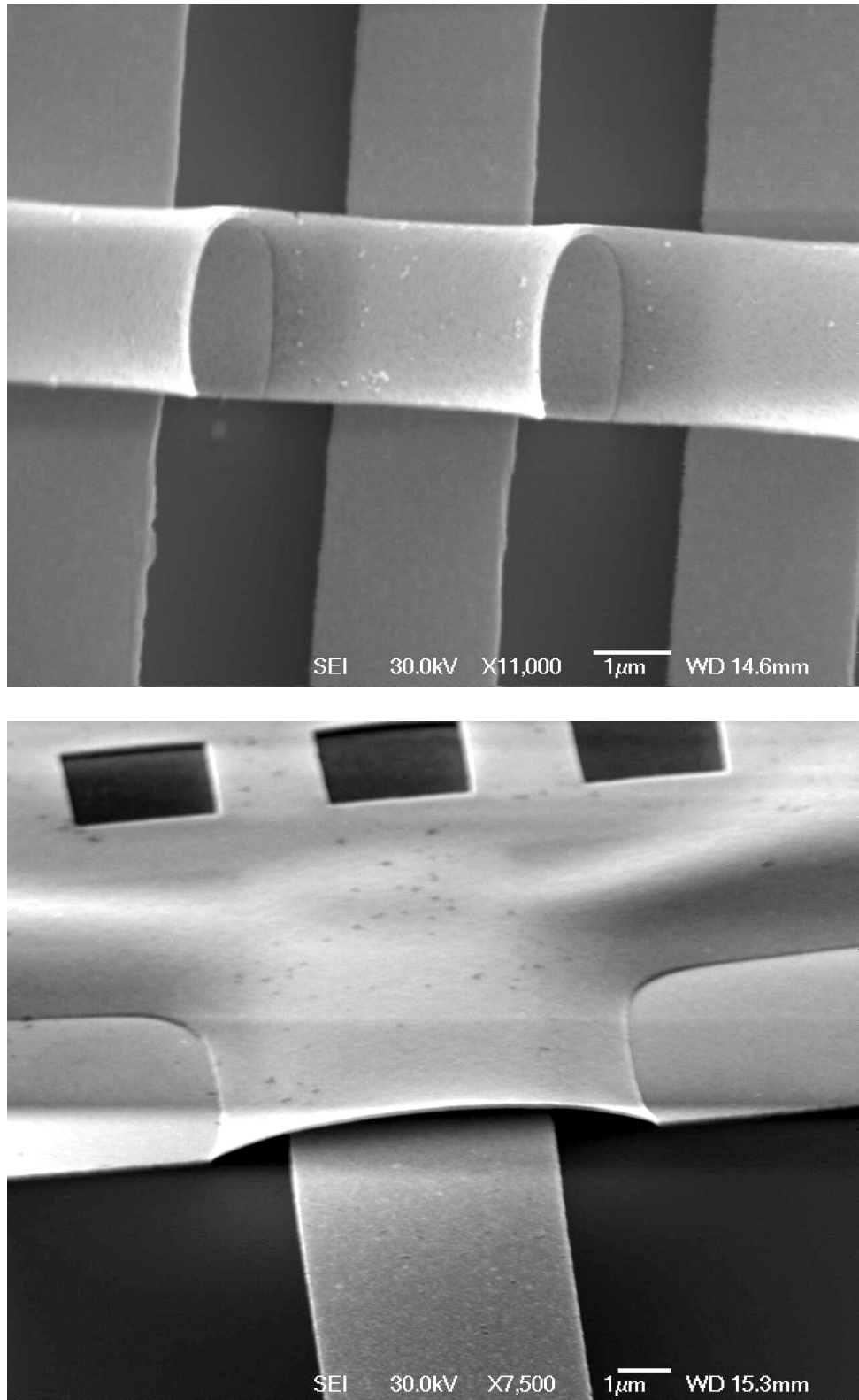


Figure 5.10: SEM image of an airbridge travelling over another wire (top) and the entrance to a parallel plate capacitor (bottom).

and gold was deposited via thermal evaporation. The same process as used in the torsional resonators is then used to make a silicon nitride membrane. Once the membrane is made a 170 nm layer of PMMA is again spun onto the wafer before being softbaked. The bottom capacitor plate, a section of the inductor spiral and underpass (black lines in Figure 5.12) is then exposed using EBL before being developed. A layer of aluminium was then evaporated onto the wafer using an electron beam evaporator. The waste aluminium is then carefully lifted off with minimal agitation in order to protect the membrane. The next step is to create the foundations for the airbridges that will allow for the inductor to bridge over an underpass and the igloo that will form the top plate of the capacitor. This is done by spinning a 500 nm layer of PMGI onto the wafer followed by a 170 nm layer of PMMA A5 with a bake after each layer. The foundations (solid red areas in figure 5.12) are then exposed using EBL before the PMMA was developed as usual. The PMGI is then exposed using deep UV and is then developed. The PMGI was then made to reflow via a bake on a hotplate. Once cooled a 170 nm layer of PMMA A5 was spun onto the wafer. The top capacitor plate and the remaining sections of the inductor spiral (transparent red lines in Figure 5.12) are then exposed using EBL before being developed as usual. A layer of aluminium was then deposited via electron beam evaporation. After the waste aluminium has been lifted off the wafer was dried using the same process as is used for the membranes, this

ensures the top plate of the capacitor does not collapse. A fabrication diagram showing how the airbridges are made for the underpass and inductor spiral is shown in Figure 5.11 and a SEM image of the entrance to the capacitor can be seen in Figure 5.10. It is also possible to replace some of the electron beam lithography steps with photolithography this was used when we wanted to scale up the number of circuits on each chip.

Full details of the process for these devices can be found in the appendix.

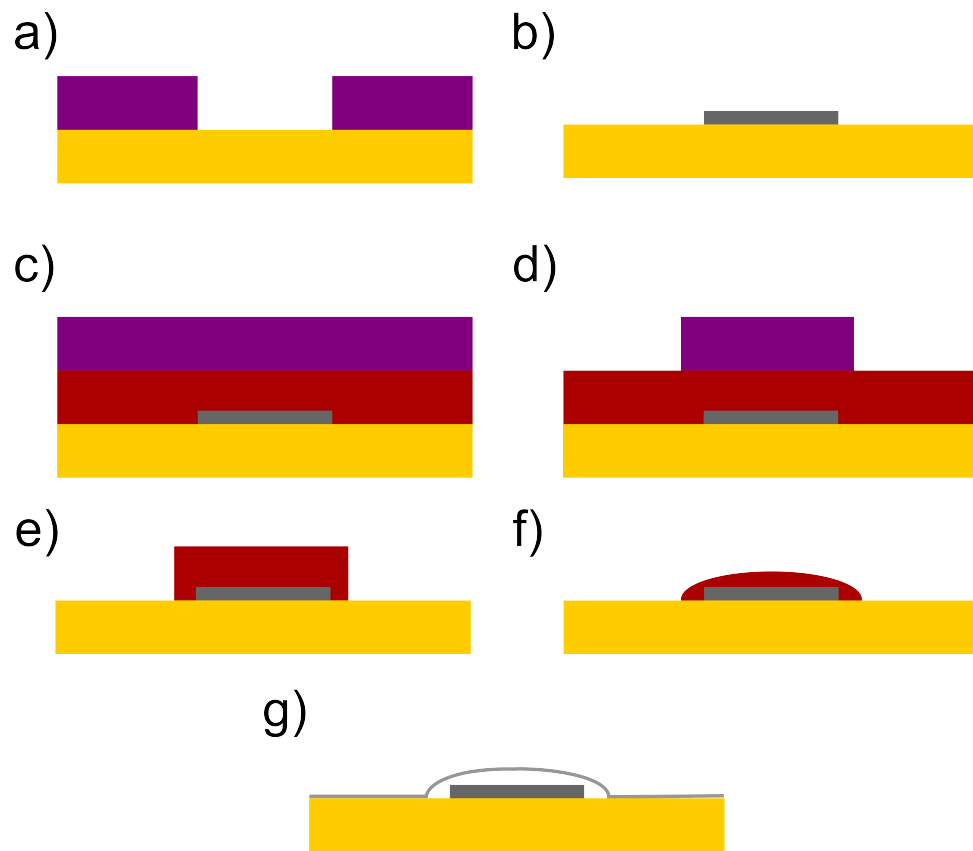


Figure 5.11: Fabrication steps for making an air bridge. a) PMMA is spun onto a wafer before being exposed via EBL and developed, b) metal is evaporated onto the wafer to form either an underpass or the bottom capacitor plate, c) a layer of PMGI followed by PMMA is spun on a wafer, d) the PMMA is exposed then developed, e) the PMGI is also exposed then developed, f) The wafer is heated causing the PMGI to reflow, g) a standard lift off process deposits metal onto the wafer to form either the air bridge or the top capacitor plate.

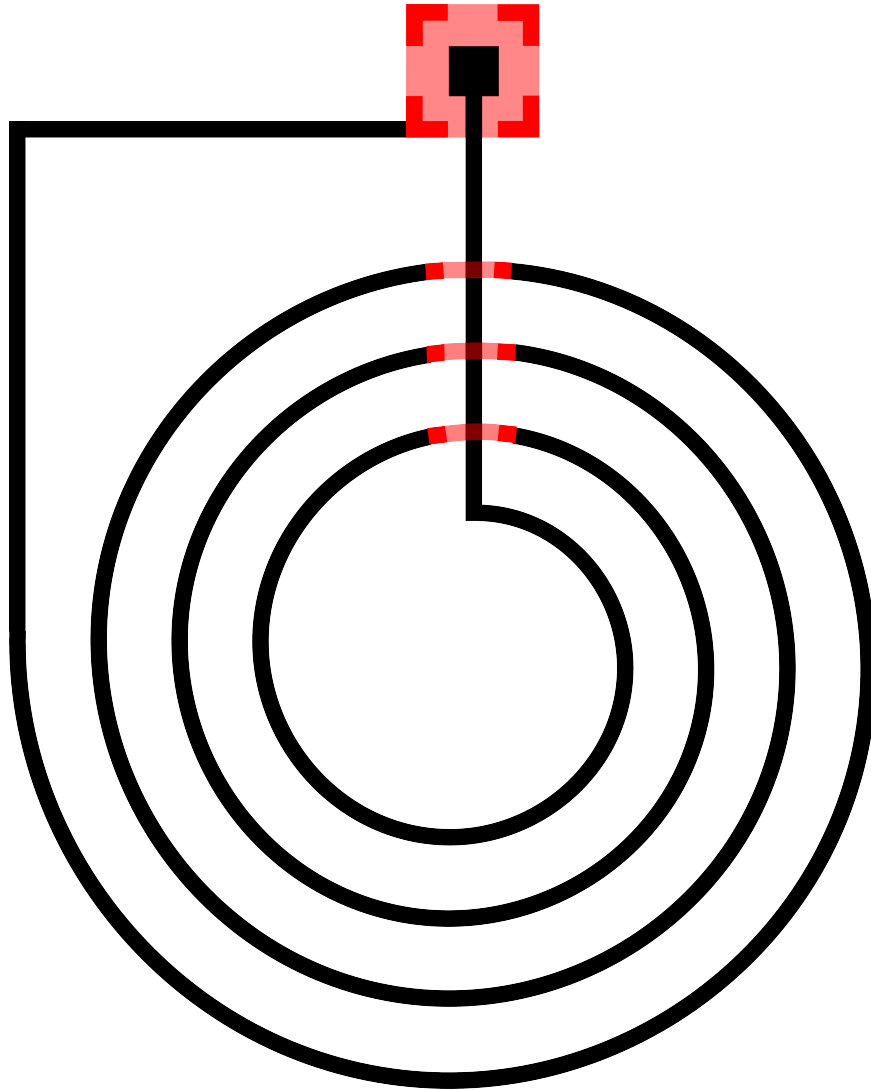


Figure 5.12: Figure showing the design of the LCR on chip circuit. The black areas represent metal placed directly on the substrate, the solid red areas indicated the foundations of the air bridges and top capacitor plate and also indicates metal deposited directly on the substrate. Finally the transparent red areas indicate the suspended metal.

5.10 Conclusion

This Chapter has looked at the methods and equipment used to create a range of different structures from nanomechanical resonators to bow tie nano antennas. We started by looking at the equipment used and discussed how we can combine electron beam lithography with proximity effect correction to make high quality patterns such as gold on glass BNA's with gaps as small as 30 nm. Then we described how this equipment was used to create silicon nitride membranes that could be turned into torsional resonators. Next it looked at how top-down fabrication can be used to create beam resonators made from a single crystal of aluminium. Finally it looked at how airbridges are used to create on chip LCR circuits. In Chapters 6 and 7 we present results that help to further our understanding of thermoelastic dissipation and dissipation due to TLS. The following chapters describe how we used these fabrication techniques to create a number of different nanomechanical resonators and details the methods used to measure them and the results we obtained from them.

Silicon Nitride Torsional Resonators

In the past decade many studies have focussed on looking at the mechanical properties of silicon nitride [20, 54, 55]. There are a number of reasons for this, firstly it is a very versatile material when it comes to fabrication. Whilst depositing it is not simple, once it has been deposited highly selective etches can be used to make a range of devices including simple beams, torsional resonators and membranes. The second reason why it is of interest is that it can be deposited with a very high in-built stress, this high stress leads to nanomechanical resonators with extraordinarily high Q factors. This chapter looks at work performed on triple and single paddle torsional resonators, where we were able to use a novel actuation method to preferentially actuate the torsional mode of the resonator which to our knowledge has not been done previously using a piezoelectric drive.

This chapter describes the optical detection method used to both image and detect the resonator. It will also mention the actuation method that was able to actuate either the torsional or flexural mode of a torsional resonator. It will then go on to present results performed at room temperature on two different designs of torsional resonators before discussing the results and comparing the results with published work.

6.1 Measurement Techniques

A common method used to detect the motion of a resonator is optical detection. This has to be combined with a drive mechanism such as piezoelectric drive. Using a piezoelectric drive allows a wide range of frequencies to be actuated. Optical detection works by combining the resonator into an interferometer. In the case of this work we used a Fabry-Perot interferometer to detect the motion of the resonator. The Fabry-Perot interferometer works by creating a cavity between two surfaces, in the case of this work the cavity is formed between the resonator and the substrate. To do this we used light from a coherent source (either a diode laser, or a HeNe laser) that undergoes a number of reflections within the cavity, as illustrated in Figure 6.1.

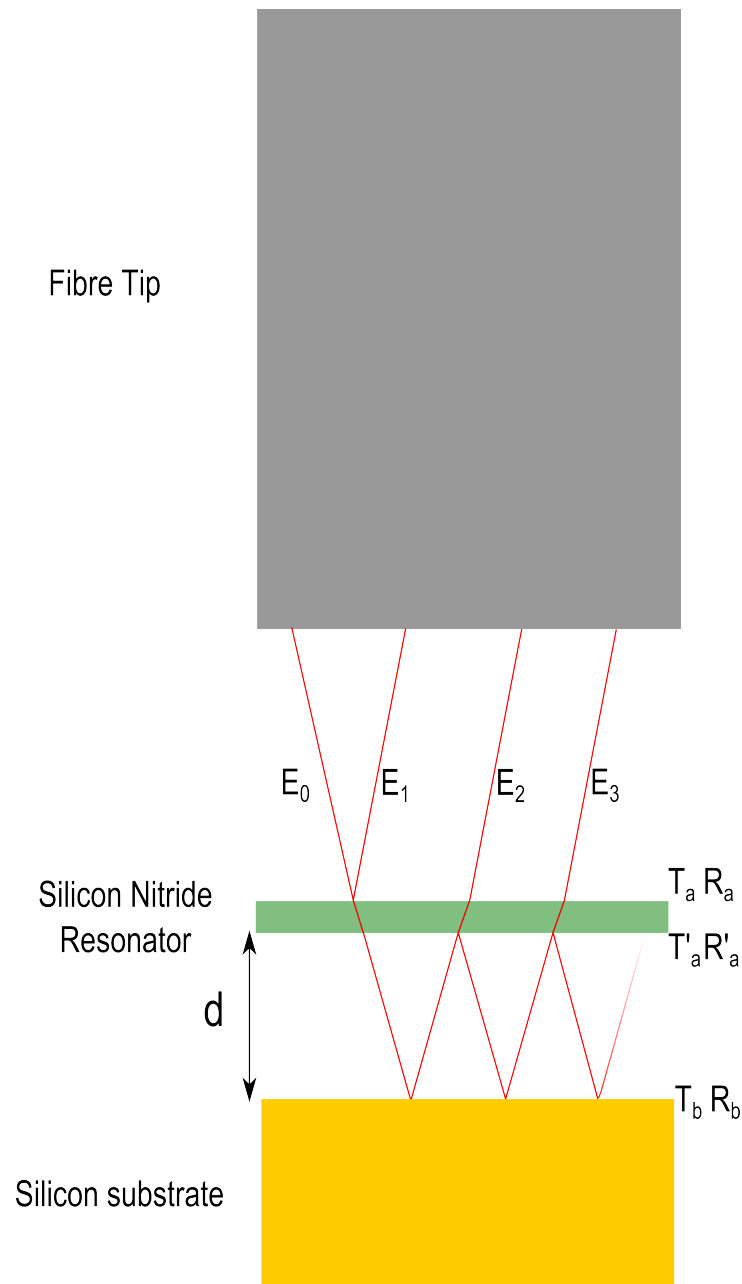


Figure 6.1: Diagram showing how a Fabry-Perot interferometer is created between the resonator (with coefficients of reflections and transmission of R_a and T_a respectively) and the substrate (R_b and T_b).

For an interferometer with two surfaces that have coefficients of transmission T_a and T_b and coefficients of reflection R_a and R_b the electric field amplitude, E , of the reflected beams are,

$$\begin{aligned}
 E_1 &= E_0 R_a e^{i\omega t} \\
 E_2 &= E_0 T_a T'_a R_b e^{i\omega t} e^{i\phi} \\
 E_3 &= E_0 T_a T'_a R_b^2 R'_a e^{i\omega t} e^{i\phi} \\
 E_n &= E_0 T_a T'_a R_b^{(n-1)} R_a^{(n-2)} e^{i\omega t} e^{i\phi},
 \end{aligned} \tag{6.1.1}$$

where ϕ is the phase difference between reflections, and ω is the frequency of the light. The total amplitude of the reflected beam, E_r , is just the sum of all the individual contributions such that,

$$\begin{aligned}
 E_r &= E_0 e^{i\omega t} [R_a + T_a T'_a R_b e^{i\phi} \sum_{m=2}^{\infty} (R_a R_b e^{i\phi})^{m-2}] \\
 E_r &= E_0 e^{i\omega t} \left[R_a + \frac{T_a T'_a R_b e^{-i\phi}}{1 - R'_a R_b e^{-i\phi}} \right].
 \end{aligned} \tag{6.1.2}$$

Using Stoke's relations, $R = -R'$ and $TT' = 1 - R^2$, we are able to simplify this to

$$E_r = E_0 e^{i\omega t} \left[\frac{R_a + R_b e^{i\phi}}{1 + R_a R_b e^{-i\phi}} \right]. \tag{6.1.3}$$

The irradiance of this reflected beam, I_r is equal to the square of its amplitude, which as it is complex is, $|E_r|^2 = E_r E_r^*$ meaning that,

$$I_r = |E_r|^2 = E_0^2 e^{-i\omega t} e^{i\omega t} \left[\frac{R_a + R_b e^{i\phi}}{1 + R_a R_b e^{-i\phi}} \right] \left[\frac{R_a + R_b e^{-i\phi}}{1 + R_a R_b e^{i\phi}} \right] \tag{6.1.4}$$

after expanding the brackets and using the relationship $2 \cos \phi \equiv (e^{i\phi} + e^{-i\phi})$ we get,

$$I_r = E_0^2 \left[\frac{R_a^2 + R_b^2 + 2R_a R_b \cos \phi}{1 + R_a^2 R_b^2 + 2R_a R_b \cos \phi} \right]. \tag{6.1.5}$$

The reflectance of the cavity, which is what we are interested in measuring is simply the ratio of the irradiance of the reflected and original beam i.e.

$$\frac{I_r}{I_0} = \frac{|E_r|^2}{|E_0|^2} = \frac{R_a^2 + R_b^2 + 2R_aR_b \cos \phi}{1 + R_a^2R_b^2 + 2R_aR_b \cos \phi}. \quad (6.1.6)$$

This shows that for a system with constant coefficients of reflection the only variable is the phase difference, ϕ , which is related to the cavity width, d , by $\phi = 2knd \cos \theta$ where k is the wavenumber and n is the refractive index of the medium (in our case this will equal 1). This means that we can use a piezo to drive the sample on resonance, causing the size of the cavity and therefore the intensity of the reflected light to change.

Figure 6.2 is a graphical representation of Equation 6.1.6 with $R_a = 0.7$ and R_b varying. This figure shows that there are a number of considerations that need to be made to ensure that this method works as well as possible. Firstly, it needs to be ensured that the cavity length is ideally around a factor of $1/2$ or $3/2$ of the wavelength of the light used, this will ensure maximum sensitivity as the gradient of the curve in Figure 6.2 will be at the steepest. In the case of our experiment that uses light with a wavelength around 633 nm this means that the distance between the substrate and resonator should be around 315 or 950nm (assuming that the light enters the cavity close to the normal incidence). The second thing that needs to be considered is what coefficients of reflection the different materials have, as this will again

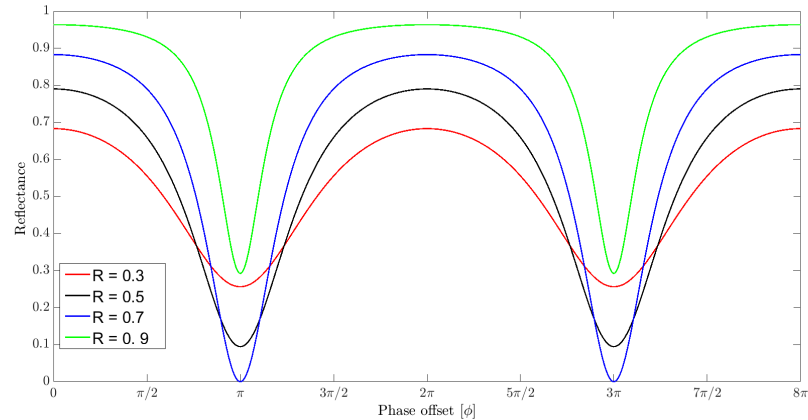


Figure 6.2: Graphical simulation of Equation 6.1.6 showing the change in reflectance of a cavity as the phase shift ϕ changes. The reflectance $R_a=0.7$ while R_b is varied between 0.3 and 0.9.

effect how sensitive the system is. As can be seen it is advantageous to use materials where $R_a = R_b$ and with low absorption, however in reality we are limited to choosing materials that will create the best resonators rather than better cavities.

In results discussed later the light source of the interferometer was a Hitachi 3mW laser diode which is coupled into an optical fibre. The diode laser was chosen over an HeNe laser that was first used. This was because the diode laser had a much shorter coherence length. This meant that it was less sensitive to reflections and scattering in the fibre. This optical fibre is then coupled to a second optical fibre using a "fibre directional coupler" which effectively acts as a beam splitter allowing the reflected beam to be separated from the probe beam. The beam is then sent through an optical assembly that contains a fixed lens and an adjustable lens allowing the beam to be collimated and

then focused. The reflected beam is sent to a photomultiplier tube and then a transimpedance amplifier which converts the current from the photomultiplier tube into a voltage while also amplifying it. A photodiode can also be used to monitor the strength of the original beam.

To actuate the resonator we used a piezoceramic material¹. When a voltage is applied to this it expands or contracts, so by applying an RF voltage we can make it vibrate. The common method of using a piezo to actuate a sample is to use a single piece, however this will preferentially actuate the flexural mode and is unlikely to strongly actuate any of the torsional modes. To compensate for this we introduced a new technique in which two piezos were driven out of phase with each other resulting in a "see-saw" shaking motion. The design of the two different piezoelectric actuators can be seen in Figure 6.4. In both cases the piezo has an RF voltage applied via a signal generator². The voltage from the transimpedance amplifier is then measured by a lock in amplifier³ referenced to the drive frequency. This allows for the response of the resonator to be extracted with very little noise. The electronics are represented in Figure 6.3.

As this method requires the laser to be aligned and focused on the resonator, there needs to be a way of moving the sample around and

¹EBL#2 gold over nickel

²Agilent E4420B

³Stanford Research Systems SR844

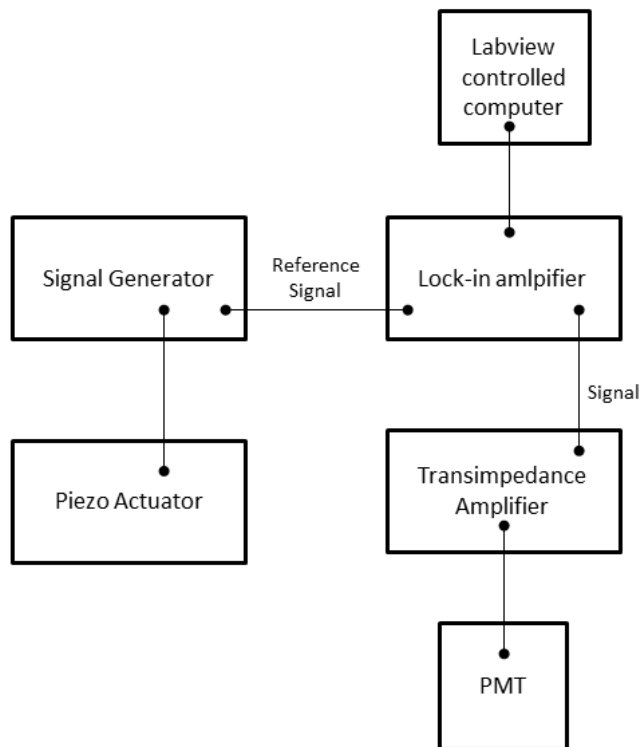


Figure 6.3: Diagram showing the actuation and detection electronics, the piezo actuator is shown in Figure 6.4

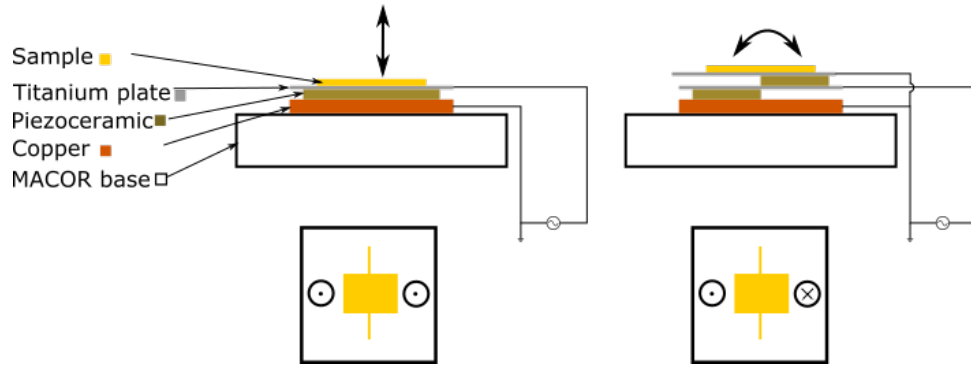


Figure 6.4: Diagram showing the actuation apparatus for the torsional resonators experiment. The set-up on the left preferentially actuates the flexural mods whilst the one on the right preferentially actuates the torsional mode.

Plane view gives an indication as to how the sample is moving for each design.

also of working out where on the sample the laser spot is. To do this we operated the optical system as a confocal microscope. In a confocal microscope light is shone through a small aperture, which in the case of this work is the optical fibre, this gives the beam a Gaussian profile. The light is then collimated and focussed by 2 aspherical lenses onto the surface of the resonator where it is reflected and again passes through the lenses towards the aperture. If the resonator surface is at the focal point of the two lenses the whole of the reflected beam will again pass through the aperture. However, if the surface is not at the focal point only a fragment of the beam will pass through the aperture. The same apparatus as used for the interferometer can then be used to measure the intensity of the returning light at different points of the sample allowing us to build up a picture of the topography of the sample.

To build up a complete picture of the surface of the wafer we need to

be able to move the sample around. This is done by a set of Attocube nanopositioning stages. These nanopositioners allow precise movement on the nm scale, 3 different stages are used allowing movement in the x, y and z direction. At their core is a piezo and set of leaf springs and they work by the "slip stick" method. Much like the trick of pulling a tablecloth out from underneath a glass, they work by slowly applying a voltage to the piezo causing the stage to move in a particular direction then rapidly removing this voltage. Rapidly removing the voltage causes the piezo to return to its original position while, thanks to the leaf springs, leaving the stage in its new position. This process can be repeated to provide a relatively smooth movement over a distance from 10s of nm to a few microns. In our experiment we are able to scan over the sample using the x and y stages and record the intensity at each point. Using this method it takes around 10 minutes to build up an image around $25\mu\text{m}$ by $25\mu\text{m}$. An image of the resonator taken using this method can be seen in Figure 6.5.

The interferometer combined with the z positioning stage also allows for the amplitude of the resonator to be converted from a voltage into a displacement in metres. This is done by arranging the set-up so that a cavity is formed between the end of the fibre tip and the resonator and then measuring the resonator while sweeping the z stage. This sweeping of the z stage alters the size of the cavity. By comparing the intensity of reflected light as a function of cavity size we are able

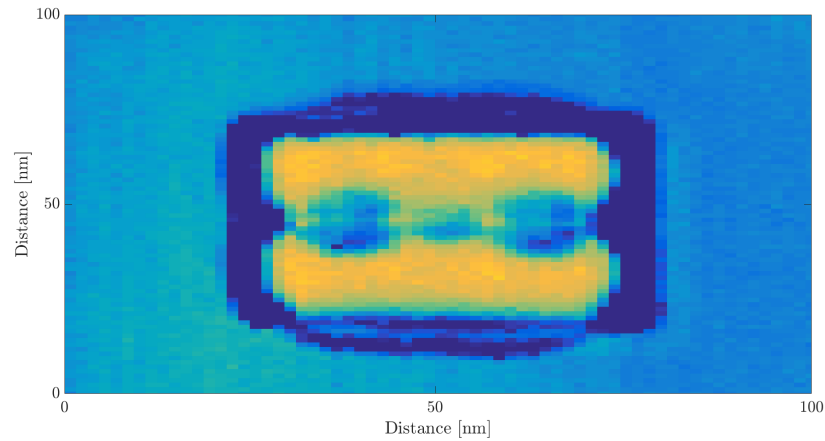


Figure 6.5: Confocal image showing a triple paddle resonator. The yellow region shows where the silicon substrate is visible after the etching of the membrane.

to obtain a conversion factor of 30.7 mV/nm [20]. A diagram of the complete apparatus can be seen in Figure 6.6.

One of the main drawbacks of optical detection is that it requires a resonator with large enough dimensions that the laser spot can be focused onto it and also it requires that the resonator can be easily located. To help with this second point we use a number of location marks on the sample to help locate where we are looking. These take the form of a series of numbers and letters that form a set of coordinates. By knowing the spacing of these coordinates it is possible to relatively quickly find a resonator, this is made easier by including a large number of resonators in a particular area. An example of these location marks taken with the optical set-up operating as an confocal microscope can be seen in Figure 6.7.

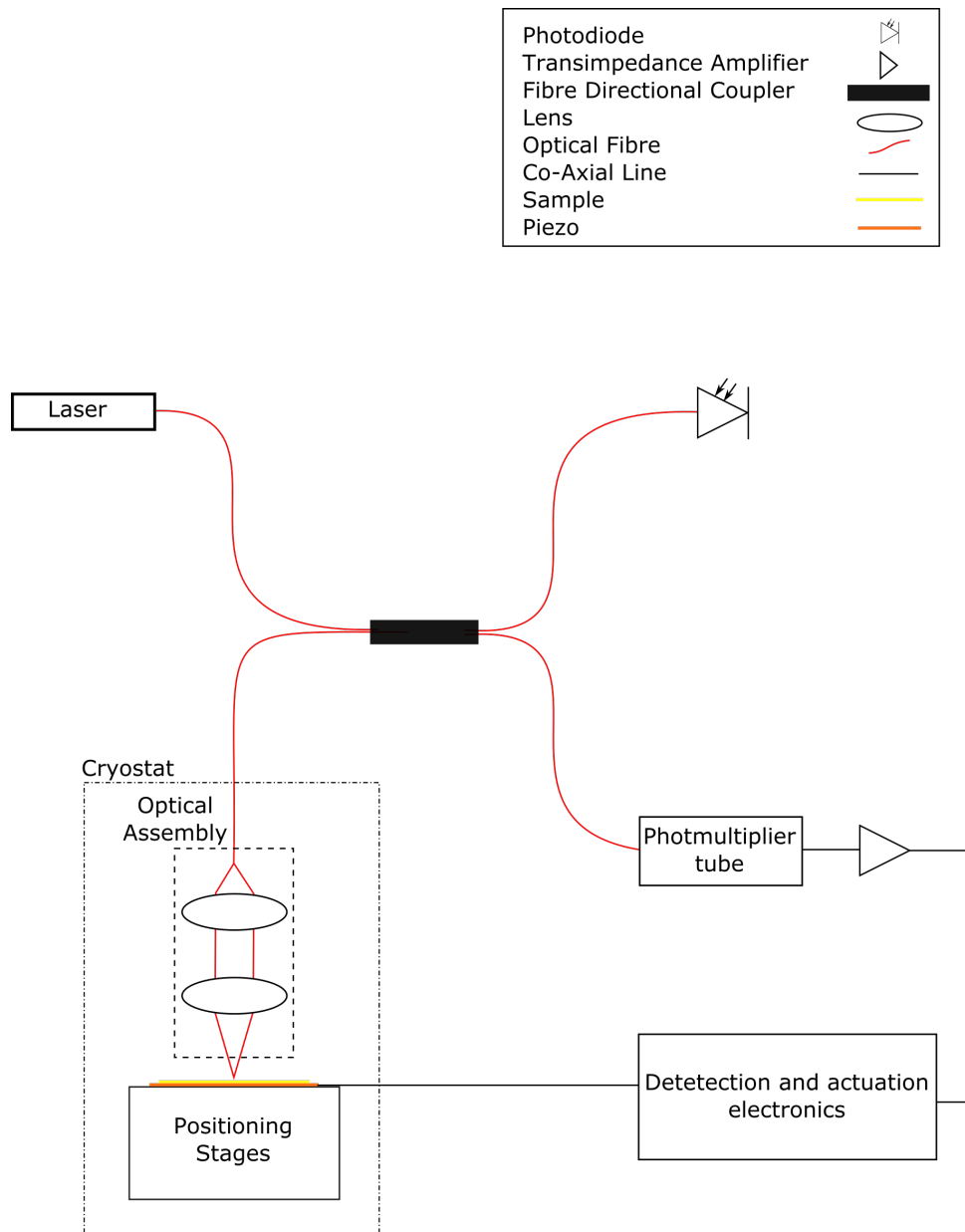


Figure 6.6: Schematic of the optical set up used to measure silicon nitride torsional resonators. The detector and actuation electronics is shown in Figure 6.3



Figure 6.7: Image of location marks taken using while operating the optics set up as a confocal microscope. Image measures around $15\ \mu\text{m}$ by $10\ \mu\text{m}$.

6.2 Results

The first design that was tested can be seen in Figure 6.8a; as can be seen it is a triple paddle design that should allow a number of different normal modes to be actuated. The resonator has a central beam with a cross section of $400\ \text{nm}$ by $70\ \text{nm}$ and has a length of $12\ \mu\text{m}$, the larger paddles measure $3.6\ \mu\text{m}$ by $2.1\ \mu\text{m}$ and the central paddle measures $1.6\ \mu\text{m}$ by $1.6\ \mu\text{m}$. The sample was placed in the set up described in Section 6.1 and then pumped out to a vacuum of 1×10^{-3} mbar. By sweeping between 5 and 20 MHz we were able to see 2 distinct peaks at 9 MHz and 12.5 MHz (Figure 6.9), these peaks were then studied in more detail.

Figure 6.10 shows a frequency sweep around 9 MHz while the piezoelectric actuator was being driven at 0 dBm. As can be seen it does not appear to be a single smooth peak but rather a combination of a

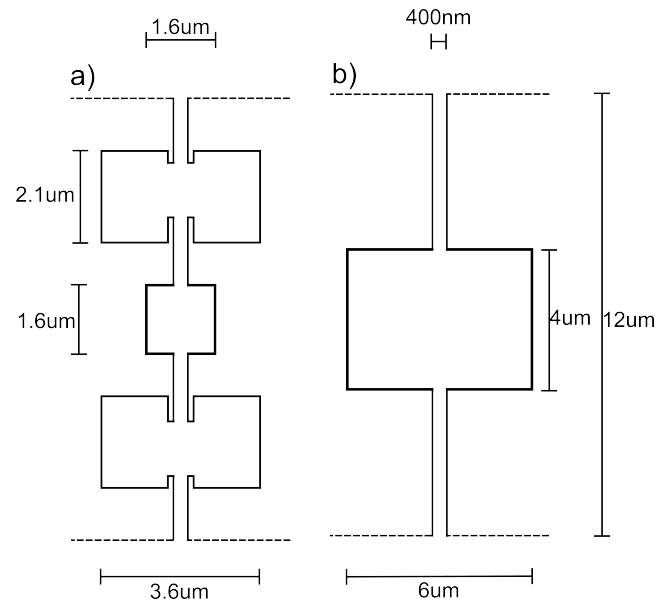


Figure 6.8: Schematic diagram of the, a) triple paddle and b) single paddle torsional resonator. Dashed lines show where it is clamped to the substrate

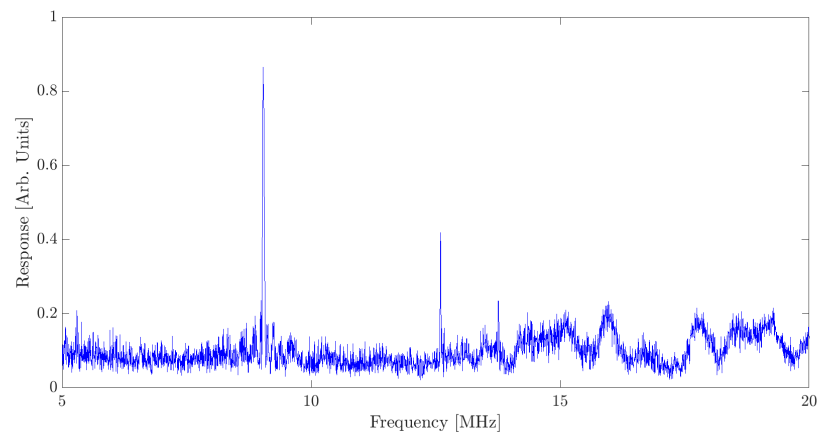


Figure 6.9: Response of the resonator as the piezo is swept between 5 and 20 MHz peaks above 15 MHz are due to electrical noise.

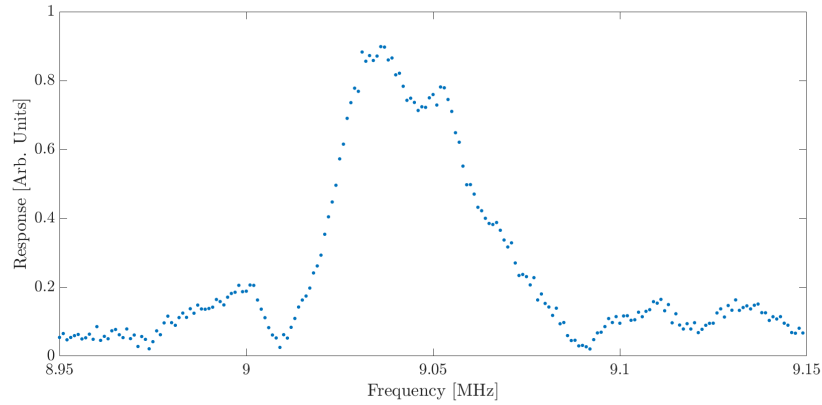


Figure 6.10: Response of the resonator as it is being driven at 0 dBm around the first flexural mode

number different peaks. To investigate this peak further the actuator was driven at 9.05 MHz while scanning the laser interferometer over the surface of the sample, in doing this we are able to record the response and phase of a particular area of the resonator. Figure 6.11 shows that all three paddles of the resonator are moving in phase with each other suggesting that this is the first flexural harmonic of the resonator.

The response close to 12.6 MHz can be seen in Figure 6.12. Again we also recorded the response as we scanned over the the sample while driving it at 12.595 MHz the amplitude and phase of the response can be seen in Figure 6.13. It can be seen that the central paddle is not moving, and the two outer paddles are moving out of phase with each other. This suggests that this is the second flexural mode that is being actuated.

A number of frequency sweeps at various points on the resonator were

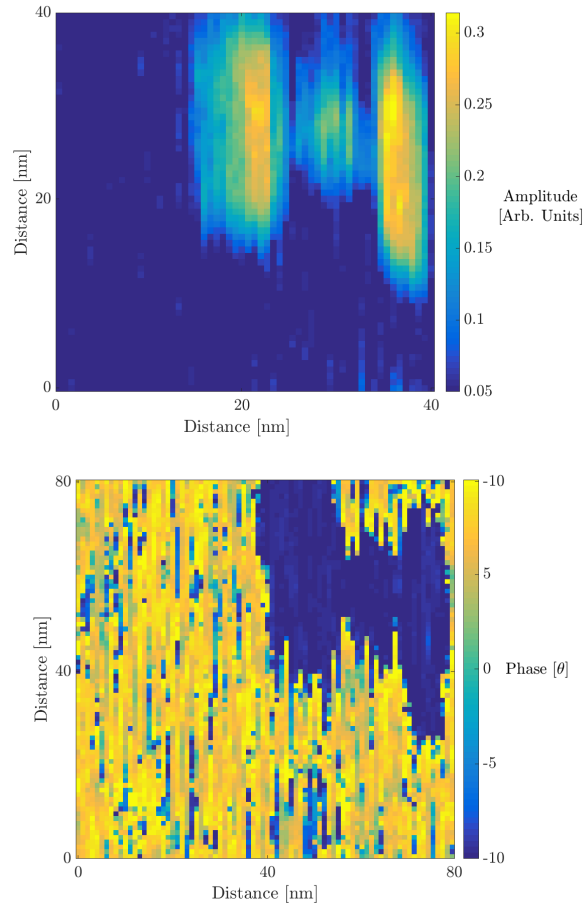


Figure 6.11: Confocal image (measuring approximately $40\ \mu\text{m}$ by $40\ \mu\text{m}$) of the resonator as it is being driven at 0 dBm at 9.05 MHz, the top image shows the amplitude of the resonator while the bottom image shows the phase of the resonator. The shift between the images is due to hysteresis of the scanning stage and the fact the images were recorded on different scans. The colour bars show amplitude and phase respectively

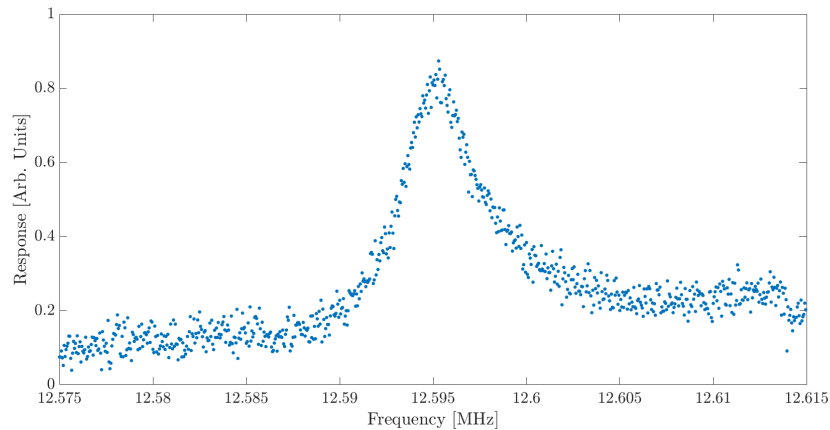


Figure 6.12: Response of the resonator as it is being driven at 0 dBm around the second flexural mode.

made, i.e. sweeps were taken on the central paddle, in the middle of the outer paddle and on the edge of the large paddle, this was done at a range of drive powers for both the first and second flexural modes. Prior analysis of the response of the beam ensured that the resonator was only ever in the linear regime. The recorded voltage was then converted into an deflection by the method described earlier which was then plotted against drive power for the various positions. This can be seen in Figure 6.14.

From these results it seems that we have only been able to actuate the flexural modes of the resonator. This is not surprising as the actuator is shaking the sample perpendicular to the plane of the sample, therefore it will preferentially actuate the flexural modes. To actuate the torsional mode we used the double piezo set up described earlier.

Using this method we only found one response, at 8.45 MHz. The

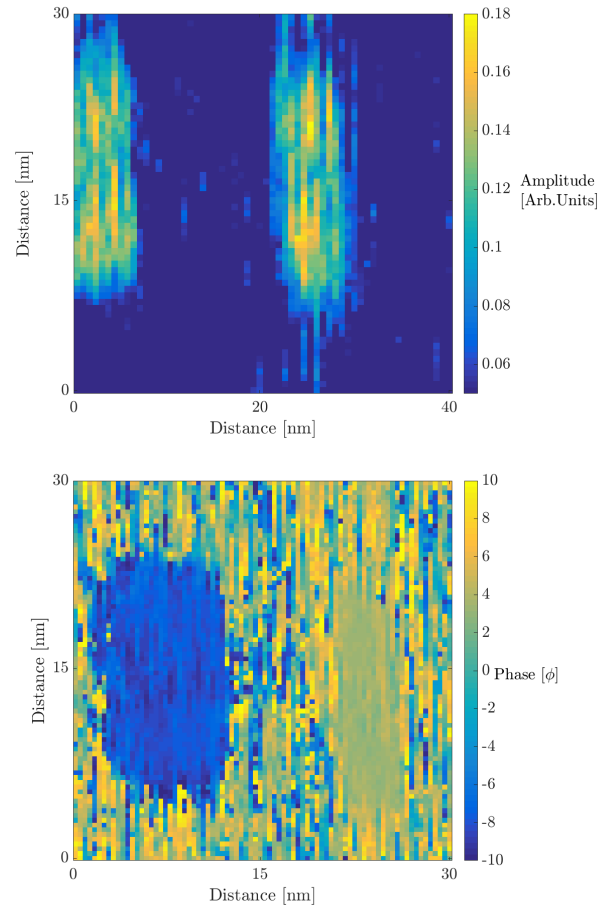


Figure 6.13: Confocal image (measuring approximately $30 \mu\text{m}$ by $30 \mu\text{m}$) of the resonator as it is being driven at 0dBm at 12.595 MHz, the top image shows the amplitude of the resonator while the bottom image shows the phase of the resonator. The shift between the images is due to hysteresis of the scanning stage. The colour bars show amplitude and phase respectively.

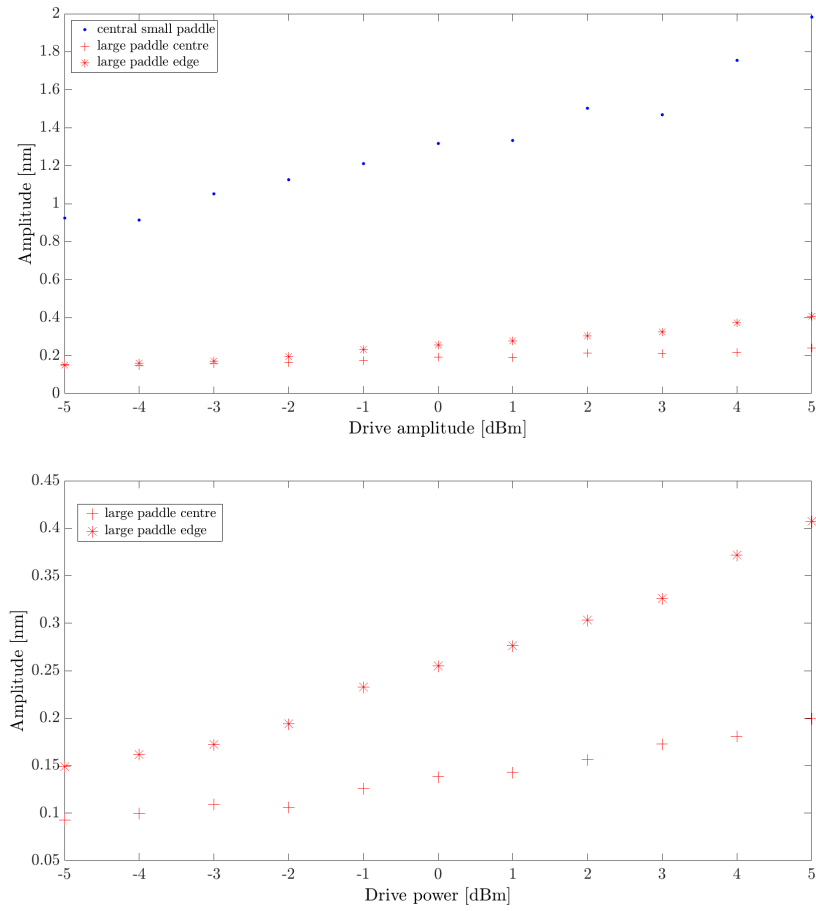


Figure 6.14: Graph showing the amplitude of various points of the resonators motion at various drive powers as it is being driven at the first flexural mode (top) and second flexural mode (bottom). Note the different scale between the graphs

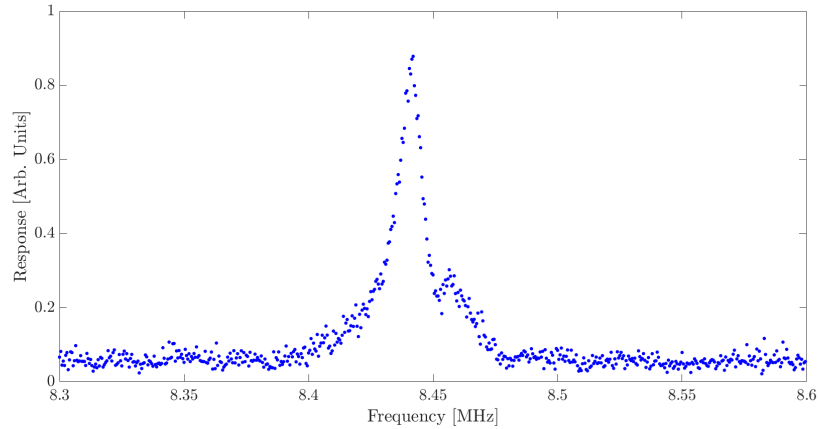


Figure 6.15: Response of the resonator as it is being driven at -16 dBm around a possible torsional mode

response around this frequency can be seen in Figure 6.15. However it is not clear whether or not this is a torsional mode as the response of the different areas of the resonator does not clearly show that all parts are moving in or out of phase with each other. What is odd is that firstly it is at a different frequency to the two modes found earlier and secondly it is the only resonance found using this method. It is possible that this response is a flexural and torsional hybrid mode. As we were not sure that this was a torsional mode we looked at another way to actuate a torsional mode.

In a further attempt to actuate a torsional mode we made a resonator with a single large paddle, the hope here was that it would be easier to actuate this design's torsional mode as the single paddle would have a larger moment of inertia (as discussed in Chapter 2). Using this method we found two peaks one at around 3.1 MHz and one at around 3.6 MHz, sweeps of these resonances can be seen in Figure 6.16, and the phase as

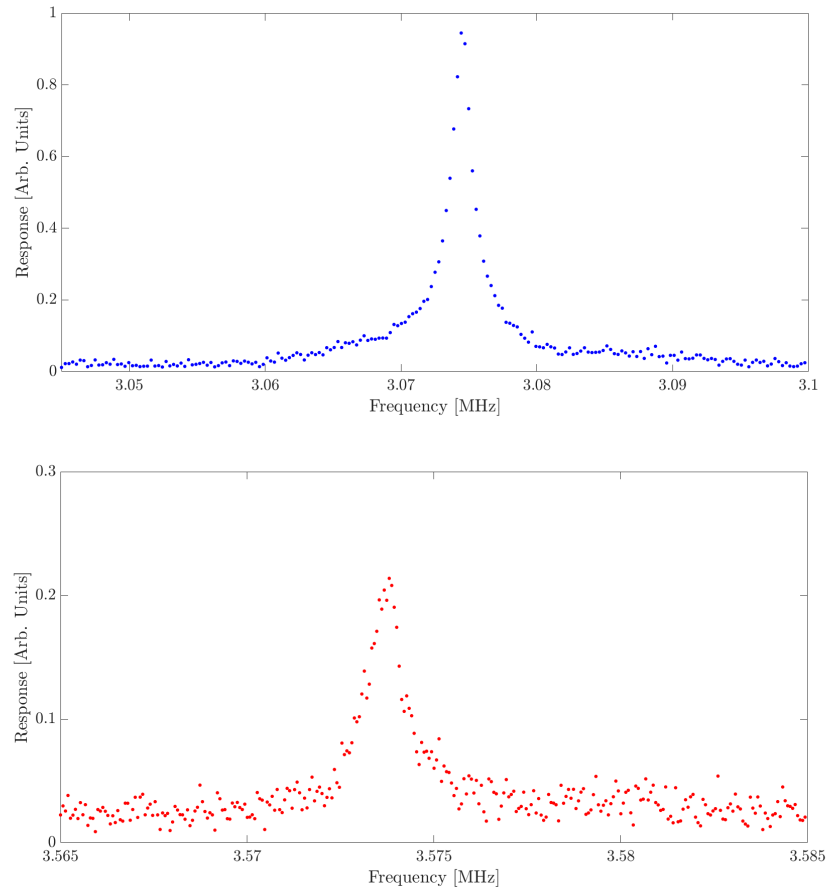


Figure 6.16: Response of resonator as it is being driven around its flexural mode (top, blue) and torsional mode (bottom , red).

we swept across the sample whilst driving at the different modes can be seen in Figure 6.17. This clearly shows that we have managed to drive both the first flexural and torsional modes, this can be seen as in Figure 6.17a the whole resonator is moving in phase whereas in Figure 6.17b the resonator is moving out of phase either side of the central beam. The dot in the bottom image is due to a metallic dot that was placed on the resonator with a view to actuate magnetically.

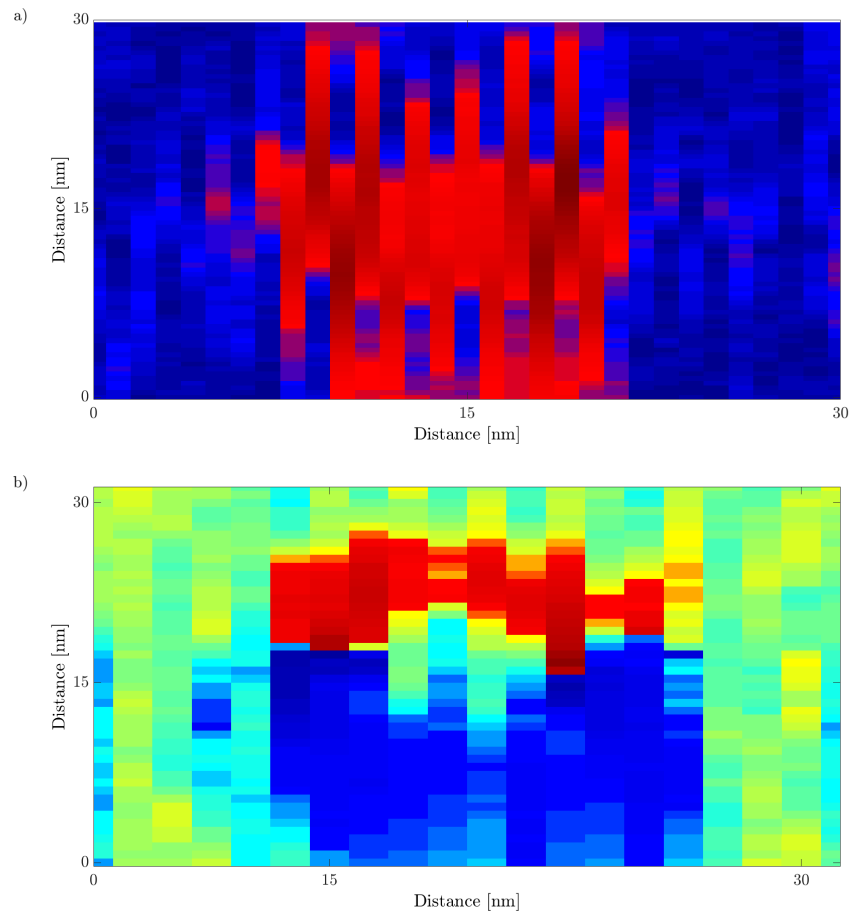


Figure 6.17: Phase of the resonator as it is being driven at 3.07 MHz (a) and 3.57 MHz (b), the different phases of the bottom image indicates that we are driving a torsional mode, whereas the single phase shown in the top image indicates we are driving a flexural mode. The black outline indicates the position of the resonator.

6.2.1 Analysis

To understand the mechanics of the silicon nitride resonators the first thing we need to do is extract the Q factor and resonant frequency of the resonance. To do this we need to fit the response to the equation of motion of the beam as shown in Equation 2.1.22. However to this equation we need to add a non zero, frequency dependent background to account for the signal produced by the detection electronics. A MATLAB program based on the approach by Kozinsky [9] takes the real and imaginary parts of the response of the resonator and fits them to the equation,

$$R(\omega) = \frac{Ae^{i(\theta - \frac{3\pi}{2})} \frac{\omega_0^2}{Q}}{(\omega_0^2 - \omega^2) + i \frac{\omega\omega_0}{Q}} + B_0 + B_1(\omega - \omega_0), \quad (6.2.1)$$

where $A = \sqrt{A_{imag}^2 + A_{real}^2}$ is the quadrature of the real and imaginary parts of the measured amplitude signal, θ is the phase, ω_0 is the resonant frequency, ω is the drive frequency, Q is the quality factor and B_0 and B_1 are the constant and frequency varying backgrounds respectively. This means that we are able to extract, the amplitude, Q factor and resonant frequency of the resonator as long as it is in the linear regime. Figure 6.18 shows one result of the fitting process.

We used this program on all resonances shown here and the obtained values can be seen in Table 6.1 As mentioned earlier it appears that the response of the first flexural mode of the triple panel resonator has a number of peaks. The Q factor shown in Table 6.1 comes from the peak

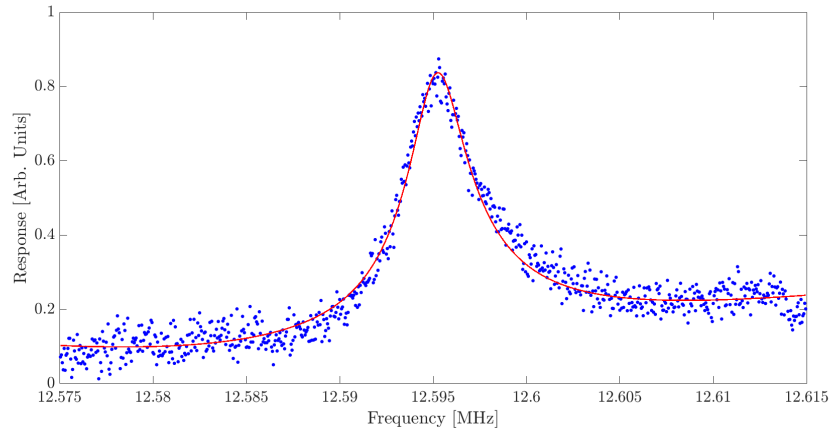


Figure 6.18: Example of fitting program being used on a sweep around the second flexural mode. The red line shows the fit produced by the program which shows it has a high accuracy and deals with the frequency varying background well.

Mode	Resonant Frequency	Q Factor
First Flexural, triple paddle	9.0342 ± 0.0008 MHz	1030 ± 80
Second Flexural, triple paddle	12.5965 ± 0.0001 MHz	4590 ± 390
Possible Torsional, triple paddle	8.4414 ± 0.0001 MHz	1750 ± 110
Flexural, single paddle	3.07448 ± 0.00001 MHz	2870 ± 70
Torsional, single paddle	3.57370 ± 0.00002 MHz	5050 ± 220

Table 6.1: Table showing resonant frequencies and Q factors of the various different modes measured in this chapter.

shown in Figure 6.19. It looks like this shows a fit that does not appear to match well with the points. However there are a number of reasons why we can trust this peak. Firstly other sweeps shown at lower powers only appear to have a single well defined peak yet show very similar Qs. This suggests that other resonances are coupled into the resonator but only at higher drives. The second thing that suggests that this fit is accurate is that whilst the fit does not appear good for the response it fits very well to the phase and other values in Equation 6.2.1. For these reasons we feel that the value for the Q factor and resonance frequency are correct.

It should also be noted that these values were checked against other resonators on the same sample and the results were found to be consistent with very little variation in resonant frequency or Q factor between resonators.

The first thing to note is that, to our knowledge, these values are higher than any other room temperature Qs of similar shaped resonators. This is especially true of the torsional mode that is more than twice as large as ones found by Davis et al. [17] who found a room temperature Q factor of 800 for the torsional mode of a triple paddle resonator actuated using magnetic torque actuation. It should be mentioned that unlike this work the fabrication method used for these devices is easy to scale up to make multiple resonators simultaneously. With regards to single paddle resonators our Q factors are 3 times larger than found by Zhang

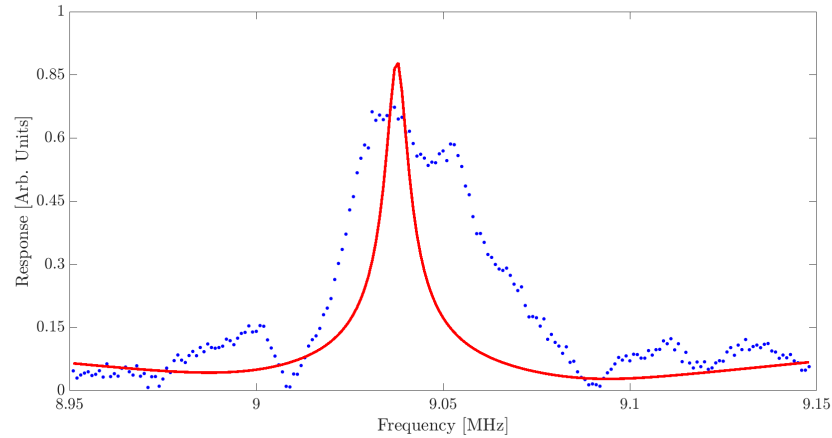


Figure 6.19: Graph showing the fit for the first torsional mode. Whilst it may appear that this is a poor fit, this appears to be due to a number of peaks superimposed on each other. The fitting program is able to differentiate between these peaks.

et al. [56]. They recorded room temperature Q factors of 1555 when using a piezodisk drive. Finally the Q factors are also larger than found in single crystal torsional resonators. Olkhovets, et. al [57] found room temperature Q factors in the region of 2500 using capacitive drive and offsetting the central beam to ensure the torsional mode is activated. Across all these results it is likely that the increase in Q factor is in the main due to the high stress in our silicon nitride layer combined with the quality of our fabrication methods.

These results appear to show two things, firstly that the first flexural mode has greater dissipation than the second. It also appears to show that the flexural mode has greater dissipation than the torsional mode. It may at first glance be surprising that the first flexural mode seems to have greater dissipation than the second mode, as it has been shown

that usually dissipation grows with mode number due to the increased number of bending points [58]. However this model applies to simple beams, and it may not be possible to extrapolate it to a more complicated design that includes paddles. Further support for this view comes from looking at the shape the resonator makes (Figure 6.20). It can be seen that for the first mode the node lies directly over the central paddle whilst for the second mode thanks to the indentations on the larger paddles they lie in an area with no paddle. This could mean that a greater area of the resonator is actually bending in the first mode than the second. Figure 6.14 also appears to support this idea as it shows that the first mode has a larger amplitude suggesting that the beam will be being stretched more. The lower graph showing the second mode shows that the resonator can bend and flex quite a lot under high drives as emphasised by the fact the edge of the paddle gains amplitude quicker than the centre.

Another source of dissipation that needs to be considered is fluid damping. Fluid damping is proportional to the area of the structure, and whilst for beams this means that it is very small, for torsional resonators it will be considerably higher due to the paddle area. However the Knudsen number which is a measure of an objects size with respect to the mean free path of the gas molecules it is moving in is in the 1000s. According to Bhiladvala et al. [14] this means the the fluid will be firmly in the free molecular flow regime. This means that we will

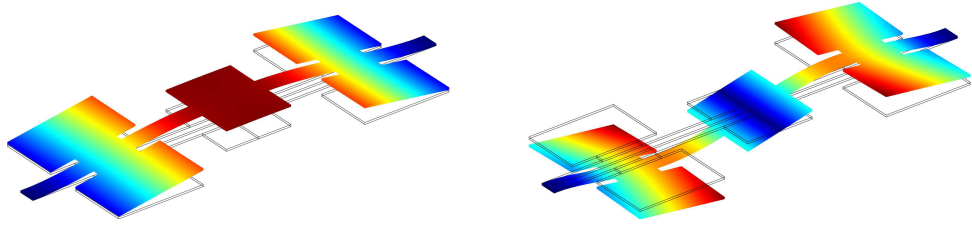


Figure 6.20: Finite element modelling (Comsol) simulation of the first and second flexural modes of a triple paddle resonator. It shows that in the first mode the central paddle will put put under stress, whereas for the second mode thanks to the way the paddle is designed there would be less stress. Colour gives an indication as to displacement with blue being zero deflection and red being maximum displacement

be able to use Equation 3.1.1 to estimate the dissipation due to fluid friction. For the resonator moving in a pressure of 0.1 Pa this gives a maximum Q factor in the region of 100,000. This suggests that at these low pressures there is a more prominent form of dissipation present. However it should be noted that at atmospheric pressures we could not see a response for any of the resonators investigated therefore to fully understand the if fluid friction is important we would need more data. Recording the Q factor of the torsional and flexural modes at a range of different pressures we would be able to see when fluid friction becomes negligible as well as seeing if it varies between modes.

Next we will consider whether clamping losses could be responsible for this dissipation. Whilst some torsional modes have very little clamping losses [17] a single paddle torsional resonator will experience some clamping loss. However in the case of simple beams we have found

clamping losses to be very low [59] with dissipation in the order of 10^{-6} , and this is supported by calculations [60]. This suggests that either clamping losses are insignificant or they are orders of magnitude greater when paddles are added to beam resonators. More evidence that suggests that clamping losses are not important is that results at 4 K for a similar resonator [20] give much lower dissipation and as clamping loss is temperature independent it suggests that clamping losses are not dominant.

A source of damping that could explain these results is thermoelastic damping. In thermoelastic damping the compression and expansion of the resonator causes the transfer of elastic energy to thermal energy. As this experiment takes place at the relatively high temperatures of 300 K this could be a source of dissipation. Evidence that thermoelastic deformation is a key source of dissipation is that for the single paddle resonator the flexural mode has a greater dissipation than the torsional. As there is very little compression or expansion in the twisting motion of the torsional mode it is not expected that thermoelastic dissipation is significant in torsional modes [22]. However that is only true when we are activating a purely torsional mode. It is likely that while our actuation mechanism is able to drive the torsional mode it does this by applying a force in the out of plane direction. This means that in addition to driving the torsional mode it is highly likely that the resonator is also moving in the out of plane direction i.e. having a

flexural mode actuated. With this in mind it is likely that there will still be a degree of thermoelastic damping in the torsional mode.

It is possible to use Equation 6.2.2 to simulate what the dissipation due to thermoelastic damping will be [21].

$$Q^{-1} = \frac{E\alpha^2 T}{C_p} \left(\frac{6}{\xi^2} - \frac{6}{\xi^3} \frac{\sinh \xi + \sin \xi}{\cosh \xi + \cos \xi} \right),$$

where, (6.2.2)

$$\xi = \sqrt{\frac{a_n^2 w^3}{4\sqrt{3} L^2 l_T}},$$

E is the Young's modulus of the resonator, α is its coefficient of thermal expansion, T is the temperature, C_p is its volumetric heat capacity, a_n is a constant depending on the mode number, w is the resonator's width, L , is its length and l_T is the thermal diffusion length in the resonator material. As can be seen the thermoelastic damping strongly depends on the width of the resonator. Figure 6.21 shows the predicted dissipation due to thermoelastic damping for the first two modes.

It should be stated that Equation 6.2.2 and Figure 6.21 are for a simple beam rather than a more complicated torsional resonator. However as most of the flexing occurs on the beam rather than the paddle they are probably still accurate. This means that for a beam 300 nm in width, the dissipation due to thermoelastic damping will be in the region of $3-6 \times 10^{-5}$ which is around an order of magnitude higher than our measured values.

Whilst we know that thermoelastic dissipation should not affect the

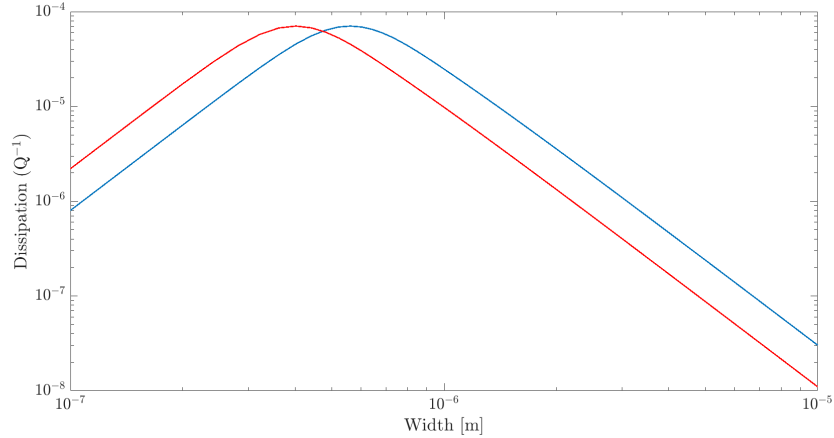


Figure 6.21: Simulation of dissipation in the first (blue) and second (red) flexural mode due to thermoelastic effect for a silicon nitride resonator at 300K.

torsional mode we do need to consider the effect of the paddles. Due to the size of the paddle it is possible that it is either a) flexing, or b) causing an additional load on the beam causing it to flex. If in the process of twisting the paddle bends or causes the beam to flex then it will cause an expansion and compression of the silicon nitride. This would then result in a degree of thermoelastic dissipation. This could go some way to explaining the dissipation in the torsional mode. In addition Tai et al. [22] have in fact suggested that no torsional mode will have zero thermoelastic dissipation as there will always be a flexural component to the mode.

It is interesting to compare these results with those obtained by Verbridge et al. [54]. They looked at simple beam resonators fabricated from high stress silicon nitride. As our silicon nitride was grown in the same facilities it is interesting to compare their Q factor to those ob-

tained in this work. At room temperature they found Q factors around 40000 and a resonant frequency of 40 MHz for a beam 15 μm long, 200 nm wide and 120 nm thick. These values agree well with the value for dissipation due to thermoelastic damping discussed earlier and are 10 times larger than we found in our torsional resonators. What this shows is that at room temperature the flexing of the paddles contribute the vast majority of the dissipation.

To understand the effect the paddles have on the dissipation we need to consider whether or not they flex when the resonator is moving. For the first mode Figure 6.14 shows that the edge of the larger paddle moves more than the centre suggesting that it does flex. In addition images taken in a SEM appear to show that it is possible for the edges of the paddles to bend due to charge build up as can be seen in the top right corner of the resonator in Figure 5.7. This means that it is not possible to simply consider thermoelastic dissipation in the beam. Using finite element modelling software Comsol it is possible to simulate the motion of a paddle (Figure 6.22). This is slightly complicated as we are not clamping the paddle to a semi-infinite rigid plane. However it does appear to show that the paddle will have resonant frequencies in the same frequency range as the whole resonator. This means while driving the resonator we could be actuating a resonant mode of one of the paddles. Following the same approach described earlier we are able to simulate the thermoelastic dissipation but this time for a range

of paddles. Doing this suggests dissipation of a similar order to those obtained in our results. This strongly suggests that the paddles are flexing and therefore causing significant dissipation. However while it is clear that thermoelastic dissipation occurs in the paddles it is likely that we would have to make modifications to equation 6.2.2 to make it fully applicable to paddle resonators. To be able to do this we would need to further investigate the effect of the paddle size on the dissipation. The fact that thermoelastic dissipation is present in the paddles is not a great cause for concern however. This is because due to the temperature, T , and the fact that the coefficient of thermal contraction and specific heat are temperature dependent it has been shown that thermoelastic dissipation is strongly temperature dependent and is negligible at the low temperatures [61]. Therefore it will be possible to remove this source of dissipation by simply reducing the temperature as shown by the Q factor of 10000 found by Patton for the flexural mode at 4.2 K [20]. In doing this a new source of dissipation such as clamping losses or fluid friction will then become dominant.

6.3 Conclusion

This chapter has demonstrated that we are able to create a torsional resonator and actuate both flexural and torsional modes. We were able to obtain room temperature Q factors between 1000 and 5000,

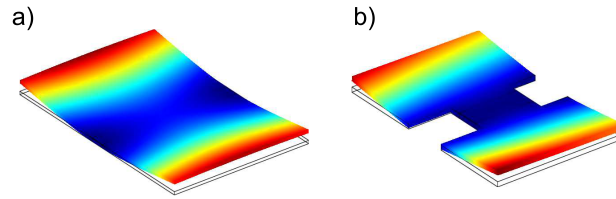


Figure 6.22: Figure showing COMSOL simulations of the largest paddle on, a) the single paddle resonator and b) the triple paddle resonator. It shows when their flexural modes are activated the paddles flex which could result in thermoelastic dissipation.

which are high for these conditions. It is thought that the majority of the dissipation was probably due to thermoelastic dissipation however further experiments would be needed to totally discount fluid friction. It was shown that the dominant source of the thermoelastic dissipation was the paddles.

Unfortunately due to problems with the experimental equipment and due to a lab reorganization we were unable to continue with the experiments on the torsional resonators. This is a shame as if we were able to cool down the resonator we could have looked at the temperature dependence of the Q factor. This would have helped us to discover the dominant damping mechanisms once thermoelastic dissipation was removed. As described in Chapter 5 we were also able to place an metallic dot on a paddle of the resonator and use this set up to probe the magnetic properties of this material [17].

We have demonstrated that we are able to use high stress silicon nitride with novel fabrication techniques to make high quality devices. These fabrication techniques can be easily used with different materials or incorporated into different structures. In Chapter 8 we look at the design of an on-chip LCR circuit which could incorporate a silicon nitride structure.

The next chapter looks at monocrystalline aluminium resonators. As aluminium has an easily obtainable superconducting transition its low temperature properties are very interesting as it could also easily be incorporated into an LCR circuit.

Single Crystal Aluminium

NEMS

The aim of this thesis is to create devices that are capable of making quantum limited measurements. To do this it is interesting to look at materials that have easily reachable superconducting transitions. Thanks to the molecular beam epitaxy (MBE) facilities here in Nottingham we have been able to create a NEMS from a single crystal of aluminium. As explained in Chapter 2 this is useful, as thanks to the lack of internal defects arising from grain boundaries, a single crystal resonator should have reduced damping due to two level systems. If as is suspected this resonator exhibits higher Q factors than similar resonators made from polycrystalline aluminium previously investigated by other groups [4, 31, 33, 34] then we could use the techniques described in Chapter 5 to create a device that could be measured with quantum limited accuracy.

As the dimensions of these beams are smaller than those of the silicon nitride resonator and as the aluminium is less reflective we can not use the optical detection method used in Chapter 6. Instead we use the commonly used magnetomotive method. This chapter starts by discussing the physics behind the magnetomotive method and the set up used in the experiments on the monocrystalline aluminium resonator. This includes a brief discussion into the workings of a dilution refrigerator. It then goes onto present the results obtained with a monocrystalline aluminium resonator at 4 K and 1.5 K before discussing these results and comparing them with other groups.

7.1 Experimental Method

7.1.1 Magnetomotive detection

One of the commonest methods of measuring NEMS devices is the magnetomotive method. The magnetomotive method has a number of benefits, firstly it is a way of both actuating and measuring the resonator, secondly it can be used for resonators of any size as long as they are conducting, and finally it is quite straightforward.

The magnetomotive method was first developed by Cleland and Roukes [19], and uses the Lorentz force law to actuate the resonator. A resonator of length L , placed in a magnetic field, B , will experience a force

if a current, I , is passed through it. If this is an alternating current this force, $F = LBI(t)$ will cause the beam to move sinusoidally according to the equation

$$m \frac{d^2 u(t)}{dt^2} + \gamma m \frac{du(t)}{dt} + ku(t) = LBI(t) , \quad (7.1.1)$$

where $u(t)$ is the displacement, k is the resonator's spring constant, and γ is a damping coefficient. If we use the solution that $u(t) = u_0 e^{i\omega t}$ the displacement will be,

$$u(t) = \frac{LBI(t)}{m(\omega_0^2 - \omega^2)} + \frac{im\omega\omega_0}{Q_0} , \quad (7.1.2)$$

where Q_0 is the unloaded quality factor and ω_0 is the resonant frequency of the undamped resonator.

This displacement, according to Faraday's law will generate an EMF equal to,

$$V_{emf}(t) = \frac{d\Phi}{dt} = \xi_n LB \frac{du(t)}{dt} , \quad (7.1.3)$$

where Φ is the flux, and ξ_n is a geometric constant which is the integral over the length of the beam of the mode shape $g(x)$ and equals 0.83 for $n=1$ [19]. Combining Equations 7.1.2 and 7.1.3 we get an equation for the relation between EMF and drive frequency,

$$V_{emf} = i\omega \frac{\xi_n LBI(t)}{m(\omega_0^2 - \omega^2) + \frac{im\omega\omega_0}{Q_0}} . \quad (7.1.4)$$

This generated EMF opposes the current flow, therefore it increases the impedance in the wire causing a drop in the measured voltage, with

the maximum impedance being reached when $\omega = \omega_0$. This voltage drop can be measured in two ways, either via a network analyser¹ in transmission mode which generates an rf signal and then measures the voltage drop after it passes through the resonator. Alternatively we can use a signal generator with a lock in amplifier² referenced to the signal generator. The benefit of this second method is that it allows for longer sweeps to be taken with more averaging thus increasing the signal to noise ratio.

To examine the effects on the Q factor, of whether or not the aluminium was in its superconducting state, we need to be able to measure its response while it is in both states. The problem with using the magnetomotive method is that it requires the use of magnetic fields. As magnetic fields cause superconductivity to be suppressed we must ensure that we use small magnetic fields. For a film 30 nm thick the critical field will be in the region of 0.5 T [62]. This critical field is a lot higher than it is in bulk aluminium where it is around 10 mT [63]. This is because at these thicknesses the aluminium beam acts as a type 2 superconductor rather than a type 1. This is due to the fact the London penetration depth of aluminium is in the same order as the thickness of the beam [64] meaning that it can remain superconducting even in relatively high fields and currents. The critical current for a thin film has been shown to be around 40 μA [31]. This means that to take readings in

¹Aglient 8712E2

²Stanford SR844

the superconducting regime we will have to use magnetic fields below 0.5 T, it is likely that at these fields we will not have to worry about the critical current. For experiments in the normal regime we will have to use fields above 0.5 T and use Equation 3.1.3 to ensure that Q factors are comparable.

7.1.2 Experimental Set Up

To cool the sample we use a dilution refrigerator to reach temperatures as low as 40 mK. A dilution fridge uses a mixture of ^3He and ^4He [65]. Whilst ^4He is normally superfluid at temperatures below 2.177 K when it is mixed with ^3He its superfluid transition is reduced such that once the ^3He concentration reaches 67.5% it no longer has a superfluid transition [65] (Figure 7.1). When the two isotopes are mixed they split into two parts a ^3He rich phase and a ^4He rich phase. As ^3He is lighter than the ^4He the ^3He rich phase floats on top of the ^4He rich phase. As the temperature is reduced the amount of ^3He in the ^4He rich phase is reduced to a minimum of 6.6% whilst the ^3He rich phase becomes purely ^3He . By pumping on this mixture ^3He atoms evaporate from the ^4He rich phase. To maintain the concentration of ^3He atoms in the ^4He rich phase ^3He atoms move to the ^4He rich phase. This process can be thought of as an evaporation of ^3He into the ^4He rich phase and as such will have an associated latent heat. This latent heat is acquired by absorbing heat from the environment thereby cooling the sample.

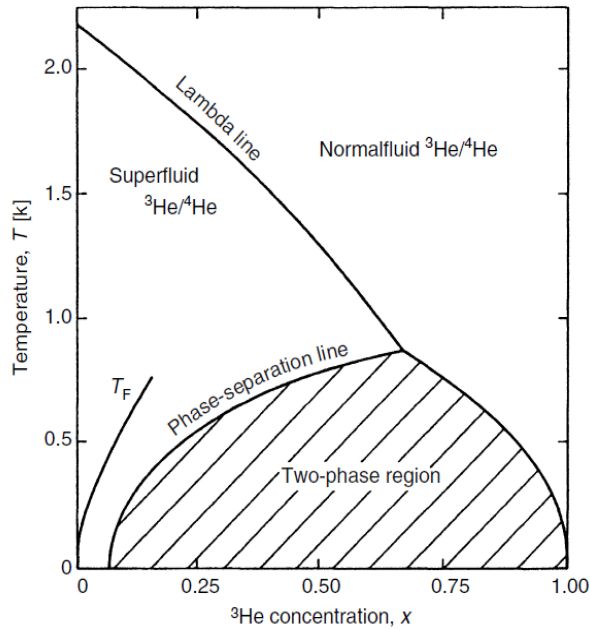


Figure 7.1: Phase diagram of ${}^3\text{He}/{}^4\text{He}$ mixture at saturated vapour pressure. Reproduced from [65]

The main parts of a dilution fridge are a mixing chamber, where the phase boundary occurs, and a still, which is used to store ${}^3\text{He}$. These are connected by a number of heat exchangers and flow impedances. The still is pumped on to continuously remove the ${}^3\text{He}$. This ${}^3\text{He}$ is then condensed back into the fridge to create a continuous cycle. The returning ${}^3\text{He}$ is precooled by a 1 K pot before reaching the heat exchangers. The cold ${}^3\text{He}$ moving from the mixing chamber to the still passes through a heat exchanger that cools the returning ${}^3\text{He}$ (Figure 7.2).

The flow rate of the ${}^3\text{He}$ is controlled by applying heat to the still. The more heat applied to the still the higher the flow rate. As the cooling

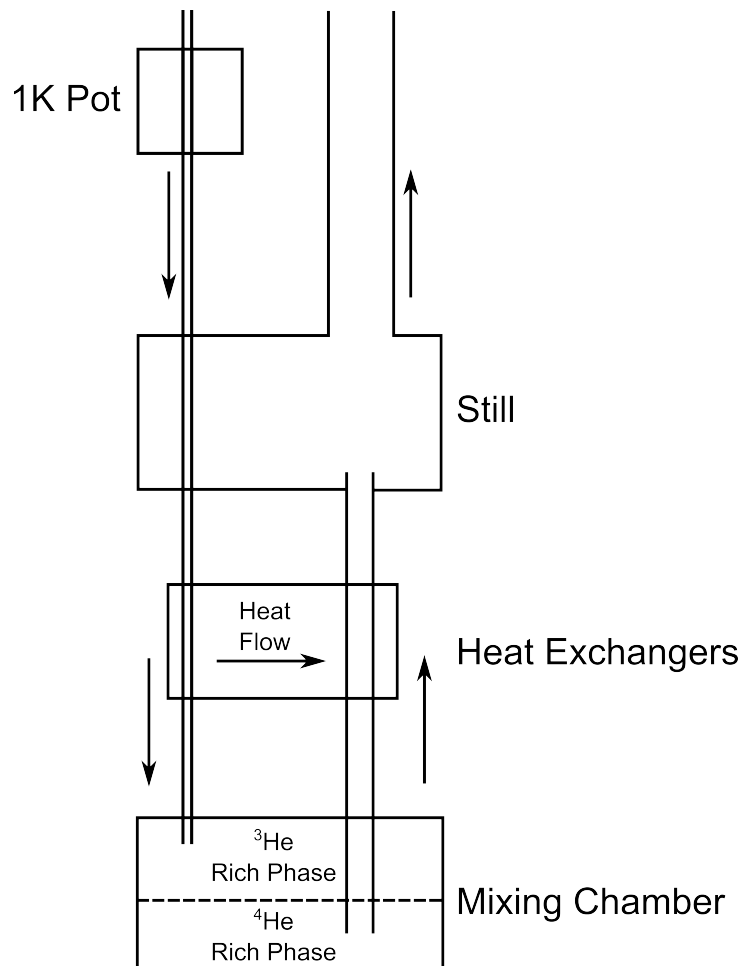


Figure 7.2: Schematic of a dilution fridge, not shown is the room temperature pumping system used to circulate the ³He or pump on the 1 K pot.

power, \dot{Q} of the fridge is defined by [65],

$$\dot{Q} \propto \dot{n}_3(T_{mc}^2 - T_{ex}^2), \quad (7.1.5)$$

where \dot{n}_3 is the flow rate of the ^3He and T_{mc} and T_{ex} is the temperature of the mixing chamber and nearest heat exchanger respectively, this will effectively cool the fridge.

A diagram of the experiment on single crystal aluminium beams can be seen in Figure 7.3. The sample is attached to a 12 pin sample holder with gold wires used to bond the contact pads to the pins. The sample holder is then attached to a piece of circuit board which is used to both help ground the signal and acts as a heat sink for the sample (Figure 7.4). The circuit board is orientated so that the magnetic field causes an out of plane vibration of the resonator. To ensure that the resonator is at as low a temperature as possible it needs to be thermally grounded. This is done via the coaxial lines being carefully attached to the cold finger which is in thermal contact with the mixing chamber. To remove the heat from the central wire of a coaxial line the signal is transferred to a 50Ω gold on sapphire co planar waveguide (Inset to Figure 7.4). These waveguides have an attenuation of less than -1 dB. Additionally the coaxial lines are also thermally grounded at an attenuator at the still temperature. The value of these attenuators depends whether or not it is an incoming or outgoing signal. Higher attenuations are used for the incoming signal in order to protect the sample and reduce the thermal noise. The coaxial cables used are a combination of semi-

flexible CuNi and Cu coaxial cables. These were chosen as they have a low frequency independent dissipation at frequencies below 100 MHz (around -10 dB each side of the sample). Outside of the fridge there is a variable attenuator on the line to the fridge and two room temperature amplifiers on the return line to amplify the returning signal by 50 dBm. The temperature of the fridge is monitored via a series of RuO₂ resistor. These are located on the sample stage, the mixing chamber, the still, the cold plate between the still and mixing chamber and finally on the 1 K pot. The temperature is monitored using a 4 wire measurement by a resistance bridge ³. The resistance can then be converted to a temperature. Finally the fridge also includes a pair of superconducting magnets that surround the sample space and create an in plane magnetic field up to a maximum of 12 T the direction of the field is noted on Figure 7.3.

7.2 Results

The beams used measured 8 μm and 12 μm long, 200-400 nm wide and 30 nm thick. The beam was orientated so that it was actuated via the magnetomotive method described earlier in the out-of-plane direction. As the beam is cooled down it is put under a stress, σ , due to the differential thermal contraction of aluminium as compared to

³Oxford Instrument AVS-47

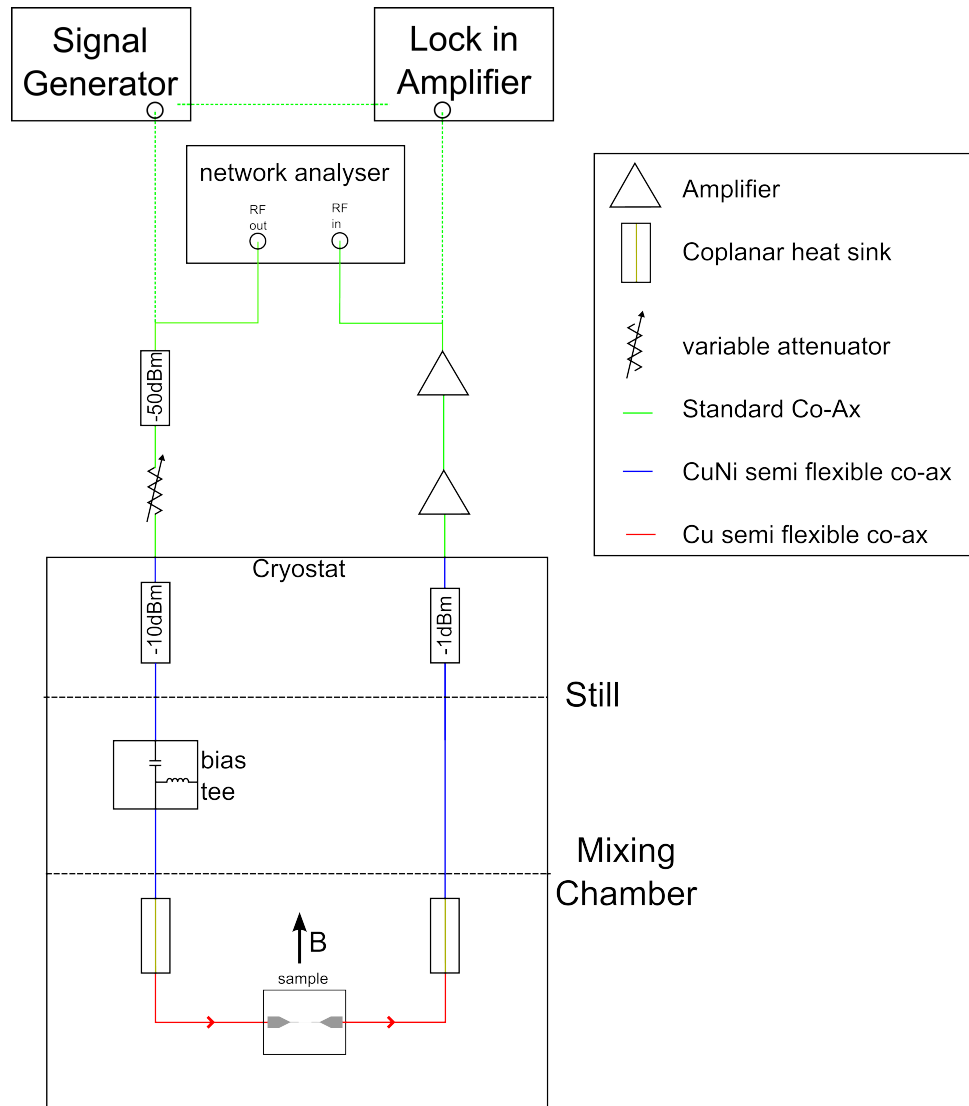


Figure 7.3: Diagram showing the experimental set up used in the experiments on the single crystal aluminium beams. The direction of the magnetic field is also indicated.

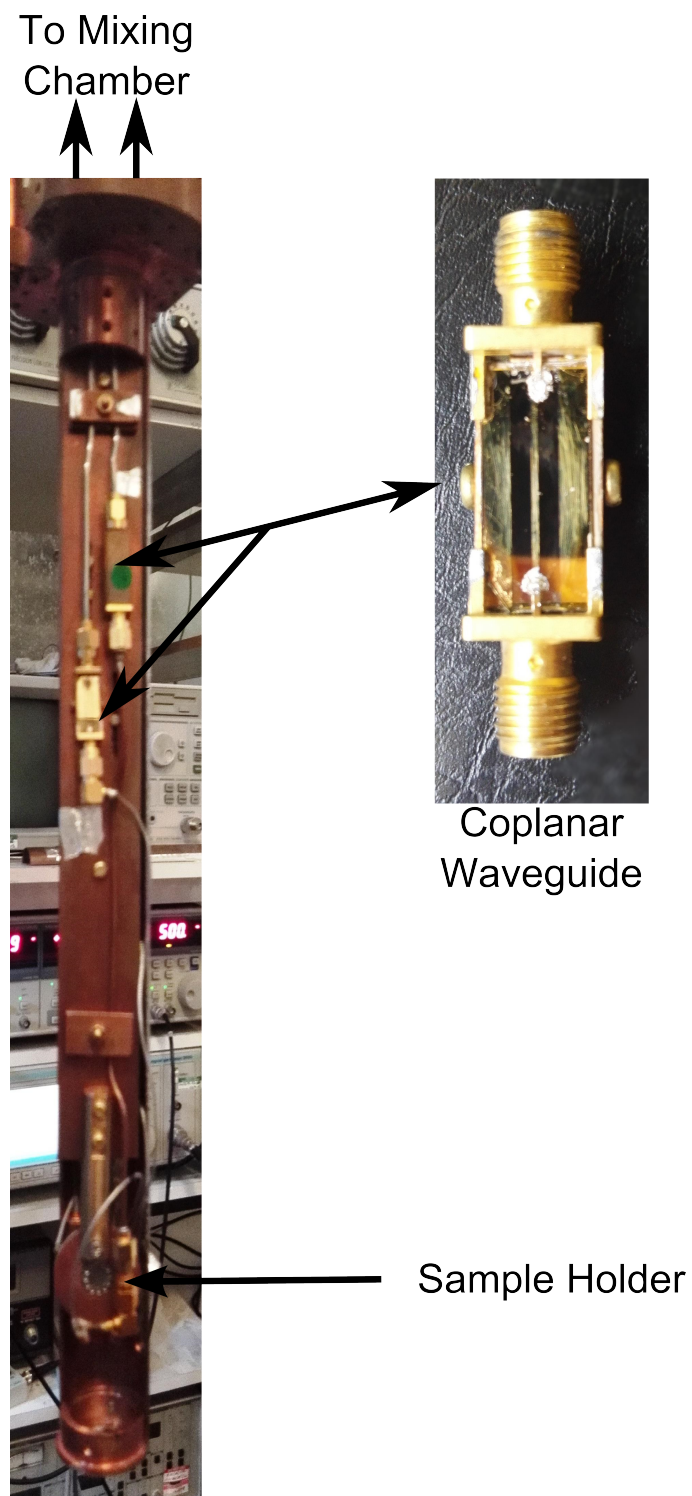


Figure 7.4: Picture of the coldfinger used for the experiments on aluminium NEMS, inset shows an enlarged image of the coplanar waveguide heat sink.

GaAs. Calculating the expected resonant frequency of the beams is not straight forward as the coefficient of thermal expansion is a function of temperature for both GaAs and aluminium. This means that we have to sweep over a wide frequency range to find the resonance. Figure 7.5 shows the response of the beam close to 12.47 MHz at a drive level at the sample of -100 dBm and with an applied field of 2.5 T. Using Equation 2.1.22 it is possible to estimate that this 12 μm beam has an stress of 190 MPa. In addition to the response at 12.47 MHz the third harmonic was found at 38.44 MHz, also shown in Figure 7.5. As expected for the magnetomotive method this higher harmonic had a much smaller amplitude and the exact frequency and Q factor could only be detected at magnetic fields above 3 T.

Figure 7.6 shows the dissipation of the resonator at several magnetic fields for both the first and third harmonic. All the results were taken at pressures below 1×10^{-5} mbar and at 4.2 K with a drive power of -100 dBm with the first harmonic being recorded using a network analyser whilst the results for the third harmonic were taken with a signal generator and lock in amplifier as this improved the signal to noise ratio.

As can be seen in Figure 7.6 there is a linear relationship between the square of the applied field and the dissipation of the resonator as expected from Equation 3.1.3. This shows that the resonator is in the linear regime as the dissipation does not seem to be affected by the size

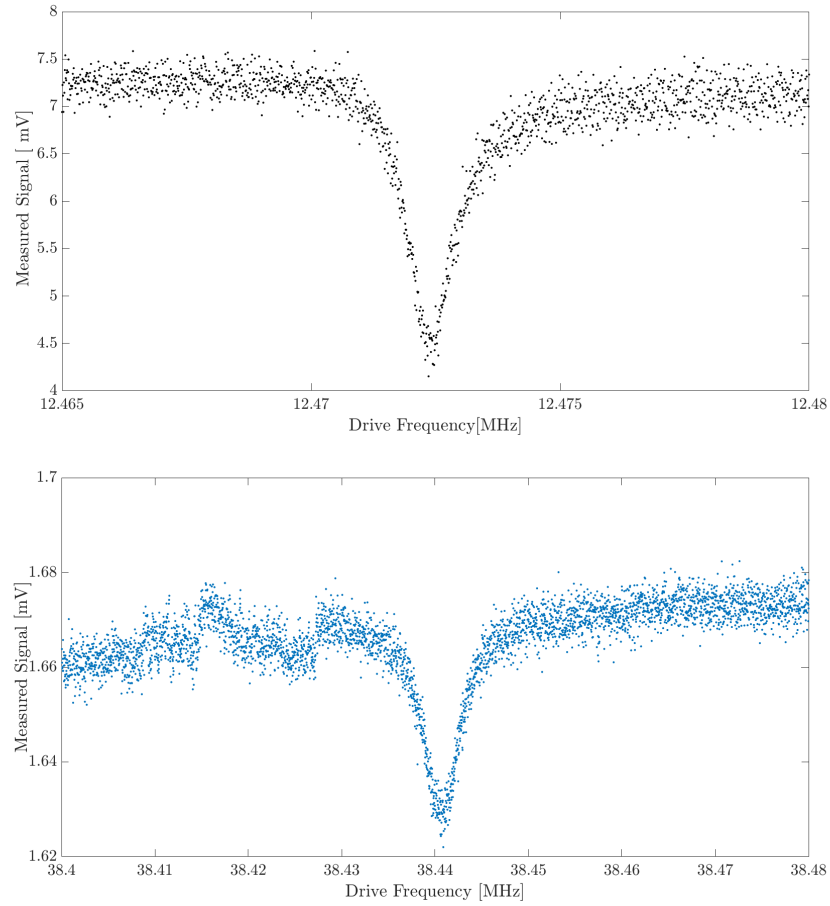


Figure 7.5: Response of the resonator as it is being driven at -100 dBm at 4.2 K at a pressure of below 1×10^{-5} mbar. The top graph shows the response of the resonator around its fundamental resonant frequency at a field of 2.5 T with a resonant frequency of 12.4723 ± 0.0001 MHz and a Q factor of 9970 ± 110 . The bottom graph shows the response of the resonator around its third harmonic at a field of 4 T with a frequency of 38.4403 ± 0.0004 and a Q factor of 9300 ± 190 .

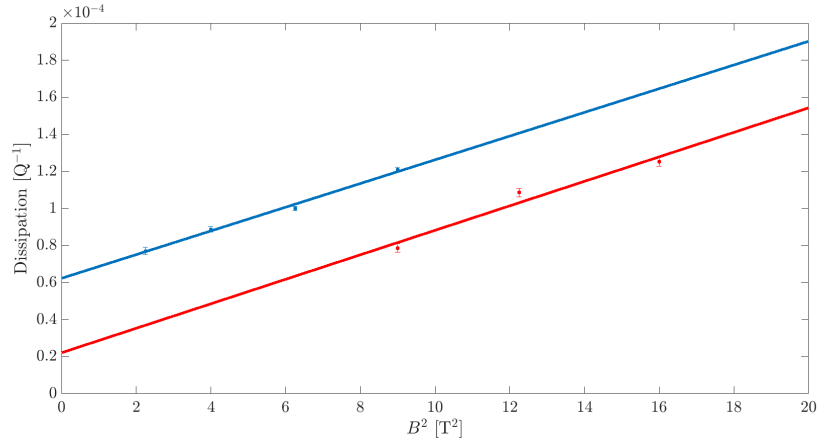


Figure 7.6: Dissipation against the square of the applied magnetic field for the first (blue) and third (red) harmonic at 4.2 K. The frequency did not drastically alter from the values given in Figure 7.5. Lines shows fit to the Equation 3.1.3.

of the drive force. Fitting to these points allows us to calculate the unloaded Q factor of the resonator, that is the Q factor of the resonator when there is no dissipation due to the magnetomotive measurement scheme. In fitting to Equation 3.1.3 we get a value of η of $(6.40 \pm 0.04) \times 10^{-6}$ which gives an unloaded Q factor of 16000 for the first harmonic and 45200 for the third. These are considerably larger than those seen on polycrystalline aluminium on silicon nitride.

On cooling the resonator down to 1.5 K it was noted that the fundamental frequency of the beam decreased significantly by 180 kHz down to 12.2917 MHz suggesting a decrease in tension of around 3% which could not be explained by thermal contraction. Meanwhile the unloaded Q factor of the fundamental resonance rose to 36900 from 16000. Full details of the obtained results can be seen in Table 7.1

T/K	B/T	f/MHz	Q	Amplitude/mv
4.2	1.5	12.4723 ± 0.0001	12983 ± 353	1.29 ± 0.04
4.2	2	12.4723 ± 0.0001	11276 ± 190	2.02 ± 0.04
4.2	2.5	12.4723 ± 0.0001	9973 ± 110	2.79 ± 0.03
4.2	3	12.4685 ± 0.0001	8270 ± 78	3.25 ± 0.03
1.9	2.5	12.2914 ± 0.0001	6277 ± 53	2.37 ± 0.02
1.5	2.5	12.2917 ± 0.0001	6333 ± 53	2.43 ± 0.02
1.5	2	12.2912 ± 0.0001	18968 ± 209	1.82 ± 0.02
4.2	4	38.440 ± 0.0004	9299 ± 187	0.041 ± 0.009
4.2	3.5	38.441 ± 0.0004	9214 ± 200	0.037 ± 0.007
4.2	3	38.441 ± 0.0001	12712 ± 198	0.025 ± 0.007

Table 7.1: Results from the single crystal aluminium beam, all results were taken at pressures below 1×10^{-5} mbar and a drive of -100 dBm. First harmonic measurements (those with frequencies around 12 MHz) were taken with a network analyser while third harmonic measurements (those with frequencies around 38 MHz) used a lock in amplifier.

7.3 Analysis

It seems that the third harmonic has a higher unloaded Q factor than the first which goes against other work looking at the dependence mode number has on Q factor. This work suggests the Q factor decreases as mode number goes up [58]. The difference gets worse if you look at the product of the frequency and Q factor, fQ , which are even further apart. It is not clear at the moment why this is occurring but if we were able to investigate higher harmonics we may be able to find an answer to this deviation from the norm.

These results are surprising as it is not expected for large changes in Q and f_0 to take place above the crossover temperature T^* mentioned in Chapter 3 which is normally around 1 K [34]. This is because as the coefficient of thermal contraction for aluminium is also effectively zero the temperature dependent dissipation mechanism of thermoelastic damping is effectively zero. Other dissipation mechanisms that can be discounted include fluid friction, as we are making use of a cryogenic vacuum. Clamping losses can be ignored as the Q is temperature dependent and results from a gold resonator fabricated in a similar way had a clamping loss limited Q of 3.25 million [35]. The most confusing aspect of these results is the huge shift in frequency. While frequency shifts are expected they are normally on the order of 100s of Hz rather than 100s of kHz. As can be seen in equation 2.1.22 there are a number

of things that can effect the frequency of a resonator including, mass, tension and stress. We can ignore a change in tension for the same reasons we can ignore thermoelastic dissipation. However a change of 180 kHz could be explained by an increase in mass of around 9 fg. This mass is approximately equal to around an 10 nm layer of liquid helium on the resonator. As the dilution fridge did have a small leak this explanation is possible however it would be expected that the Q factor would also decrease. One possible explanation is that when the fridge was cooled to below 2 K any helium in the system will have become superfluid. This means that while it would form a film on the beam and effect the frequency of the NEMS it may not effect the Q as there would be no friction between the beam and the helium. However this would not explain the fact that the Q factor increased, as while work by Defoort et al. [66] has shown that both the Q factor and resonant frequency are affected by a change in pressure, this is only for pressures above 10^{-2} mbar which is much larger then the pressures we are working at. In addition Huang et al. [67] have showed that while metallic beams can be effected by exposure to gaseous hydrogen there is very little frequency shift or damping for exposure to gaseous helium. It is possible that the liquid helium film caused a shift in frequency while another mechanism caused the increase in Q factor.

It is interesting to compare our Q factors with other work on polycrystalline aluminium resonators. While there has been, to our knowledge,

no work on aluminium resonators with surface to volume ratios as high as ours ($s/v=7.2\times 10^7\text{ m}^{-1}$) there has been work on resonators with ratios in the same order. Firstly we can look at the work by Lulla et al. [31] discussed in Chapter 3. At 4.2 K they recorded a Q factor of 5000 for a resonant frequency of 7.07 MHz. Notably their results showed very little change in frequency or Q factor between 4.2 K and 1.5 K. It should be noted again that their resonator included a 120 nm layer of silicon. Another key difference between the work is that due to the design of the resonator there would be no additional stress. On work in purely polycrystalline aluminium films there have been a number of pieces of work. The Tsai group have performed work on a number of different aluminium resonators. In particular reference [68] had a 4.2 K Q factor of around 4000 while [33] had a 4.2 K Q factor of 9420. Both of these had surface to volume ratios of $3\times 10^7\text{ m}^{-1}$ suggesting that they should have higher Q factors rather than lower ones. In addition and perhaps most interestingly we have a higher Q factor at 4.2 K than Harrabi et al. [69] managed at 100 mK (12900 for a beam with $s/v=2.3\times 10^7\text{ m}^{-1}$). This last piece of work is interesting as the resonators were designed to be coupled to an electrical circuit which is something we are interested in doing. Another group working on polycrystalline aluminium resonators is the Hakonen group from Aalto university who coupled an aluminium beam resonator into an electrical cavity [34]. They found 1 K Q factors around 17000 for a beam with a surface to volume ratio of

($s/v=2\times 10^7\text{ m}^{-1}$). What is interesting about this work is that it used top down techniques, meaning it could be adapted for monocrystalline aluminium thereby possibly increasing the Q factor.

The question that needs to be answered therefore is why does a single crystal beam have a considerably higher Q factor than a polycrystalline beam even at 4 K? As we are able to compare our results with a number of different polycrystalline beams and to our knowledge there has been no work with Q factor within a factor of two of ours suggest that the increase in Q factor is caused by the fact that there are no grain boundaries in our beam. Whilst it would be understandable that the single crystal beam would have a higher Q factor at the lowest temperatures thanks to the lack of internal defects it is not necessarily true that this would affect the dissipation at temperatures above the crossover temperature T^* . It could also be that our fabrication method results in particularly high Q factors however the Tsai group used similar methods. While it would be nice to think of this as a reason for our improved Q factors and while it may explain how we have higher Q factors than Harrabi et. al where the beams buckled when released it is likely that due to the range of the other work it is not sole cause.

It can therefore be concluded that one of two things are happening. It could be that the fact that the beam is single crystal causes an increase in T^* . The other explanation could be that the remaining grain boundaries cause another form of temperature dependant dissipation

at temperatures above T^* .

Firstly lets consider the transition temperature T^* after which dissipation due to TLS plateaus. For a polycrystalline beam has been shown to be around 1 K for a similar sized device [34] made from polycrystalline aluminium. Unfortunately due to problems with the dilution fridge we were unable to get to temperatures below 1 K. As mentioned in Chapter 3 the transition temperature is defined as when $\omega\tau \sim 1$ which is constantly around 1 K for both metals and dielectrics due to a coth dependence on temperature [24].

So if we are above T^* we must consider what is causing the dissipation. The dissipation at 1.5 K is most likely mostly due to a relaxation interaction within the TLS model of damping. The dissipation at 4 K is harder to explain as it is larger than at 1.5 K meaning that there is probably another dissipation scheme alongside the dissipation due to TLS. Alongside our results work looking at the internal friction of aluminium at temperatures below 100 K [70, 71] has shown a slight temperature dependence above $T^* = 1K$ suggesting another temperature dependent dissipation mechanism is present.

To be sure that our beams do not contain any grain boundaries we need to consider if the beam is indeed made up of a single crystal of aluminium. Whilst x-ray analysis of the original wafer showed that the aluminium layer was a single crystal it may not be the case after fabrication and heat cycling. It is possible that during cooldowns and

warm ups the beam will experience dislocations and cracks. The first piece of evidence that suggests that we would still have a single crystal comes from work by Oh et. al [72] who show that there is very little creation of dislocations at strains below 40%. Thermal contraction would cause a strain of less than 0.1% meaning that it is unlikely that this compression and expansion would cause damage to the beam. In addition to this the beam was placed in an SEM after the experiments and no serious damage could be seen on the beam even after several thermal cycles between 300 K and 4 K (see Figure 7.7). However as mentioned in Chapter 3 it is likely that an oxide layer will have formed on the surface of the aluminium. This layer would contain a number of grains of aluminium oxide. It has been estimated by Tao et al. that for a single crystal silicon resonator with an oxide layer 85% of the internal friction occurs on the surface of the resonator [73]. However it is not clear if the same can be said for a polycrystalline resonator. Figure 7.7 shows an SEM image of the beam after experiments with what appears to be a number grains boundaries around 100 nm in diameter. These could be grains of aluminium formed due to slight lattice constant mismatch between aluminium and GaAs. They could also be grains of aluminium oxide, however it is unlikely that we could see such grains due to the penetration depth of the electron beam in the SEM resulting in it being unable to detect the thin (1-2 nm) layer of aluminium oxide. It is also possible that they could be some form of contamination on

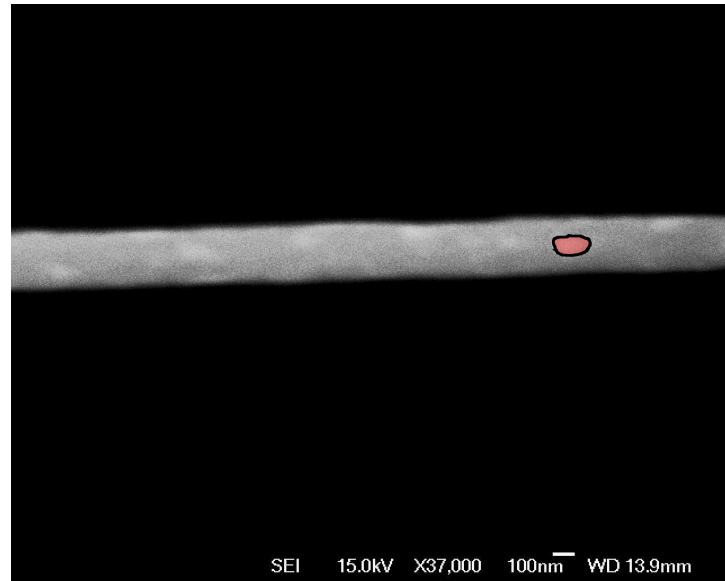


Figure 7.7: SEM image of the aluminium beam used in these experiments taken after the beam was measured. Visible are a number of grains of aluminium oxide on an otherwise undamaged surface. One of the grains of aluminium oxide has been highlighted in red.

the beam or the SEM is causing localized charging on the beam causing false bright spots to appear.

For a polycrystalline material that is put under stress the individual grains will slip and slide against each other [74]. Although we do not know what grain size of aluminium used in the other work has it is reasonable to assume that there would be many grains in the structures. The movement of these grains could cause dissipation in some form. The first form of dissipation that this grain movement could have caused is similar to thermoelastic dissipation. The motion of the grain boundaries would cause localized heating, the resonator would then try to return to its equilibrium state by coupling to its strain field and thus

allowing for an energy flow. Whilst we have said in Chapters 3 and 6 that thermoelastic dissipation is a strongly temperature dependent mechanism it may not be true in this case. This is because for the case of a beam bending the heating would be caused by the expansion and contraction of the aluminium. As the coefficient of thermal expansion is strongly temperature dependent and effectively zero below 100 K [75] this expansion and contraction would cause very little heating. However if the heating is caused by the friction between the grains there could still be an degree of thermoelastic dissipation. In addition to the grain movement causing heating it is also possible that the grains are moving plastically. If the grains are moving plastically they will cause an energy loss as the resonator is no longer able to relax to its original position.

It has been shown that, at least at room temperature, the grain size of the aluminium does effect the internal friction of the film [76]. Further to this Kê [77] has shown that internal friction in aluminium wires at high temperatures is caused by grain boundaries moving in a viscous manner. This friction was found to be temperature dependent between 300 K and 500 K. While no results were given below room temperature the friction at room temperature was very high so it is reasonable to assume that there would still be some internal friction around 4 K. There has however been little work looking at grain boundary slipping at low temperatures although Raza did find evidence for it at temperatures as

low as 25 K [78].

From the above evidence it seems that at 4 K the dissipation is caused by a combination of dissipation due to TLS and dissipation due to movement of grain boundaries. Both of these have been reduced in the monocrystalline beam due to the fact the only grain boundaries occur on a thin oxide layer on the edge of the beam. The dissipation due to the movement of grain boundaries can be reduced by cooling the resonator which increases the viscosity of the grain boundary movement [77]. This shows that working with monocrystalline aluminium over polycrystalline aluminium has the effect of greatly increasing the Q factor even at relatively high temperatures. Thanks to our currently unrivalled ability to create nanomechanical structures from a single crystal of aluminium it should be easily possible to create devices that could operate in the quantum regime.

7.4 Conclusion

This chapter has looked at dissipation of a nanomechanical beam resonator made from a single crystal of aluminium. To our knowledge this is the first NEMS research on of any kind on a single metallic crystal. The results showed Q factors higher than has been seen in polycrystalline aluminium resonators of a similar size. In particular unloaded Q factors of 16000 for the first harmonic and 45200 for the third harmonic

were found at 4.2 K with the former rising to 36900 when cooled to 1.5 K. It was also seen that the frequency of the first harmonic dropped considerably on cooling from 4.2 K to 1.5 K which is not easy to explain but is possibly due to a film of superfluid helium on the beam.

It was shown that the high Q factors can be explained by the lack of grain boundaries. The lack of grain boundaries results in a reduction in the number of defects within the beam. As the main cause of dissipation due to TLS is from defects this causes a reduction in dissipation. As a temperature dependence was seen above the temperature T^* it was assumed another unknown dissipation mechanism was present. It is possible that the movement of the grain boundaries could cause dissipation which would obviously be higher in polycrystalline materials.

Unfortunately we could not take measurements at lower temperatures which would help us to expand on our knowledge of the effect of the grains have on dissipation. This was due to a series of major leaks on the ageing dilution fridge. Future work could be done in cooling down the resonator and seeing how the dissipation varies. If as is thought we have created a sample without many defects then this should result in a resonator with a very high Q factor as when the aluminium becomes superconducting the Q factor at a given temperature will become even larger.

The next chapter looks at the design of an LCR circuit that incorporates a mechanical element. It is hoped that such a system could be

used to make quantum limited measurements. It could be possible in future designs to include an element fabricated from monocrystalline aluminium into such a device.

Design of an on chip LCR circuit

In Chapter 4 we learnt that in order to measure a nanomechanical resonator we need to be able to couple it to a microwave circuit. This chapter draws on the theory discussed in Chapter 4 along with the fabrication methods described in Chapter 5 to describe how we designed an on chip LCR circuit that would be capable of being cooled via side-band cooling and therefore measure the motion of a nanomechanical resonator with quantum limited precision.

8.1 LCR circuit Design

In order to perform microwave coupling we need to be able integrate a mechanical resonator into a microwave circuit. One of the simplest ways of doing this is to make the resonator form part of the capacitor

in an LCR circuit (inductor, capacitor and resistor circuit). There are a number of options available as to how to make the capacitor; from using a metallic beam to form one plate of the resonator to using a silicon nitride torsional resonator to alter the permittivity of the gap between the two capacitor plates. However we have decided to continue the work on high stress silicon nitride membranes done here in Nottingham by Patton and myself by incorporating a metal plate onto a silicon nitride membrane base with a metal dome creating the top plate. In doing this we would be able to include two different mechanical resonators into the capacitor. The choice of metal for the circuit is between aluminium or niobium as these are reasonably strong but most importantly they have superconducting transitions easily reachable by basic refrigeration techniques. In addition to the capacitor we also need to incorporate an inductor. The inductor can take the form of either a spiral or meander by changing their sizes the electrical frequency of the circuit can be altered. The final aspect of the circuit is a ground plane and coplanar stripline that is capacitively coupled to the inductor.

When designing the capacitor there are a number of things that need to be considered, from whether or not it is physically possible to fabricate it, to whether or not it is possible to measure the resonant frequency of the circuit. With fabrication we are limited to the size of the capacitor plates as well as the gap in between them. Whilst the electrical measurements are limited by the frequency range of cabling

and room temperature electronics. Experiments on a range of different sized membranes showed that above 20 microns in diameter the success rate would have been too low to reliably make capacitors. This means that the metallic bottom plate has a maximum diameter (in the case of circular membranes) or side length (in the case of square membranes) of around 18 microns. This will ensure that there is no metal over the clamping points of the membrane which could significantly reduce the Q factor [79]. The top plate will be designed to be slightly larger than the membrane, this is again to ensure that the Q factor of the membrane is not needlessly reduced. The gap between the plates is set by the PMGI resist discussed in Chapter 5 and tests have shown that this is around 200 nm.

Now that the achievable dimensions have been set out we can use a finite element modelling program called COMSOL to simulate the mechanical frequencies of capacitor plates. This shows that we are able to create membranes with mechanical frequencies of between 4 and 20 MHz and top plates with frequencies between 2 and 5 MHz depending on the device dimensions. As we want to alter the size of the gap we are only interested in odd modes and in all likelihood only the first mode will be useful as the displacement of the higher modes will likely have to small an amplitude. This means we can have a plate area between 1 and 5×10^{-10} m². The capacitance can be estimated using $C = \epsilon_0 \epsilon_r \frac{A}{d}$ where A is the area of the plate d is the separation, ϵ_0 is the permittivity of a

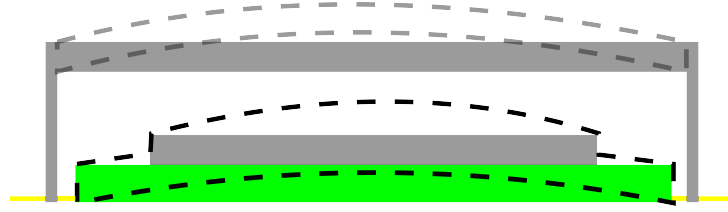


Figure 8.1: Figure showing 2D slice of the mechanics of the parallel plate capacitor. Both the bottom silicon nitride (green) and aluminium (gray) plate and the aluminium top plate are free to resonate with the deformed shape showed by the dotted lines. The whole capacitor is anchored to the substrate (yellow).

vacuum and ϵ_r is the relative permittivity of the gap (which is equal to one in our case). This results in a capacitance of the NEMS of between around 4-20 fF. The mechanics of the modes can be seen in Figure 8.1.

Calculating the inductance of the on-chip inductor is a bit more complicated due to the fact that at these high frequencies and small length scales the standard calculations for inductance do not work. Various attempts have been made to find expressions for such inductances and accuracies of around 5% have been achieved for spirals and 10% for meanders. One of the most accurate expressions for the inductance of a spiral inductor was derived by Mohan [80]. They found that for a spiral inductor with, n turns, an average diameter of d_{ave} and fill factor, $\rho = (d_{in} - d_{out}) / (d_{in} + d_{out})$, where d_{in} and d_{out} are the inner and outer diameters of the spiral respectively the inductance, L is,

$$L = \frac{\mu}{2} c_1 n^2 d_{ave} (\ln(c_2 / \rho) + c_3 \rho + c_4 \rho^2), \quad (8.1.1)$$

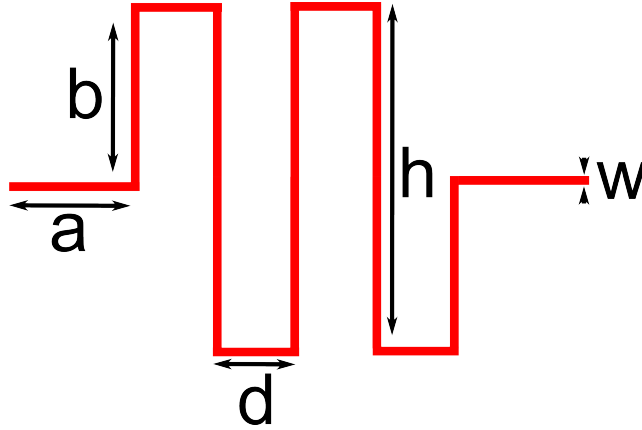


Figure 8.2: Figure showing the definitions a , h , d and w used in equation 8.1.2

where μ is permeability and in our case equals μ_0 . The constants c_n depend on the type of spiral with them equalling, 1.27, 2.07, 0.10 and 0.13 respectively for a square spiral and, 1, 2.46, 0 and 0.2 for a circular spiral. For a meander inductor the inductance can be calculated with the equation [81],

$$L = 2.6 \times 10^{-6} (N^{0.954} a^{0.0603} h^{0.4429} d^{0.606} w^{-0.173}), \quad (8.1.2)$$

where N is the number of meanders and a , h , d and w are the dimensions of the meander as defined in Figure 8.2.

Now that the inductance of the on chip inductor and the capacitance of the NEMS is known we can find out the electrical resonant frequency f_{lc} as,

$$f_{lc} = \frac{1}{2\pi\sqrt{LC}}. \quad (8.1.3)$$

However again this is not as simple as it sounds due to stray capaci-

tances e.g. between the inductor spirals (or meanders) and between the airbridges and underpasses used in the spirals. Calculating the total capacitance of the whole system is made more important as the ratio between the NEMS capacitance, C_{NEMS} , and the circuit total capacitance, C_{tot} , defines how well we can couple together the mechanical and electrical modes of the circuit. Equation 8.1.4 [47] shows that the coupling constant, g_0 , between a NEMS capacitor with a gap d , and zero point motion, κ_0 , and a LC circuit with a resonant frequency ω_c , is,

$$g_0 = \omega_c \frac{\kappa_0}{2d} \frac{C_{NEMS}}{C_{tot}}. \quad (8.1.4)$$

As is shown in Equation 4.2.4 we need this to be as high as possible with $g = g_0 n_{ph}$ where n_{ph} is the number of photons in the electrical circuit. What g_0 shows is the change in frequency of the electrical circuit for a movement equal to the zero point motion. To ensure the ratio $\frac{C_{NEMS}}{C_{tot}}$ is as close to unity as possible we need to design it so that the capacitance of the air bridges in the inductor are in series with each other therefore the total stray inductance is as small as possible. Using a MATLAB program we were able to calculate this ratio, along with the mechanical and electrical frequencies and therefore the coupling constant for a range of different designs. Whilst we had to make a number of estimations in these calculations the error should be reasonably small. These simulations showed that the ratio $\frac{C_{NEMS}}{C_{tot}}$ is above 0.90 for all our designs and values for g_0 varies between 100 and 500

depending on the size of the inductor and mechanical frequency of the membrane. Table 8.1 shows the resonant frequency, capacitance ratio and coupling, g_0 , for 4 different capacitors coupled to a 36 nH spiral inductor. It shows values for both the silicon nitride and aluminium membrane bottom plate and the aluminium top plate. It shows that the resonant frequencies for the two different plates are well separated and thanks to its larger zero point motion the top plate will have better coupling however it is likely to have a smaller Q factor. These values for g_0 are similar or better than the ones we are able to estimate for the work performed by Teufel [42]. This suggests that we should be able to create a resonator that is strongly coupled to the microwave circuit and therefore would be able to perform various sideband effects. We can consider if we could improve on the cooling in works such as [42] or [48] by looking at the cooperativity (Equation 4.2.3). Purely by increasing the Q by swapping the aluminium for high stress silicon nitride we could increase the cooperativity and therefore the cooling power by a factor of around 3.

It is also possible to calculate what the measurement noise, \bar{s}_m for such a system is. The force noise for a capacitor resonator arises from fluctuations in the circuit's resistance which results in a fluctuation in the voltage across the capacitor. This fluctuation in voltage causes a random force between the plates which in turn will cause changes in the size of the gap. In addition to this noise the measurement system also

Type	dimensions/ μm	f_0	C_{nems}/C_{tot}	g_0
Circle membrane	12	24.4	0.93	285.5
Circle top plate	14	4.7	0.93	916
Circle membrane	18	11.1	0.97	181
Circle top plate	20	2.8	0.97	391
Square membrane	12	27.1	0.91	408
Square top plate	14	5.2	0.91	1390
Square membrane	18	12.2	0.95	321
Square top plate	20	2.5	0.95	922

Table 8.1: Table showing the resonant frequencies for a variety of mechanical capacitor plates and there respective C_{mem}/C_{tot} and g values when coupled to a 36 nH spiral inductor. Resonant frequencies are simulated using COMSOL and values of C_{nems}/C_{tot} and g are simulated using Matlab

adds noise that is proportional to the power being sent to the detector [47]. Braginsky and Khalili give the force noise of the system discussed here as,

$$\bar{s}_m = \left[\frac{k_B T_c}{\omega_c} \right], \quad (8.1.5)$$

where T_c is the effective temperature of the circuit which at low temperatures reduces to $\frac{\hbar^2}{4}$.

To give us the best chance of performing measurements we incorporated a number of LCR circuits on one chip. By ensuring that these circuits have a range of electrical frequencies we only need to include one set of contact pads and by changing the microwave frequency we can select which circuit to "talk" to. The microwave signal is sent to the circuits via a microwave stripline with capacitively couples to the inductor. The final part of the chip is the ground plane which covers the rest of the surface of the chip and incorporates an array of unmetallized squares which trap magnetic eddy currents that could interfere with the microwave signal. An image of a LCR circuit where the capacitor is placed within the inductor thus making it possible to actuate it magnetically can be seen in Figure 8.3 and a schematic of the whole chip can be seen in Figure 8.4

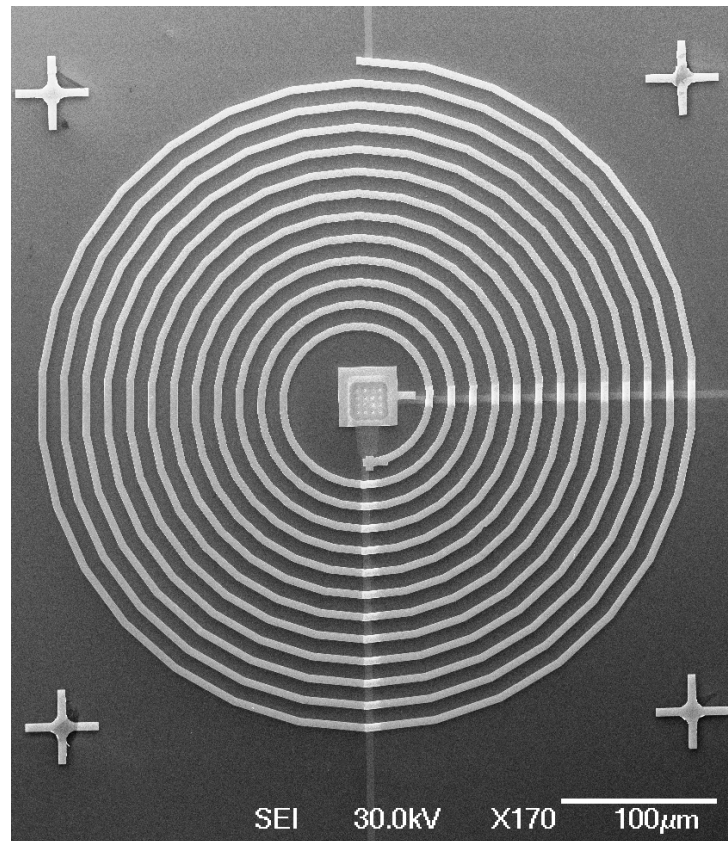


Figure 8.3: SEM image of an on-chip aluminium on silicon nitride LCR circuit. It incorporates a capacitor that has a aluminium on silicon nitride bottom plate.

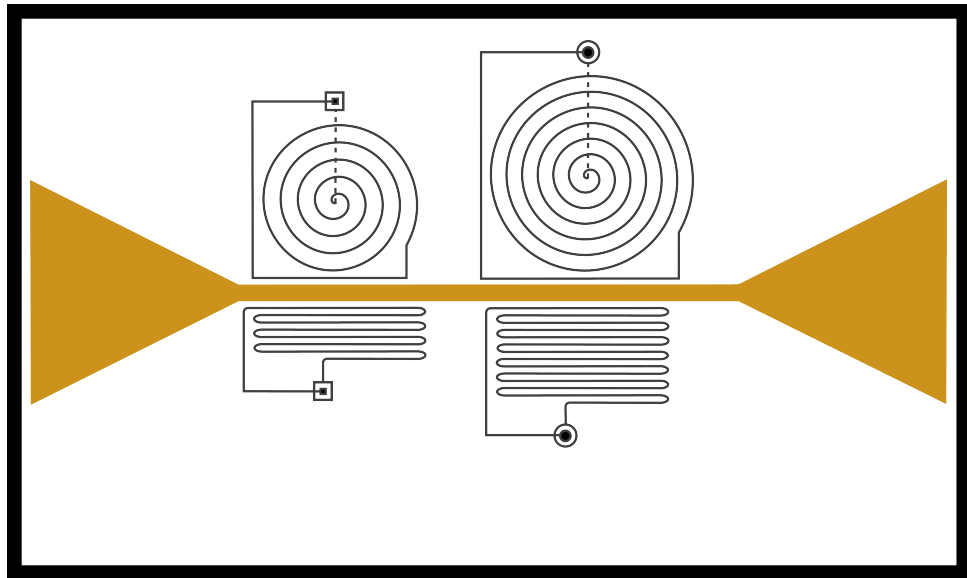


Figure 8.4: Schematic of the design of an LCR circuit with coplanar wave guide. The gold areas represent the wave guide with the silver areas showing a variety of LC circuits. Dashed lines represent the underpass used to escape the spiral inductor. Not shown is the ground plane which surrounds the LC circuits and the coplaner waveguide.

8.2 Conclusion

This chapter has looked at work towards being able to measure a resonator with quantum limited dissipation. In particular it looked at the design of such a circuit. It integrated a high stress silicon nitride membrane with its high Q factor into a parallel plate capacitor. This capacitor was then linked with an on-chip spiral or meander inductor to form an LCR circuit. Simulations suggested that we would be able to create similar coupling constants as work that has got to the quantum limit however we should be able to improve the Q and therefore reduce the amount of heat that is generated by the mechanical resonator.

Once we have coupled the motion of the mechanical resonator into the microwave circuit we will be able to investigate the properties of high stress silicon nitride or even monocrystalline aluminium with very high precision. By pumping with a blue detuned signal we should be able to increase the Q of any resonator and thus be able to investigate the effect a range of factors had on dissipation. It should also be possible to couple a signal crystal aluminium resonator with the microwave circuit. This would allow us to compare the differences between mono- and polycrystalline aluminium which combined with the work performed in Chapter 7 could increase our knowledge of the mechanics of resonators at the lowest temperatures.

CHAPTER 9

Summary and Future Work

In this thesis we looked at dissipation mechanisms in nanomechanical resonators with a view to create a system that could either make quantum limited measurements or cool a resonator down to its quantum ground state.

The first three chapters looked at the mechanics of resonators. Equations of motion were derived for beams, torsional resonators, square membrane and circular "drum" membranes. It then went on to discuss a range of dissipation mechanisms in particular it looked at how dissipation due to two level systems (TLS) within the standard tunnelling model (STM) varies between materials. The predictions of dissipation due to TLS can be seen in Table 3.2. Finally it looked at the theory behind making quantum limited measurements and performing sideband cooling.

We then went on to discuss the various techniques used in this thesis

some of which were particularly novel. In particular we looked at how we are able to create high stress silicon nitride membranes that can then be further processed to make resonators. We also showed the method that allowed us to be the first people to make a nanomechanical beam out of a single crystal of aluminium. The fact that we are able to fabricate airbridges allowed us to make an on chip LCR circuit that incorporated a mechanical resonator into a parallel plate capacitor. Chapter 5 also include a description of how we used proximity effect correction to create incredibly high quality bow-tie nano antennas (BNA's) for optical trapping experiments.

The first experiments performed looked at nanomechanical torsional resonators fabricated from high stress silicon nitride. Thanks to the use of a new design of piezoelectric drive we were able to preferentially actuate the torsional mode of a single paddle resonator which had a Q factor 5050 ± 220 which was larger than the Q factor of 2870 ± 70 that was found for the flexural mode. This showed that thermoelastic dissipation is larger in flexural modes than torsional modes. The size of the dissipation also confirmed that thermoelastic dissipation was almost entirely focused in the paddles meaning paddle resonators will have significantly lower Q factors at room temperatures than simple beams. It was shown that our torsional resonators exhibited higher Q factors than those from other groups suggesting our fabrication technique was very good.

Next we looked at nanomechanical resonators fabricated from a single crystal of aluminium. It was found that even at relatively high temperatures of 1.5 K and 4 K they had impressively high Q factors with the first mode having a unloaded Q factor of 36900 at 1.5 K with the third harmonic having a unloaded Q factor of 45200 at 4.2 K. These were considerably larger than polycrystalline aluminium thanks to the reduction in the number of grain boundaries which can cause dissipation due to TLS as well as thermoelastic dissipation.

The final chapter looked at how we could combine the work of the thesis to create a system that could couple an mechanical membrane into a microwave circuit. We were able to design and fabricate a LCR circuit where the capacitor contained two mechanical elements, an aluminium on high stress silicon nitride bottom plate, and an aluminium top plate. Simulations performed on such a device suggested coupling constants, g , up to 1390. As we have already seen we are able to create devices with high quality factors these would be ample to put us in the good cavity limit as described in Equation 4.2.4.

9.1 Future Work

This thesis shows that with a range of fabrication and experimental techniques it is possible to make high quality NEMS. With these techniques it is hoped that we will be able to create a NEMS devices that

is able to make quantum limited measurements. Whilst we have shown that we have been able to fabricate an on chip LCR circuit which incorporated a nanomechanical resonator we did not have the time to test it this was due to unavoidable delays caused by a superleak in the dilution fridge as well as the need to update the electronics within the dilution fridge. To do this testing it would be useful to cool this sample down to cryogenic temperatures. As we have shown in Chapter 7 we are able to do this. However some changes to the experimental set up would have to be made. To limit the noise we would have to include a microwave circulator, by terminating one of the ports with a matched load we can ensure that we would only amplify the signal coming from the LCR circuit. We would also need to include a cryogenic amplifier to set the thermal noise at around 1 K. Both of these we currently have and it would be reasonably straight forward to incorporate them either into the set up described in Chapter 7 or into a He cryostat. The only other change that would need to be made would be to include wiring that was suitable for use with GHz frequency signals. Whilst it is unlikely that we would be able to reduce the noise to a level below the quantum limit it should be enough to demonstrate that we can couple the microwave circuit and nanomechanical membrane and therefore either cool the resonator or increase its Q factor.

In addition to working on the LCR circuit designed in Chapter 8 it would also be of interest to investigate other ways of incorporating a

nanomechanical resonator into the capacitor. As we have already looked at silicon nitride torsional resonators and found that at least at room temperatures they exhibit higher Q factors than other groups it would be interesting to use these. This could be done, for example, by using the silicon nitride torsional resonator to modify the permittivity of the gap in the capacitor. This would give a ratio between capacitances $C_{res}/C_{tot} = 0.5$ and coupling constant, g , of around 100 which is a reasonably good starting point. It could also be possible to use the single crystal aluminium on GaAs wafers to create either a membrane or a free standing beam that could be incorporated into an capacitor. Both of these could make use of their apparently high Q factor to get close to the quantum limit.

Aside from finishing the work on LCR circuits and microwave coupling it would also be interesting to continue to investigate dissipation in NEMS further. Although a range of materials have been investigated this is often done by a range of groups using a range of different detection and actuation schemes. For this reason it would be interesting for us to use the same fabrication procedure but alter the type of aluminium used. For example we could compare MBE grown monocrystalline aluminium with electron beam or thermally evaporated polycrystalline aluminium with a range of grain sizes. It would also be possible to investigate the effect of an oxide layer by carefully controlling the oxidation the surface of the aluminium. Doing this will allow us to investigate the

role that defects (caused by the grain boundaries and oxide layer) have on the dissipation and therefore hopefully improve our understanding of two level systems within the standard tunnelling model. After Lulla et al. [31] found interesting differences between the dissipation when the beam was in its superconducting or normal state it could also be used to investigate the properties of superconductors at nm length scales.

As it appears that the majority of the dissipation for the silicon nitride torsional resonator was thought to be due thermoelastic damping it would be interesting to cool the resonator down. This is because the thermoelastic damping would effectively reduce to zero and it would be interesting to see what dissipation mechanism takes over. Very little work has been done on analysing the difference between flexural and torsional modes when it comes to dissipation so this would be useful to do. This is because the extra degrees of freedom available in torsional resonators could be used in a range of devices from torque magnetometry [17] or even inclusion into microwave coupling experiments [44].

9.2 Conclusion

In conclusion this thesis has shown that we are able to fabricate a wide range of devices that show impressive Q factors for the conditions they are placed in. It has shown we are able to preferentially actuate the torsional mode of a resonator and therefore obtain a higher room tem-

perature Q factor. It has also shown that we are able to reduce low temperature dissipation in an aluminium resonator by fabricating it from monocrystalline aluminium. Finally it has shown that we are able to design and fabricate a mechanical element coupled to a microwave circuit that should hopefully be able to get close to making quantum limited measurement or even possibly measuring a classical system in its quantum ground state and thus marry classical and quantum mechanics.

APPENDIX A

Fabrication Details

A.1 Silicon Nitride Torsional Resonators

1. Scribe wafer into 9.5 mm by 9.5 mm squares.
2. Clean sample in ethyl lactate followed by acetone, methanol and IPA in an ultrasonic bath for 5 minutes each.
3. Spin PMMA A5 at 5000 rpm for 45 s before being softbaked at 180 °C for 3 minutes on a hotplate.
4. Location and alignment marks are exposed using EBL at a dose of 275 $\mu\text{C}/\text{cm}^2$.
5. Develop the sample in a mixture of 3 parts IPA to 1 part MIBK for 1 minute. Then rinse in IPA and blow dry.
6. Place the sample on a graphite shuttle in the Corial 200IL dry etcher where a 20 s oxygen descum process is carried out (O_2 flow

APPENDIX A: FABRICATION DETAILS

rate 25 sccm, RF power 60 W, pressure 10 Torr) followed by a 20 s silicon nitride etch (CHF_3 flow rate 100 sccm, RF power 150 W, pressure 50 mTorr).

7. Place the sample in a thermal evaporator and then pump out to pressures below 10^{-6} mbar , before evaporating 5 nm of chrome and 50 nm of gold at a rate of 0.5 nm/s
8. Lift off the excess gold by placing the sample in acetone at 60 °C, then placing it in an ultrasonic bath.
9. Spin PMMA A8 at 5000 rpm for 45 s before being softbaked at 180 °C for 3 minutes on a hot plate.
10. Expose an array 1 micron wide dots using EBL at a dose of $500 \mu\text{C}/\text{cm}^2$.
11. Develop the sample in a mixture of 3 parts IPA to 1 part MIBK for 2 minutes. Then rinse in IPA and blow dry.
12. Place the sample on a graphite shuttle in a Corial 200IL dry etcher where a 20 s oxygen descum process is carried out (O_2 flow rate 25 sccm, RF power 60 W, pressure 10 mTorr) followed by a 5 to 6 minute silicon nitride etch (CHF_3 flow rate 100 sccm, RF power 150 W, pressure 50 mTorr).
13. The remaining PMMA is removed by placing the sample in DMSO at 60 °C.

APPENDIX A: FABRICATION DETAILS

14. The sample is wetted by placing it in acetone followed by methanol then IPA then DI water for 5 minutes each without letting it dry between steps.
15. The sample is then etched in 49% hydrofluoric acid for a total of 5 minutes with occasional gentle agitation. This is done in three stages with it being placed in DI water inbetween to ensure the gold does not peel off.
16. The sample is placed in a number of DI water baths for 3 minutes each to ensure all the acid is removed.
17. To release the membranes the sample is placed in IPA followed by methanol for 20 s each before being blow dried with nitrogen for 60 s.
18. Spin PMMA A5 at 5000 rpm for 45 s before being softbaked at 180 °C for 30 minutes.
19. The resonator is exposed using EBL at a dose of 275 – 350 $\mu\text{C}/\text{cm}^2$.
20. Develop the sample in a mixture of 3 parts IPA to 1 part MIBK for 1 minute. Then rinse in IPA and blow dry.
21. Place the sample on a graphite shuttle in a Corial 200IL dry etcher where a 20 s oxygen descum process is carried out (O_2 flow rate 25 sccm, RF power 60 W, pressure 10 mTorr) followed by a 2 minute silicon nitride etch (O_2 flow rate 15 sccm, CHF_3 flow rate

100 sccm, RF power 150 W, pressure 50 mTorr), to release the resonator.

22. If needed an oxygen plasma etch can be used to remove any residual resist.

A.2 Single Crystal Aluminium Resonators

1. Scribe wafer into 4.5 mm by 4.5 mm squares.
2. Clean sample in ethyl lactate followed by acetone, methanol and IPA in an ultrasonic bath for 5 minutes each.
3. Spin PMMA A5 at 5000 rpm for 45 s before being softbaked at 180 °C for 3 minutes on a hotplate.
4. Contact pads and alignment marks are exposed using EBL at a dose of 275 $\mu\text{C}/\text{cm}^2$.
5. Develop the sample in a mixture of 3 parts IPA to 1 part MIBK for 1 minute. Then rinse in IPA and blow dry.
6. Place the sample in a thermal evaporator and then pump out to pressures below 10^{-7} mbar , before evaporating 50 nm of aluminium at a rate of 0.5 nm/s.
7. Lift off the waste aluminium by placing the sample in acetone at 60°C. Followed by being agitated via an ultrasonic bath.

APPENDIX A: FABRICATION DETAILS

8. Spin LOR5B at 5000 RPM for 45 s before being softbaked at 180 °C for 5 minutes on a hotplate.
9. Place the sample in a thermal evaporator and then pump out to pressures below 10^{-6} mbar , before evaporating 50 nm of germanium at a rate of 0.5 nm/s.
10. Spin AR-N 7520 at 4000 rpm for 30 s before being softbaked at 85 °C for 1 minute on a hotplate.
11. The beam is exposed using EBL at a dose of $100 \mu\text{C}/\text{cm}^2$.
12. The sample is developed in 4 parts AR300-47 to 1 part DI water.
13. Place the sample on a graphite shuttle in a Corial 200IL dry etcher for a 2 minute germanium etch (SF_6 flow rate 20 sccm, RF power 60 W, pressure 10 mTorr) followed by a 5 minute LOR etch (O_2 flow rate 25 sccm, RF power 60 W, pressure 10 mTorr).
14. Place the sample on a quartz shuttle in a Corial 200IL dry etcher where a 36 s GaAs etch (SiCl flow rate 25 sccm, SF_6 flow rate 2 sccm, RF power 60 watt, pressure 10 mTorr) followed by a 12 s aluminium oxide etch (BCl_3 flow rate 25 sccm, RF power 100 watt, pressure 10 mTorr) then an aluminium etch (Cl_2 flow rate 90 sccm, C_2H_4 flow rate 10 sccm, RF power 100 watt, pressure 30 mTorr) . The aluminium etch is stopped as soon as the aluminium layer is etched normally around 60 seconds.

APPENDIX A: FABRICATION DETAILS

15. Spin PMMA A5 at 5000 rpm for 45 s before being softbaked at 180 °C for 3 minutes on a hotplate.
16. Etch windows are exposed using EBL at a dose of 275 $\mu\text{C}/\text{cm}^2$.
17. Develop the sample in a mixture of 3 parts IPA to 1 part MIBK for 1 minute. Then rinse in IPA and blow dry.
18. Etch the windows in a mix of 4 parts citric acid to 1 part hydrogen peroxide for 1-2 minutes until the beam is released.
19. Check the beam is released using an SEM and then check the resistance using a 4 wire measurement to ensure that the beam is still conducting as expecting.

A.3 Aluminium and silicon nitride on chip

LCR circuits

1. Scribe wafer into 9.5 mm by 9.5 mm squares.
2. Clean sample in ethyl lactate followed by acetone, methanol and IPA in an ultrasonic bath for 5 minutes each.
3. Spin PMMA A5 at 5000 rpm for 45 s before being softbaked at 180 °C for 3 minutes on a hotplate.
4. Location and alignment marks are exposed using EBL at a dose of 275 $\mu\text{C}/\text{cm}^2$.

APPENDIX A: FABRICATION DETAILS

5. Develop the sample in a mixture of 3 parts IPA to 1 part MIBK for 1 minute. Then rinse in IPA and blow dry.
6. Place the sample on a graphite shuttle in a Corial 200IL dry etcher where a 20 s oxygen descum process is carried out (O_2 flow rate 25 sccm, RF power 60 W, pressure 10 mTorr) followed by a 20 s silicon nitride etch (CHF_3 flow rate 100 sccm, RF power 150 W, pressure 50 mTorr).
7. Place the sample in a thermal evaporator and then pump out to pressures below 10^{-6} mbar , before evaporating 5 nm of chrome and 50 nm of gold at a rate of 0.5 nm/s
8. Lift off the excess gold by placing the sample in acetone at 60 °C, then placing it in an ultrasonic bath.
9. Spin PMMA A8 at 5000 rpm for 45 s before being softbaked at 180 °C for 3 minutes on a hot plate.
10. Expose 1 micron wide dots using EBL at a dose of 500 $\mu C/cm^2$.
11. Develop the sample in a mixture of 3 parts IPA to 1 part MIBK for 2 minutes. Then rinse in IPA and blow dry.
12. Place the sample on a graphite shuttle in a Corial 200IL dry etcher where a 20 s oxygen descum process is carried out (O_2 flow rate 25 sccm, RF power 60 W, pressure 10 mTorr) followed by a 5 to 6

APPENDIX A: FABRICATION DETAILS

minute silicon nitride etch (O_2 flow rate 15 sccm, CHF_3 flow rate 100 sccm, RF power 150 W, pressure 50 mTorr).

13. The remaining PMMA is removed by placing the sample in DMSO at 60 °C.
14. The sample is wetted by placing it in acetone followed by methanol then IPA then DI water for 5 minutes each without letting it dry.
15. The sample is then etched in 49% hydrofluoric acid for a total of 5 minutes with occasional gentle agitation. This is done in three stages with it being placed in DI water inbetween to ensure the gold is not removed.
16. The sample is placed in a number of DI water baths for 3 minutes each to ensure all the acid is removed.
17. To release the membranes the sample is placed in IPA followed by methanol for 20 s each before being blow dried with nitrogen for 60 s.
18. Spin PMMA A5 at 5000 rpm for 45 s before being softbaked at 180 °C for 30 minutes.
19. The capacitor bottom plate, majority of the inductor and inductor underpass is exposed using EBL at a dose of $275 \mu C/cm^2$
20. Develop the sample in a mixture of 3 parts IPA to 1 part MIBK for 1 minute. Then rinse in IPA and blow dry.

APPENDIX A: FABRICATION DETAILS

21. Place in the electron beam evaporator where 70 nm of aluminium is deposited at a rate of 0.1 nm/s
22. Lift off the waste aluminium by placing the sample in acetone at 60 °C. Followed by being gently agitated via an stirrer.
23. Spin MIBK at 5000 rpm for 30 s before being softbaked at 200 °C for 3 minutes on a hot plate.
24. Spin PMMA A5 at 5000 rpm for 45 s before being softbaked at 180 °C for 3 minutes on a hotplate.
25. The foundations for the air bridges and capacitor top plate are exposed using EBL at a dose of 275 $\mu\text{C}/\text{cm}^2$.
26. Develop the sample in a mixture of 3 parts IPA to 1 part MIBK for 1 minute. Then rinse in IPA and blow dry.
27. Expose the PMGI using deep UV at a dose of 10 mJ/cm².
28. Develop the PMGI in MCC 101 developer for 1 minute.
29. Reflow the PMGI by placing the sample on a hotplate at 250 °C for 5 minutes.
30. Spin PMMA A5 at 5000 rpm for 45 s before being softbaked at 180 °C for 3 minutes on a hotplate.
31. The capacitor top plate and the remainder of the inductor is exposed using EBL at a dose of 275 $\mu\text{C}/\text{cm}^2$.

APPENDIX A: FABRICATION DETAILS

32. Develop the sample in a mixture of 3 parts IPA to 1 part MIBK for 1 minute. Then rinse in IPA and blow dry.
33. Place in the electron beam evaporator where 70 nm of aluminium is deposited at a rate of 0.1 nm/s
34. Lift off the waste aluminium by placing the sample in acetone at 60 °C. Followed by being gently agitated via an stirrer.
35. To release the capacitor the sample is placed in IPA followed by methanol for 20 s each before being blow dried with nitrogen for 60 s.

References

- [1] KL Ekinci, XMH Huang, and ML Roukes. Ultrasensitive nanoelectromechanical mass detection. *Applied Physics Letters*, 84(22):4469–4471, 2004.
- [2] HJ Mamin and D Rugar. Sub-attoneutron force detection at millikelvin temperatures. *Applied Physics Letters*, 79(20):3358–3360, 2001.
- [3] D Rugar, R Budakian, HJ Mamin, and BW Chui. Single spin detection by magnetic resonance force microscopy. *Nature*, 430(6997):329–332, 2004.
- [4] AD O’Connell, M Hofheinz, M Ansmann, RC Bialczak, M Lenander, E Lucero, M Neeley, D Sank, H Wang, M Weides, et al. Quantum ground state and single-phonon control of a mechanical resonator. *Nature*, 464(7289):697–703, 2010.
- [5] Jasper Chan, TP Mayer Alegre, Amir H Safavi-Naeini, Jeff T Hill, Alex Krause, Simon Gröblacher, Markus Aspelmeyer, and Oskar

REFERENCES

- Painter. Laser cooling of a nanomechanical oscillator into its quantum ground state. *Nature*, 478(7367):89–92, 2011.
- [6] P Mohanty, DA Harrington, K L Ekinici, YT. Yang, MJ Murphy, and ML Roukes. Intrinsic dissipation in high-frequency micromechanical resonators. *Physical Review B*, 66(8):085416, (2002).
- [7] JD Teufel, T Donner, MA Castellanos-Beltran, JW Harlow, and KW Lehnert. Nanomechanical motion measured with an imprecision below that at the standard quantum limit. *Nature nanotechnology*, 4(12):820–823, 2009.
- [8] A Bokaian. Natural frequencies of beams under tensile axial loads. *Journal of sound and vibration*, 142:481–498, (1990).
- [9] I Kozinsky. *Nonlinear Nanoelectromechanical Systems*. PhD thesis, California Institute of Technology, (2007).
- [10] WC Young and RG Budynas. *Roark’s formulas for stress and strain*, volume 7. McGraw-Hill New York, 2002.
- [11] P Hagedorn and A DasGupta. *Vibrations and Waves in Continuous Mechanical Systems*. Wiley, 2007. ISBN 9780470517383.
- [12] J Woodhouse. On the synthesis of guitar plucks. *Acta Acustica united with Acustica*, 90(5):928–944, 2004.
- [13] DF McGuigan, CC Lam, RQ Gram, AW Hoffman, DH Douglass, and HW Gutche. Measurements of the mechanical Q of single-

REFERENCES

- crystal silicon at low temperatures. *Journal of Low Temperature Physics*, 30(5):621–629, 1978.
- [14] RB Bhiladvala and ZJ Wang. Effect of fluids on the Q factor and resonance frequency of oscillating micrometer and nanometer scale beams. *Physical Review E*, 69(3):036307, (2004).
- [15] I Wilson-Rae. Intrinsic dissipation in nanomechanical resonators due to phonon tunneling. *Physical Review B*, 77(24):245418, (2008).
- [16] I Wilson-Rae. Intrinsic dissipation in nanomechanical resonators due to phonon tunneling. *Physical Review B*, 77(24):245418, 2008.
- [17] JP Davis, Doug Vick, DC Fortin, JAJ Burgess, WK Hiebert, and MR Freeman. Nanotorsional resonator torque magnetometry. *Applied Physics Letters*, 96(7):072513, 2010.
- [18] R. A. Norte, J. P. Moura, and S. Gröblacher. Mechanical resonators for quantum optomechanics experiments at room temperature. *Physical Review Letters*, 116:147202, Apr 2016.
- [19] AN Cleland and ML Roukes. External control of dissipation in a nanometer-scale radiofrequency mechanical resonator. *Sensors & Actuators A: Physical*, 72(3):256–261, (1999).
- [20] M. Patton. *Design and Construction of a Fibre Interferometer for*

REFERENCES

- the Study of MEMS and NEMS to Temperatures Below 1 K*. PhD thesis, University of Nottingham, 2012.
- [21] R Lifshitz and ML Roukes. Thermoelastic damping in micro-and nanomechanical systems. *Physical Review B*, 61(8):5600, 2000.
- [22] Y Tai, P Li, and Y Fang. Thermoelastic damping in torsion microresonators with coupling effect between torsion and bending. *Journal of Sound and Vibration*, 333(5):1509–1525, 2014.
- [23] P W Anderson, BI Halperin, and C M Varma. Anomalous low-temperature thermal properties of glasses and spin glasses. *Philosophical Magazine*, 25(1):1–9, 1972.
- [24] WA Phillips. Two-level states in glasses. *Reports on Progress in Physics*, 50(12):1657, 1987.
- [25] BS Berry and WC Pritchett. Internal stress and internal friction in thin-layer microelectronic materials. *Journal of Applied Physics*, 67(8):3661–3668, 1990.
- [26] S Hunklinger and AK Raychaudhuri. *Thermal and elastic anomalies in glasses at low temperatures*, volume 9. Amsterdam: Elsevier, 1986.
- [27] P Mohanty, DA Harrington, KL Ekinici, YT Yang, MJ Murphy, and ML Roukes. Intrinsic dissipation in high-frequency micromechanical resonators. *Physical Review B*, 66(8):085416, 2002.

REFERENCES

- [28] K Bordo and HG Rubahn. Effect of deposition rate on structure and surface morphology of thin evaporated Al films on dielectrics and semiconductors. *Materials Science*, 18(4):313–317, 2012.
- [29] A Venkatesan, KJ Lulla, MJ Patton, AD Armour, CJ Mellor, and JR Owers-Bradley. Dissipation in a gold nanomechanical resonator at low temperatures. *Journal of Low Temperature Physics*, 158(3-4):685–691, 2010.
- [30] KJ Lulla, RB Cousins, A Venkatesan, MJ Patton, AD Armour, CJ Mellor, and JR Owers-Bradley. Nonlinear modal coupling in a high-stress doubly-clamped nanomechanical resonator. *New Journal of Physics*, 14(11):113040, 2012.
- [31] KJ Lulla, M Defoort, C Blanc, O Bourgeois, and E Collin. Evidence for the role of normal-state electrons in nanoelectromechanical damping mechanisms at very low temperatures. *Physical review letters*, 110(17):177206, 2013.
- [32] Y Tao, JM Boss, BA Moores, and CL Degen. Single-crystal diamond nanomechanical resonators with quality factors exceeding one million. *Nature communications*, 5, 2014.
- [33] TF Li, Yu A Pashkin, O Astafiev, Y Nakamura, JS Tsai, and H Im. High-frequency metallic nanomechanical resonators. *Applied Physics Letters*, 92(4):043112, 2008.

REFERENCES

- [34] MA Sulkko, Jand Sillanpää, P Häkkinen, L Lechner, M Helle, A Fefferman, J Parpia, and PJ Hakonen. Strong gate coupling of high Q nanomechanical resonators.
- [35] R Cousins. Nonlinear effects in nanomechanical resonators at low temperatures. Master's thesis, University of Nottingham, 2012.
- [36] J Haust, M Burst, R Haueisen, and G Weiss. Low temperature acoustic properties of poly-crystalline aluminium. *Journal of low temperature physics*, 137(3-4):523–533, 2004.
- [37] M Poot and HSJ van der Zant. Mechanical systems in the quantum regime. *Physics Reports*, 511(5):273–335, 2012.
- [38] K Jacobs and DA Steck. A straightforward introduction to continuous quantum measurement. *Contemporary Physics*, 47(5):279–303, 2006.
- [39] H Kroemer and C Kittel. *Thermal physics*. WH Freeman, 1980.
- [40] M Aspelmeyer, TJ Kippenberg, and F Marquardt. Cavity optomechanics. *Reviews of Modern Physics*, 86(4):1391, 2014.
- [41] JD Teufel, Tobias Donner, Dale Li, JW Harlow, MS Allman, K Cicak, AJ Sirois, JD Whittaker, KW Lehnert, and RW Simmonds. Sideband cooling of micromechanical motion to the quantum ground state. *Nature*, 475(7356):359–363, 2011.

REFERENCES

- [42] JD Teufel, T Donner, MA Castellanos-Beltran, JW Harlow, and KW Lehnert. Nanomechanical motion measured with an imprecision below that at the standard quantum limit. *Nature nanotechnology*, 4(12):820–823, 2009.
- [43] T Faust, P Krenn, S Manus, JPeter Kotthaus, and EM Weig. Microwave cavity-enhanced transduction for plug and play nanomechanics at room temperature. *Nature communications*, 3:728, 2012.
- [44] PH Kim, C Doolin, BD Hauer, AJR MacDonald, MR Freeman, PE Barclay, and JP Davis. Nanoscale torsional optomechanics. *Applied Physics Letters*, 102(5):053102, 2013.
- [45] AA Clerk, Florian Marquardt, and K Jacobs. Back-action evasion and squeezing of a mechanical resonator using a cavity detector. *New Journal of Physics*, 10(9):095010, 2008.
- [46] MJ Woolley, AC Doherty, GJ Milburn, and KC Schwab. Nanomechanical squeezing with detection via a microwave cavity. *Physical Review A*, 78(6):062303, Dec 2008.
- [47] VB Braginski and FY Khalili. *Quantum measurement*. Cambridge University Press, 1995.
- [48] EE Wollman, CU Lei, AJ W, J S, A Kronwald, F Marquardt, AA Clerk, and KC Schwab. Quantum squeezing of motion in a mechanical resonator. *Science*, 349(6251):952–955, 2015.

REFERENCES

- [49] P Rai-Choudhury. *Handbook of microlithography, micromachining, and microfabrication: microlithography*, volume 1. Iet, 1997.
- [50] George B. *Electron-beam technology in microelectronic fabrication*. Elsevier, 2012.
- [51] BJ Roxworthy, KD Ko, A Kumar, KH Fung, EKC Chow, GL Liu, NX Fang, and KC Toussaint Jr. Application of plasmonic bowtie nanoantenna arrays for optical trapping, stacking, and sorting. *Nano letters*, 12(2):796–801, 2012.
- [52] M Mossayebi, AJ Wright, A Parini, MG Somekh, G Bellanca, and EC Larkins. Investigating the use of a hybrid plasmonic–photonic nanoresonator for optical trapping using finite-difference time-domain method. *Optical and Quantum Electronics*, 48(5):1–11, 2016.
- [53] KR Williams, K Gupta, and M Wasilik. Etch rates for micro-machining processing-part ii. *Journal of Microelectromechanical Systems*, 12(6):761–778, 2003.
- [54] SS Verbridge, JM Parpia, RB Reichenbach, L. Bellan, and HG Craighead. High quality factor resonance at room temperature with nanostrings under high tensile stress. *Journal of Applied Physics*, 99:124304, (2006).
- [55] JP Davis, D Vick, P Li, SKN Portillo, AE Fraser, JAJ Burgess, DC Fortin, WK Hiebert, and MR Freeman. Nanomechanical tor-

REFERENCES

- sional resonator torque magnetometry. *Journal of Applied Physics*, 109(7):07D309, 2011.
- [56] XC Zhang, EB Myers, JE Sader, and ML Roukes. Nanomechanical torsional resonators for frequency-shift infrared thermal sensing. *Nano letters*, 13(4):1528–1534, 2013.
- [57] A Olkhovets, S Evoy, DW Carr, JM Parpia, and HG Craighead. Actuation and internal friction of torsional nanomechanical silicon resonators. *Journal of Vacuum Science & Technology B*, 18(6):3549–3551, 2000.
- [58] QP Unterreithmeier, T Faust, and JP Kotthaus. Damping of nanomechanical resonators. *Physical Review Letters*, 105(2):27205, (2010).
- [59] K Lulla. *Dissipation and Nonlinear Effects in Nanomechanical Resonator at Low Temperatures*. PhD thesis, University of Nottingham, (2011).
- [60] DM Photiadis and JA Judge. Attachment losses of high q oscillators. *Applied Physics Letters*, 85(3):482–484, 2004.
- [61] R Lifshitz and ML Roukes. Thermoelastic damping in micro- and nanomechanical systems. *Physical Review B*, 61:5600–5609, (2000).
- [62] R Meservey and PM Tedrow. Properties of very thin aluminum films. *Journal of Applied Physics*, 42(1):51–53, 1971.

REFERENCES

- [63] JF Cochran and DE Mapother. Superconducting transition in aluminum. *Physical Review*, 111(1):132, 1958.
- [64] IS Khukhareva. The superconducting properties of thin aluminum films. *Soviet Journal of Experimental and Theoretical Physics*, 16: 828, 1963.
- [65] F Pobell. *Matter and methods at low temperatures*. Springer Science & Business Media, 2007.
- [66] M Defoort, KJ Lulla, T Crozes, O Maillet, O Bourgeois, and E Collin. Slippage and boundary layer probed in an almost ideal gas by a nanomechanical oscillator. *Physical review letters*, 113 (13):136101, 2014.
- [67] XMH Huang, M Manolidis, Seong Chan Jun, and J Hone. Nanomechanical hydrogen sensing. *Applied Physics Letters*, 86(14):143104, 2005.
- [68] F Hoehne, Yu. A Pashkin, O Astafiev, L. Faoro, LB Ioffe, Y Nakamura, and JS Tsai. Damping in high-frequency metallic nanomechanical resonators. *Physical Review B*, 81(18):184112, (2010).
- [69] K Harrabi, YA Pashkin, OV Astafiev, S Kafanov, TF Li, and JS Tsai. Fabrication and characterization of al nanomechanical resonators for coupling to nanoelectronic devices. *Applied Physics A*, 108(1):7–11, 2012.

REFERENCES

- [70] X Liu, EJ Thompson, BE White Jr, and RO Pohl. Low-temperature internal friction in metal films and in plastically deformed bulk aluminum. *Physical Review B*, 59(18):11767, 1999.
- [71] AD Fefferman. *The Low Temperature Acoustic Properties Of Amorphous Silica And Polycrystalline Aluminum*. PhD thesis, Cornell University, 2009.
- [72] SH Oh, M Legros, D Kiener, and G Dehm. In situ observation of dislocation nucleation and escape in a submicrometre aluminium single crystal. *Nature materials*, 8(2):95–100, 2009.
- [73] Y Tao, P Navaretti, R Hauert, U Grob, M Poggio, and CL Degen. Permanent reduction of dissipation in nanomechanical si resonators by chemical surface protection. *Nanotechnology*, 26(46):465501, 2015.
- [74] M Prieler, HG Bohn, W Schilling, and H Trinkaus. Grain boundary sliding in thin substrate-bonded al films. *Journal of alloys and compounds*, 211:424–427, 1994.
- [75] SW Van Scriver. *Helium Cryogenics*. Springer Science & Business Media, 2012.
- [76] G Sosale, D Almecija, K Das, and S Vengallatore. Mechanical spectroscopy of nanocrystalline aluminum films: effects of frequency and grain size on internal friction. *Nanotechnology*, 23(15):155701, 2012.

REFERENCES

- [77] T Kê. Experimental evidence of the viscous behavior of grain boundaries in metals. *Physical Review*, 71:533–546, 1947.
- [78] SM Raza. Slip bands in nickel polycrystals at a low temperature. *Scripta Metallurgica*, 16(12):1325–1328, 1982.
- [79] P-L Yu, TP Purdy, and CA Regal. Control of material damping in high-Q membrane microresonators. *Physical Review Letters*, 108(8):083603, 2012.
- [80] SS Mohan. *The design, modeling and optimization of on-chip inductor and transformer circuits*. PhD thesis, Stanford University, 1999.
- [81] G Stojanović, L Živanov, and M Damjanović. Compact form of expressions for inductance calculation of meander inductors. *Serbian Journal of Electrical Engineering*, 1(3):57–68, 2004.